Technische Universität München

TUM School of Natural Sciences

Lehrstuhl für Oberflächen- und Grenzflächenphysik (E20)

Investigations of Self-Assembly Approaches for 3D Molecular Networks at the Solid-Vacuum Interface

Dennis Meier

Technische Universität München
TUM School of Natural Sciences

Investigations of Self-Assembly Approaches for 3D Molecular Networks at the Solid-Vacuum Interface

Dennis Meier

Vollständiger Abdruck der von der TUM School of Natural Sciences der Technischen Universität München zur Erlangung des akademischen Grades eines Doktors der Naturwissenschaften (Dr. rer. nat.) genehmigten Dissertation.

Vorsitz: Prof. Dr. David Egger

Prüfende der Dissertation:

1. Priv.-Doz. Dr. Anthoula C. Papageorgiou
2. Prof. David Écija

Die Dissertation wurde am 14.02.2024 bei der Technischen Universität München eingereicht und durch die TUM School of Natural Sciences am 10.04.2024 angenommen.

Abstract

Due to their potential applications in e.g. catalysis, charge transfer processes in energy conversion systems, or electronic devices, three-dimensional (3D) nanostructures are a research field that has received a lot of attention. Often, well-ordered arrangements are achieved through *bottom-up* approaches. Consequently, there is considerable interest in scrutinizing the individual steps integral to their formation to ensure their high order. In this thesis, three different *bottom-up* strategies to obtain 3D nanostructures in ultrahigh vacuum (UHV) were pursued and investigated by employing microscopy, spectroscopy, and diffraction techniques, such as scanning tunneling microscopy, photoelectron spectroscopy, near-edge X-ray absorption fine structure, normal incidence X-ray standing wave, low energy electron diffraction and temperature programmed desorption.

In the first approach, building blocks aiming to form spin crossover complexes by Fe-ligation were tried to be prepared *in situ* on an Ag(111) single crystal. This endeavor unexpectedly unveiled a fascinating kagome network hosting rotor molecules within its pores. The enantiomerically directed dynamic anchoring of these rotor molecules is intricately tied to the interplay between the kagome structure and the silver surface. Density functional theory calculations provided valuable insights, assigning the interactions among host and guest molecules to the formation and breaking of hydrogen bonds.

For the second approach, oligoamide foldamer molecules with a secondary helical structure were selected to form an upright self-assembly. Due to their size, these molecules are difficult to deposit intact in a well-defined UHV environment. To address this challenge, a novel deposition technique was employed: electrospray controlled ion beam deposition. While foldamers with varying lengths were successfully deposited intact on an Ag(111) surface, they unexpectedly adapted an unfolded conformation. Through ion mobility spectrometry, the spraying process was excluded to cause the unfolding. Hence, the impact upon landing or the interaction with the substrate were identified as potential origins for the loss of the secondary structure after deposition on a surface.

In the third segment of this thesis, porphyrin pedestals were investigated, offering the capacity to bind out-of-plane ligands to their center metal atom, resulting in the formation of 3D structures. The study delves into the behavior of two porphyrins with different substituents on an Ag(111) single crystal: ruthenium octaethyl porphyrin (Ru-OEP) and ruthenium tetrabenzo porphyrin (Ru-TBP). Two self-assembled structures of Ru-OEP and one self-assembly of Ru-TBP were found and initially analyzed without additional ligation.

Subsequent to this examination, ligation of either an exemplary N-heterocyclic carbene (NHC) or CO to the ruthenium metal center in *trans* position relative to the surface was tested. We observed that the substituents of the porphyrins influence the binding strength of the different ligands to the metal center. Furthermore, an intriguing, non-uniform binding behavior of NHCs to the two selected porphyrins was revealed, which is proposed to result from a dynamic tilting of the carbene ligand from the surface normal.

To increase the thermal stability of the NHCs on both pedestal systems, where the desorption of NHCs was already observed at room temperature, we switched to a more passivated surface, Cu(110)-(2×1)O. The stability of the interface compared to Ru-OEP on a pristine Cu(110), revealing an interaction of the ethyl side chains with the surface oxygen on the passivated surface. Despite this, we achieved a stable ligation of the carbene molecules to the ruthenium metal centers at temperatures exceeding 400 K, underscoring the feasibility of this approach for 3D nanoarchitectures.

Zusammenfassung

Dreidimensionale Nanostrukturen erhalten derzeit aufgrund ihrer vielversprechenden Anwendungsmöglichkeiten in Bereichen wie Katalyse, Ladungstransferprozessen in Energieumwandlungssystemen oder Elektronik viel Aufmerksamkeit. Häufig werden 3D-Nanostrukturen durch „*bottom-up*“-Ansätze erreicht. Daher besteht erhebliches Interesse daran, die einzelnen Schritte dieser Anordnungsprozesse eingehend zu untersuchen, um eine hohe Ordnung der Nanostruktur sicherzustellen. In dieser Arbeit wurden drei verschiedene „*bottom-up*“-Strategien zur Herstellung von 3D-Nanostrukturen im Ultrahochvakuum verfolgt und mittels Mikroskopie-, Spektroskopie- und Beugungstechniken, wie Rastertunnelmikroskopie, Photoelektronenspektroskopie, Nahkanten-Röntgenabsorptionsfeinstruktur, Spektroskopie mittels stehender Röntgen-wellenfelder, nieder-energetischer Elektronenbeugung und Temperatur-programmierter Desorption, untersucht.

Im ersten Ansatz wurde versucht, einen Spin Crossover-Komplex *in situ* bestehend aus zwei Liganden und einem Eisenatom auf einem Ag(111)-Einkristall herzustellen. Dieses Vorhaben enthüllte unerwartet ein faszinierendes Kagome-Netzwerk, das Rotormoleküle in seinen Poren einlagert. Die dynamische Verankerung dieser Rotormoleküle ist komplex mit der Wechselwirkung zwischen der Kagome-Struktur und der Silberoberfläche verbunden. Dichtefunktionaltheorierechnungen lieferten wertvolle Einblicke, indem sie die Wechselwirkungen zwischen Wirt- und Gastmolekülen auf die Bildung und das Brechen von Wasserstoffbrückenbindungen zurückführen.

Für den zweiten Ansatz wurden Oligoamidfoldamermoleküle mit einer sekundären helikalen Struktur ausgewählt, die sich aufrechtstehend auf der Oberfläche organisieren sollten. Wegen ihrer Größe, ist eine intakte Deposition dieser Moleküle in einer wohldefinierten UHV Umgebung schwierig. Um dieser Herausforderung zu begegnen, wurde eine neuartige Depositionstechnik, eine Elektrosprayquelle mit kontrollierter Ionenstrahldeposition, verwendet. Während Foldamere mit variierender Länge erfolgreich in intakter Form auf einer Ag(111)-Oberfläche deponiert werden konnten, nahmen sie dort überraschenderweise eine entfaltete Konformation an. Durch Ionenmobilitäts-spektrometrie konnte der Sprühprozess als Ursache für die Entfaltung ausgeschlossen werden. Daher wurden entweder der Landeprozess bei der Deposition oder die Wechselwirkung mit dem Substrat als potenzielle Ursache für den Verlust der sekundären Struktur ausgemacht.

Im dritten Abschnitt dieser Arbeit wurden Porphyrine als Plattformen eingesetzt, die die Fähigkeit haben, axiale Liganden zu binden und so die Bildung von 3D-Strukturen zu ermöglichen. Die Studie untersuchte das Verhalten zweier verschiedener Porphyrine auf Ag(111): Rutheniumoctaethylporphyrin und Rutheniumtetrabenzoporphyrin. Zwei selbstorganisierte Strukturen von Ru-OEP und eine Selbstorganisationsstruktur von Ru-TBP wurden zunächst ohne Liganden untersucht. Nach dieser Analyse wurden die Liganden, ein N-heterozyklisches Carben oder Kohlenmonoxid, in *trans*-Konfiguration gebunden. Es wurde beobachtet, dass die Substituenten der Porphyrine einen Einfluss auf die Bindungsstärke der verschiedenen Liganden zum Metallzentrum haben. Darüber hinaus wurde ein interessantes, nicht einheitliches Bindungsverhalten von den NHCs an die Metallzentren beider Porphyrine beobachtet. Eine dynamische Neigung des Carbenliganden von der Oberflächennormalen wird als mögliche Ursache vorgeschlagen.

Um die thermische Stabilität der an den Porphyrinen gebundenen Carbenen zu erhöhen, bei denen bereits Desorption von NHC bei Raumtemperatur beobachtet wurde, erfolgte ein Wechsel zu Cu(110)-(2×1)O, einer passivierten Oberfläche. Die thermische Stabilität wurde im Vergleich zu Ru-OEP auf einer unbehandelten Cu(110)-Oberfläche untersucht, wobei eine Wechselwirkung der Ethyl-Seitenketten mit dem Sauerstoff von Cu(110)-(2×1)O festgestellt wurde. Dennoch konnte eine stabile Ligation der Carbenmoleküle an die Rutheniummetallzentren der Porphyrine bei Temperaturen über 400 K erreicht werden, was die Durchführbarkeit dieses Ansatzes unterstreicht.

Content

Acknowledgment

I am deeply grateful to the remarkable individuals whose unwavering support, guidance, and contributions have been indispensable throughout completing this PhD thesis:

My heartfelt gratitude goes out to my primary supervisor, *Dr. Anthoula Papageorgiou*, for her steadfast support, invaluable guidance, and mentorship, which have profoundly influenced the direction of my research. Her leadership goes beyond professional roles and extends to a human touch. I also want to express deep appreciation to *Prof. Johannes Barth* for providing me with the opportunity to conduct my research in the E20 and for his ongoing support. Special acknowledgment is reserved for *Dr. Joachim Reichert*, whose assistance with the instruments and valuable feedback significantly contributed to the success of this work. I extend my thanks to *Dr. Peter Knecht* for introducing me to practical part of my research and supporting my work in all aspects.

A heartfelt thank you is extended to the ES-CIBD team, including *Dr. Andreas Walz, Dr. Annette Huettig,* and *Dr. Hartmut Schlichting*, for their collaborative spirit and valuable contributions to the projects. I also appreciate *Benedikt Schoof* for his dedicated efforts and contributions to the research during his master's studies. I extend my sincere gratitude to *Prof. Peter Feulner* and *Dr. Francesco Allegretti* for their fruitful discussions and instrumental support with the PSD chamber.

I would like to express my heartfelt gratitude to *Viktoria Blaschek* for her invaluable assistance in various aspects, including her support in navigating bureaucratic challenges. I am grateful for the steadfast availability and indispensable assistance provided by *Karl Eberle*, *Dr. Knud Seufert*, and *Fabian Strunk*. Their support has proven crucial whenever challenges with our instruments or computer system arose.

I want to express my heartfelt appreciation to *Pablo Vezzoni Vincente*, *Hongxiang Xu*, *Dr. Biao Yang*, *Dr. Alexander Riss*, and the entire E20 team for their collaborative spirit and invaluable assistance during experiments in Munich and various other locations. Their support has played a crucial role not only during periods focused on research but also during times when research wasn't the primary focus.

I extend special mention and deep appreciation to all collaboration partners whose invaluable contributions played a pivotal role in the success of this work. My sincere thanks are owed to *Prof. Ivan Huc*, *Prof. Mario Ruben*, *Dr. Nithin Suryadevara*, and *Dr. Guillaume Médard* for providing the essential molecules crucial to the research and for engaging discussions throughout my experiments. I express gratitude to *Prof. Shobhana Narasimhan* and *Dr. Abhishek K. Adak* for their significant contributions with theoretical

calculations revealing intriguing facts hidden by experimental methods. Furthermore, I would like to convey additional gratitude to *Dr. Fulden Eratam*, *Dr. Alexander Generalov*, and *Dr. Alexei Preobrajenski* for their unwavering support during the intense periods at the synchrotrons. I extend a heartfelt appreciation to *Dr. David Duncan*, offering a special thanks for his invaluable contributions of ideas and practical knowledge that played a significant role in supporting this work. Furthermore, I am grateful for his delightful company, fostering enjoyable conversations and laughter at any hour of the day or night.

Special appreciation goes out to *Valeria Chesnyak* for offering guidance during moments of my own uncertainty. *Anna Quitt* deserves recognition for her corrections in the late stages of this thesis. Lastly, I convey my deepest appreciation to my boyfriend, *Johannes Großkopf*, for his understanding, encouragement, and unwavering support during the ups and downs of this academic endeavor. A deeply heartfelt and sincere thank you to my parents, *Petra Rodenberg* and *Michael Meier*, and my stepparents, *Gudrun Schneider* and *Axel Rodenberg*, for their unwavering support, boundless encouragement, and immeasurable love that have been constant companions throughout every step of my academic journey.

Acronyms

2D	two-dimensional
3D	three-dimensional
ACW	anticlockwise
bbp-COOH	2,6-bis(1H-pyrazol-1-yl)pyridine-4-carboxylic acid
Co-OEP	cobalt octaethyl porphyrin
Co-TBP	cobalt tetrabenzo porphyrin
CW	clockwise
DFT	density functional theory
DLS	Diamond Light Source
dQMF	digital quadrupole mass filter
$^{DT}CCS_{He}$	collisional cross section
ES-CIBD	electrospray controlled ion beam deposition
ESI	electrospray ionization
FFT	fast Fourier transform
***i*-BuO**	*iso*-butoxy
IMe	(1,3-dimethyl-1,3dihydro-2H-imidazol-2-ylidene)
IMS	ion mobility spectrometry
IT	ionization threshold
LbL	layer-by-layer
LDOS	local density of states
LEED	low energy electron diffraction
LT-STM	low temperature STM
MOF	metal-organic framework
ncAFM	non-contact atomic force microscope
NEXAFS	near-edge X-ray absorption fine structures
NHC	N-heterocyclic carbene
NIXSW	normal incident XSW
OMBE	organic molecular beam epitaxy
PES	photoelectron spectroscopy
PSD	photo-stimulated desorption
pyr-Q_n	Q_n with pyrene plattform
Q_n	oligoamides of n 8-amino-2-quinoline-carboxylic acid monomers
RF	radiofrequency
RT	room temperature

Ru-OEP	ruthenium octaethyl porphyrin
Ru-TBP	ruthenium tetrabenzo porphyrin
Ru-TPP	ruthenium tetraphenyl porphyrin
SPM	scanning probe microscope/microscopy
STM	scanning tunneling microscope/microscopy
SWIG	small wires ion guide
TPD	temperature programmed desorption
UHV	ultra-high vacuum
UPS	ultraviolet photoelectron spectroscopy
VT-STM	variable temperature STM
XPS	X-ray photoelectron spectroscopy
XSW	X-ray standing wave

1 Introduction

Bottom-up approaches offer unique opportunities to construct ordered three-dimensional (3D) architectures [1-4]. Due to the number of possibilities of *bottom-up* processes, the obtained structures can be widely applicable, e.g., in electronic devices [5-6], charge or ion transfer [7-9], catalysis [10-12], optical applications [13-16] or adsorption processes [17-18]. However, the functionality and applicability strongly rely on the order of organization of the assembly, making it crucial to investigate formation processes on a fundamental level. Several different strategies of *bottom-up* formation of 3D architectures are known, such as layer-by-layer (LbL) or template growth [19-20]. In LbL growth, the different building units are separately introduced forming well-ordered two-dimensional (2D) layers working as pedestals for the next layer by, e.g., organometallic bonds or π stacking [21-23]. In template growth, the formation of the 3D self-assembly is guided, for instance, by interactions with a host network or the substrate [24-27], or self-templating through the components' 2D network [28-29]. Regardless of the growth mechanism, a primary challenge persists in controlling such processes and, consequently, the 3D architectures.

Within the scope of this thesis, different approaches were pursued to investigate the formation of *bottom-up* 3D architectures in ultra-high vacuum (UHV). UHV has proven to be extremely helpful to provide a suitable environment to study model systems with atomic precision and gives the opportunity for isolated investigation of interactions between the individual components. Thus, important insights into the single steps towards well-ordered 3D architectures can be gained. A combination of state-of-the-art surface science techniques, such as scanning tunneling microscopy (STM), low energy electron diffraction (LEED), X-ray and ultraviolet photoelectron spectroscopy (XPS and UPS), temperature programmed desorption (TPD), normal incident X-ray standing wave (NIXSW) and near edge X-ray absorption fine structure (NEXAFS), was used to characterize the structures and to determine crucial elementary steps in the formation of 3D architectures.

In Chapter 4, we identified 2,6-bis(1H-pyrazol-1-yl)pyridine-4-carboxylic acid (bbp-COOH) as a potential ligand for the formation of a 3D spin crossover complex with Fe ions on an Ag(111) substrate (Figure 1.1a). We envisioned this to be driven by the distinctive characteristics of the ligand, which feature a compact ligation pocket formed by three nitrogen atoms. The spatial arrangement of the atoms could have the potential to generate a hexagonal ligand field involving two bpp-COOH molecules and a Fe ion, resulting in an upright conformation of at least one ligand. The ligand was supplied by the group of *Mario Ruben* from Karlsruhe Institute of Technology, Germany. Surprisingly, our exploration uncovered an

enantiospecific self-assembled system of rotors within a host network in the absence of Fe. Intrigued by this discovery, we delved into a profound analysis of the rotational behavior of the guest molecules in the pores of the host network. Supported by density functional theory (DFT) calculations performed by the group of *Shobhana Narasimhan* from the Jawaharlal Nehru Centre for Advanced Scientific Research, India, we demonstrated that hydrogen bonds play a pivotal role in inducing preferential positioning of the rotors within the pores, resembling a raffle wheel.

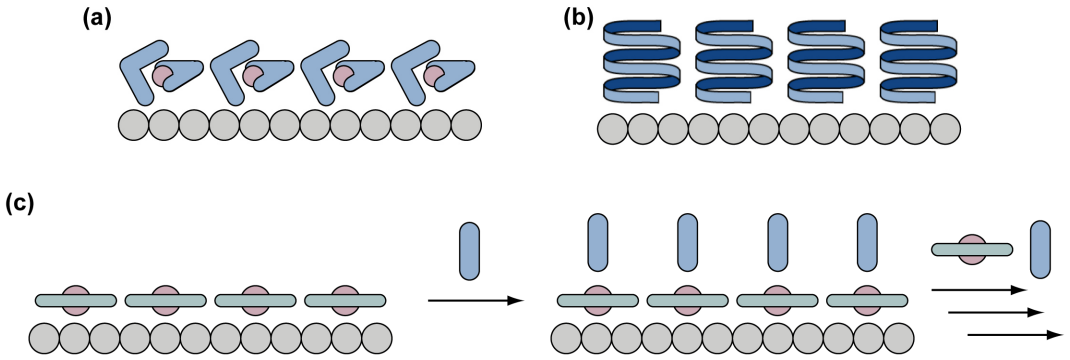

Figure 1.1: Envisioned approaches to obtain 3D architectures studied in this thesis: (a) on-surface formation of spin crossover complexes, (b) deposition of oligomers with distinct 2D conformation and (c) layer-by-layer deposition.

In Chapter 5, we explored the self-assembly of molecules with a pre-established secondary structure, giving the potential to establish an ordered 3D layer (Figure 1.1b). As a representative molecular class, oligoamide foldamers of the group of *Ivan Huc* from Ludwig-Maximilian University, Germany, were selected. These helical molecules are renowned for their robust secondary structure and, hence, exhibit exceptional resistance towards unfolding [30-31]. However, achieving clean deposition in UHV of such large molecules poses a considerable challenge [32-33]. To address this issue, we employed a newly in-house built deposition technique, electrospray controlled ion beam deposition (ES-CIBD), facilitating clean depositions of unsublimable molecules [34-36]. Through STM, we showed that the intact molecules were successfully deposited on the surface, forming a highly ordered self-assembly. Intriguingly, a loss of the secondary structure was observed. Investigating key steps of the deposition process, ion mobility spectrometry (IMS) confirmed that spraying is not affecting the secondary structure. This highlights the significance of the landing process and substrate interactions as pivotal factors in overcoming challenges associated with the loss of the secondary structure.

Chapters 6 to 8 present new insights in an LbL approach, starting with porphyrins as a pedestal for building surface-mounted metal-organic frameworks (MOF) (Figure 1.1c) [23, 37]. Recognized for their propensity to form well-ordered 2D self-assemblies on metal substrates

[38-39], porphyrins can serve as platforms for the subsequent development of 3D structures [37, 40-42]. Our investigation commenced with an analysis of two ruthenium porphyrins, octaethyl porphyrin (Ru-OEP) and tetrabenzo porphyrin (Ru-TBP), exploring the impact of their substituents on self-assembly and their metal centers on Ag(111) described in Chapter 6. This analysis revealed influences on the electronic structure, variations in adsorption height, and distinct conformations of the macrocycles.

In Chapter 7, the ligation of ruthenium porphyrin pedestals by N-heterocyclic carbenes (NHCs) in *trans* position to the surface was explored to extend their self-assembled nanostructures into the third dimension. NHCs, in our case 1,3-dimethyl-1,3dihydro-2H-imidazol-2-ylidene (IMe), are known to form strong bonds with metal single atoms [43-48]. Surprisingly, based on NEXAFS measurements, the NHC ligands are not completely perpendicular to the surface. We propose that this is caused by a dynamic movement of the ligands. This discovery provides valuable insights into the interactions between porphyrins and *trans* ligands, substantial for the formation of 3D architectures and, thus, for comprehending the fundamentals of LbL in UHV. However, on Ru(IMe)-OEP as well as Ru(IMe)-TBP on Ag(111), IMe desorption was observed at room temperature (RT), necessitating reinforcement of the carbene-ruthenium bond to achieve stable 3D architectures at and above RT. The surface itself acts as a *trans* ligand, competing with the carbene. This so-called surface *trans* effect [49-52] leads us to the strategy pursued in Chapter 8 to strengthen the bond between carbene and metal center of the porphyrin.

To mitigate the interactions of the Ru metal center with the substrate and, thus, to enhance the binding strength of the carbene, the surface was changed to a less strongly interacting substrate in Chapter 8: Cu(110)-(2×1)O. The change to the Cu(110)-(2×1)O substrate led to a remarkable increase in the stability of the IMe porphyrin interface, surpassing 400 K compared to the bare Cu(110) surface, thereby making RT-stable 3D architectures achievable with this approach.

2 Methodology

Throughout this thesis, a combination of complementary techniques has been applied to investigate metallic surfaces and adsorbed molecules in UHV. This chapter provides comprehensive descriptions of the employed techniques as well as their underlying fundamental physical principles.

2.1 Electrospray Ionization

Electrospray ionization (ESI) is a soft ionization method developed in the 1980s [53]. *John B. Fenn* was awarded the Nobel Prize in Chemistry in 2002, along with *Kōichi Tanaka*, for this development [54].

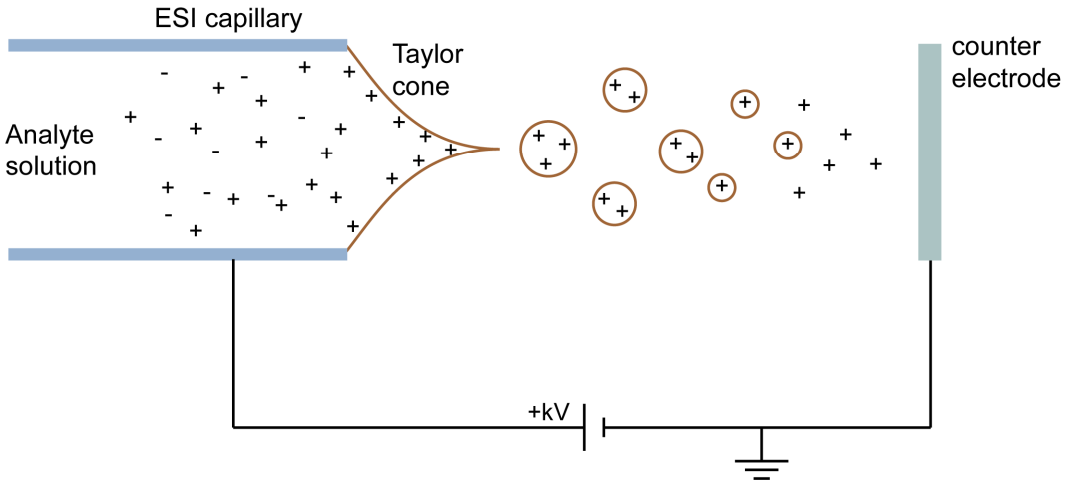

Figure 2.1: Scheme of an exemplary ESI source. Adapted from [55].

A solution of the molecules of interest is pumped through a capillary with an electric potential of approximately 1.5 to 6 kV (Figure 2.1) [56]. The solution at the end of the capillary is deformed into a Taylor cone, which releases a fine spray of droplets towards the counter electrode [57-58]. The solvent evaporates during spraying and, consequently, the droplet volume decreases while having a constant charge. At some point, a critical radius is reached and the *Coulomb* repulsion is greater than the surface tension, triggering *Coulomb* fission. This results in the division of the droplet into several smaller droplets, and thereby, the total surface enlarges [59]. The *Rayleigh* limit gives the critical charge q_r as an upper limit of the charge carried by these spherical droplets with radius r:

$$q_r = 8\pi\sqrt{\epsilon_0 \gamma r^3} \tag{2.1}$$

where ϵ_0 is the vacuum permittivity and γ is the surface tension [35, 60]. The newly formed droplets' charge is again below the critical charge predicted by the *Rayleigh* limit. A sequence of solvent evaporation and *Coulomb* fissions shrinks the droplet and leads to solvent-free ions [55]. This beam of ions can now be analyzed, for instance, by mass spectrometry or transported and deposited onto surfaces in UHV by ion optics.

2.2 Scanning Tunneling Microscopy

A scanning probe microscope (SPM) operates by precisely scanning a surface with a sharp tip in close proximity, thereby achieving high spatial imaging resolution [61]. The first SPM technique was the scanning tunneling microscope developed by *Gerd Binnig* and *Heinrich Rohrer* at the IBM Zurich Research Laboratories in the 1980s [62-63]. Their groundbreaking contributions were recognized with the Nobel Prize in Physics in 1986, underscoring the significance of their achievements [64]. The fundamental working principle is based on the tunneling effect, which will be here shortly derived. A more detailed description can be found in, for example, [65]. In quantum mechanics, the tunneling effect describes how a particle can propagate with a certain probability through a potential barrier V with a finite height, even if its energy E is smaller than V (Figure 2.2a), which is not possible in classical physics. Particles, such as electrons, can be described by a wave function Ψ with the time-independent *Schrödinger* equation in a one-dimensional model:

$$\frac{\hbar^2}{2m}\frac{\partial^2}{\partial z^2}\Psi(z) = (V(z) - E)\,\Psi(z). \tag{2.2}$$

Here, $\hbar$ is the reduced *Planck* constant and m the mass of the electron. A wave propagation towards the right leads to the following solutions of the *Schrödinger* equation for the regions $I - III$ (Figure 2.2a):

$$\Psi_{I,III}(z) = \exp(ikz), \qquad k = \sqrt{\frac{2m}{\hbar^2}\,E} \tag{2.3}$$

$$\Psi_{II}(z) = \exp(-\kappa z), \qquad \kappa = \sqrt{\frac{2m}{\hbar^2}\,(E - V(z))} \tag{2.4}$$

where k and κ are the wavevectors. The solution of regions outside the potential barrier takes the shape of an oscillating wave, whereas, within the potential barrier, the solution exhibits an exponential decay. Linear combination with a left-traveling wave, another independent solution of the *Schrödinger* equation, provides the following description of the system:

$$\Psi_{I,III}(z) = \begin{cases} \mathrm{A}\exp(ikz) + \mathrm{B}\exp(-ikz), & for\ region\ I \\ C\exp(-\kappa z) + \mathrm{D}\exp(\kappa z), & for\ region\ II \\ F\exp(ikz), & for\ region\ III. \end{cases} \tag{2.5}$$

The coefficients A, B, C, D and F can be determined by consideration of continuity conditions. With these, the transmission factor T, which describes the probability of the electron being in region III, can be obtained and is given by

$$T = \frac{16k^2\kappa^2}{(k^2+\kappa^2)^2}\exp(-2\kappa d) \tag{2.6}$$

where d is the potential barrier width. Therefore, the tunneling probability of an electron through a barrier depends exponentially on the barrier width and the differences between the electron energy and the potential barrier height. A visualization of tunneling in an STM junction is provided in Figure 2.2b [65]. The distance of the probe tip and the surface equals the barrier width. Bringing these two in tunneling contact, their Fermi levels align and electrons can tunnel between the tip and sample. In this state, no directed tunneling current is measurable. However, by applying a bias between the tip and the sample, a shift in Fermi level occurs, leading to the observation of a directed tunneling current. The potential barrier is not rectangular in this case anymore.

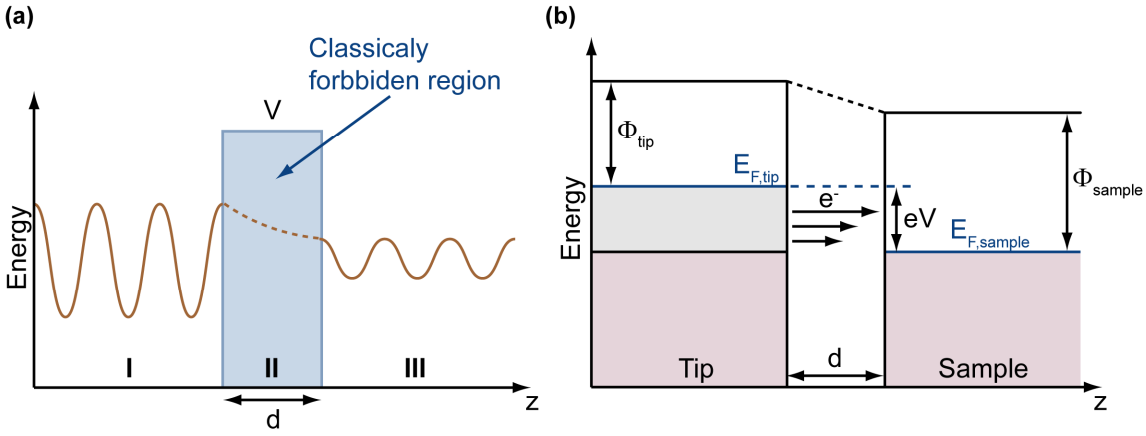

Figure 2.2: (a) Visualization of the wave function with a rectangular finite potential barrier. (b) Schematics of the energy of an STM tip in tunneling contact with a sample.

Tersoff and *Hamann* developed a more sophisticated theory to describe tunneling between a surface and the STM tip [61, 66] with a formalism introduced by *Bardeen* [67], which describes the tunneling current I by

$$I = \frac{2\pi e}{\hbar}\sum_{\mu,\nu} f(E_\mu)\left[1 - f(E_\nu + eV)\right]\left|M_{\mu\nu}\right|^2 \delta(E_\mu - E_\nu) \tag{2.7}$$

where $f(E_\mu)$ is the Fermi function, V is the applied voltage, $M_{\mu\nu}$ is the tunneling matrix element between states Ψ_μ of the probe and Ψ_ν of the surface, E_μ and E_ν is the energy of the state Ψ_μ and Ψ_ν in absence of tunneling, respectively [61]. STM experiments are mostly performed at or below RT and with small voltages. Therefore, an approximation in the limits of small voltage and temperature can be considered [61]. This simplifies the expression of the tunneling current to

$$I = \frac{2\pi}{\hbar} e^2 V \sum_{\mu,\nu} |M_{\mu\nu}|^2 \delta(E_\mu - E_F)\, \delta(E_\nu - E_F). \tag{2.8}$$

Bardeen describes the tunneling matrix element $M_{\mu\nu}$ by an integral over a surface entirely situated within the vacuum region between the two tunneling contacts (in the case of STM the tip and the sample) [67]:

$$M_{\mu\nu} = \frac{\hbar^2}{2m} \int dS \left(\Psi_\mu^* \vec{\nabla} \Psi_\nu - \Psi_\nu \vec{\nabla} \Psi_\mu^*\right). \tag{2.9}$$

The tunneling matrix elements are only dependent on the wave functions of the two electrodes (tip and surface) separately. s-waves are approximated for the unknown wave functions of the tip which is modeled as a locally spherical potential well with a radius R and its center located at $\overrightarrow{r_0}$ [61]. The work functions ϕ of tip and surface are assumed to be equal for simplification [61]. The following expression for the tunneling current is obtained:

$$I = 8\sqrt{2}\pi^3 \hbar^2 e^2 V \sqrt{\frac{\phi}{m^3}} D_t(E_F) R^2 \exp\left(\frac{2R\sqrt{2m\phi}}{\hbar}\right) \sum_\nu |\Psi_\nu(\overrightarrow{r_0})|^2\, \delta(E_\nu - E_F) \tag{2.10}$$

where D_t is the density of states per unit volume of the probe tip [61]. The expected exponential decay of the tunneling current with respect to the barrier width d is predicted, given by

$$|\Psi_\nu(\overrightarrow{r_0})|^2 \propto \exp\left(-\frac{2\sqrt{2m\phi}}{\hbar}\, d\right). \tag{2.11}$$

The tunneling current is also directly correlated with the local density of states (LDOS) of the surface at E_F, given by the sum term of eq (2.10). This makes the acquired STM images comprehensible as a convolution of both surface topography and LDOS. For more details, see the derivation by *Tersoff* and *Hamann* [61].

Figure 2.3a provides an overview of the technical implementation of an STM [65]. The instrument utilizes an atomically sharp metallic tip as a probe, which is brought close to the surface until a tunneling current is detected (0.5 – 1 nm). This tip is attached to a piezoelectric tube, enabling movement in the x, y, and z directions at sub-angstrom precision. During the scanning process, the tip traverses the surface along the x and y directions. To generate an

STM image, two operational modes can be considered: constant current and constant height mode (Figure 2.3b,c) [68]. In the constant height mode, the tip's height remains fixed, and the tunneling current is measured (Figure 2.3b). Therefore, an atomically flat surface and a very stable system are needed to prevent a crash between tip and surface. Conversely, the constant current mode maintains the measured tunneling current at a constant level, with a feedback loop adjusting the tip's height accordingly (Figure 2.3c). The tip displacement is recorded, termed as “apparent height”. Its signal yields a detailed STM image as a convolution of LDOS and topography [65].

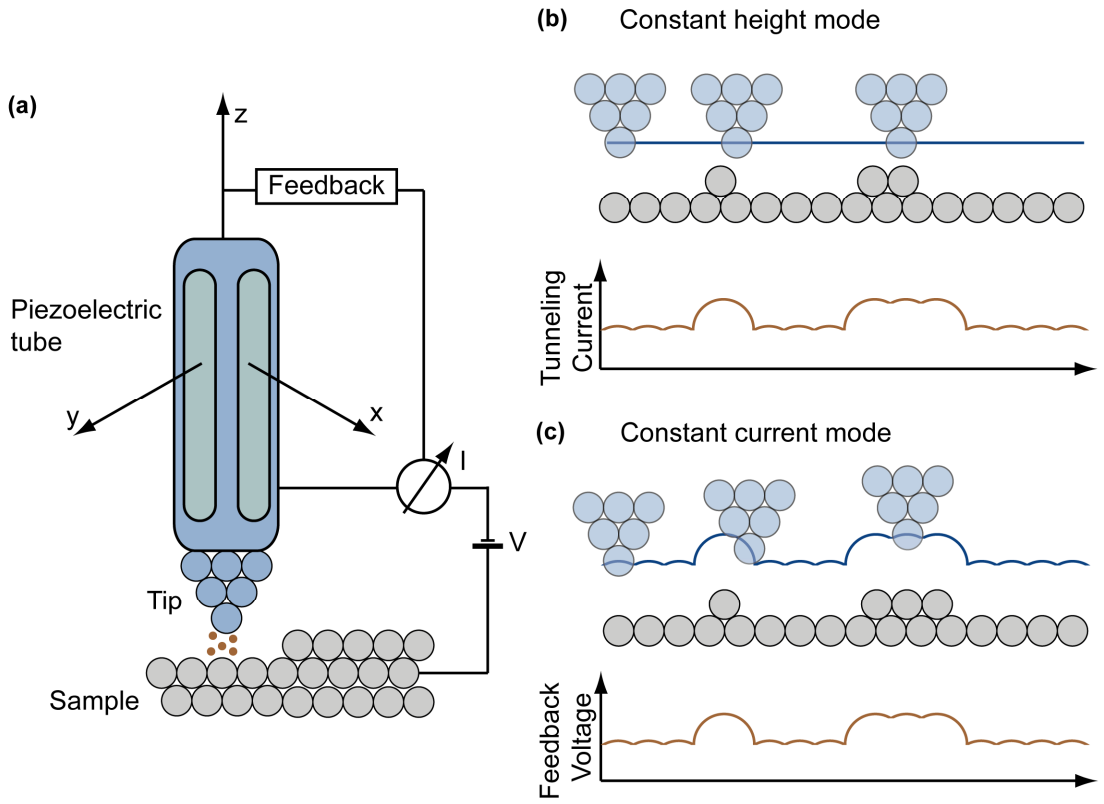

Figure 2.3: (a) Scheme of the working principle of a scanning tunneling microscope. Adapted from [65]. There are two different operation modes of STM: (b) constant current and (c) constant height mode. At the top, a scheme of the tip and the surface for the respective mode is shown. The height of the tip for the measurement is indicated by the blue line. At the bottom, the corresponding measurement of the feedback voltage/tunneling current is given, respectively. Adapted from [68-69].

2.3 Photoelectron Spectroscopy

The interaction of electromagnetic radiation with a material can lead to the emission of electrons. This so-called photoelectric effect was first described by *Heinrich Hertz* in 1887 [70]. But only in 1905, *Albert Einstein* was able to explain the observed effect by the quantum nature of light [71]. For the theoretical description of the photoelectric effect, he was awarded the Nobel Prize in Physics in 1921 [72].

Photoelectron spectroscopy (PES) takes advantage of this effect. The techniques was developed by *Kai Siegbahn*, who was awarded in 1981 with the Nobel Prize in Physics [73]. A light source, such as a gas discharger lamp, X-ray tube, or synchrotron, is emitting towards a sample, at which photoelectrons are emitted, and analyzed regarding their kinetic energy (E_{kin}) with an electron energy analyzer (Figure 2.4) [74]. A (semi)conductive sample is required to avoid charging. However, with an electron flood gun, which provides electrons to the sample, nonconductive samples can be measured as well [75]. The technique is categorized by the employed wavelength of the electromagnetic radiation in UPS used to investigate the band structures close to the Fermi level, and XPS, mostly used for analysis of the core level binding energies (usually higher than 120 eV). The “universal” electron mean free path, describing the scattering length of electrons in metals in dependence on their energy (5 – 5000 eV), is just a few tens of angstroms [74]. This makes photoelectron spectroscopy a surface-sensitive tool.

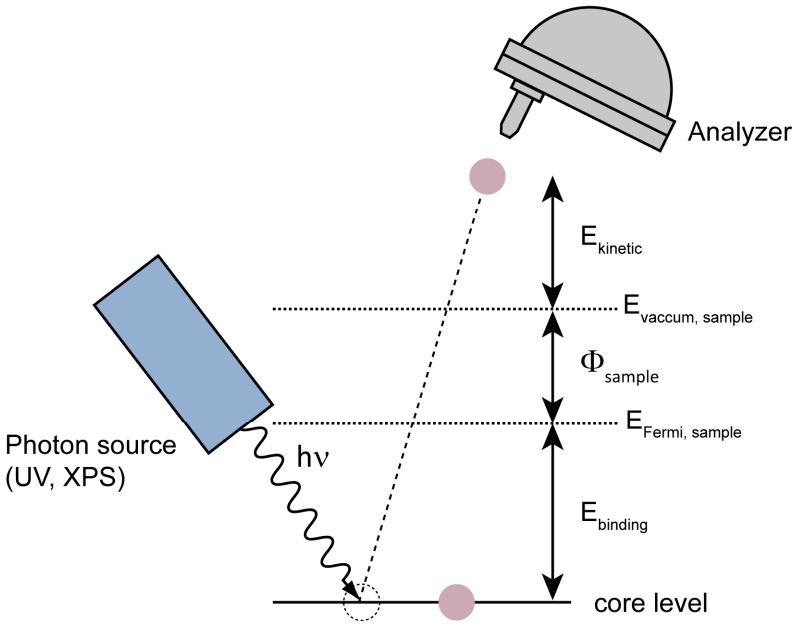

Figure 2.4: Schematics of the working principle of photoelectron spectroscopy and the underlying photoelectric effect. An electron is emitted with a specific kinetic energy by the incoming radiation, which is measured by an analyzer.

The measured kinetic energy E_{kin} can afterwards be translated to the binding energy E_{bin} of the electron with respect to the Fermi level by

$$E_{kin} = h\nu - \Phi - E_{bin} \tag{2.12}$$

where $h\nu$ is the energy of the incoming radiation and Φ is the work function of the material (Figure 2.4) [74]. The core level electron energy is specific for chemical elements, making PES an element-sensitive technique [76]. In addition, it can detect differences in the chemical environment of the atoms. Modifications, such as bond formation or cleavage with a more

electronegative atom or the occurrence of charge transfer from the metal substrate to the atom, result in alterations in the screening of the nuclear charge. These changes, in turn, impact the binding strength of the emitted electrons [76]. Therefore, a third advantage of this technique is its chemical state sensitivity.

The work function Φ can also be determined using XPS by the secondary electron cutoff detection, which is defined as

$$\Phi = h\nu - \left|E_{Fermi\ level} - E_{seondary\ electron\ cutoff}\right|. \tag{2.13}$$

Here, $E_{Fermi\ level}$ and $E_{seondary\ electron\ cutoff}$ are the energies of the Fermi edge and second electron cutoff, respectively (Figure 2.5) [42].

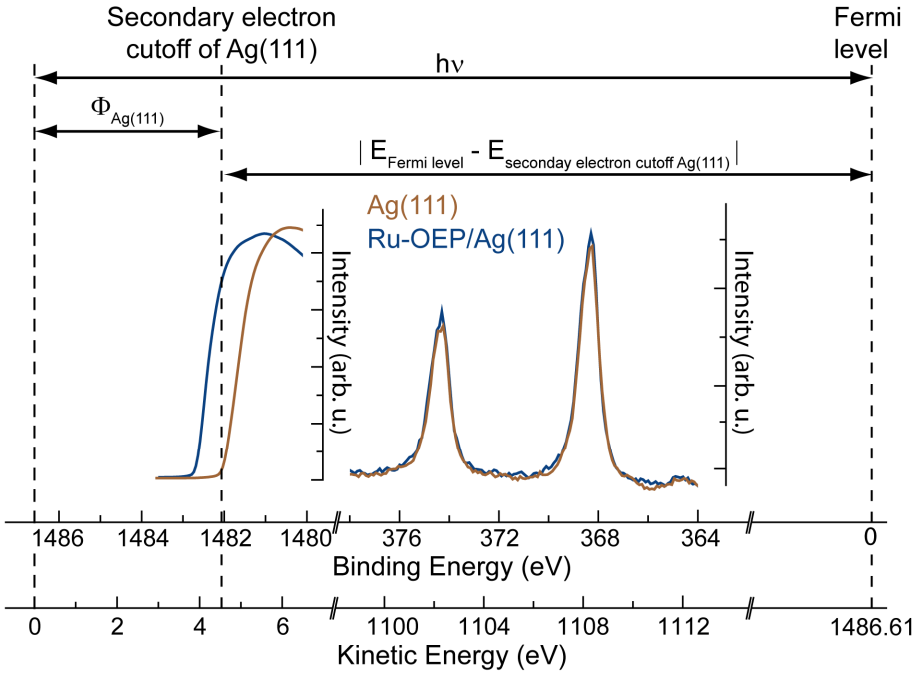

Figure 2.5: Schematics of the determination of the work function by secondary electron cutoff. Adapted from [42].

2.4 Near-Edge X-ray Absorption Fine Structure

Near-edge X-ray absorption fine structure is employed to investigate the electronic structure and orientation of molecules on surfaces *via* K-shell excitation to unoccupied states of the molecules by X-ray radiation [77]. The measured resonances of adsorbed molecules on surfaces arise mostly through transitions to highly localized π^* and σ^* antibonding molecular orbitals. Other resonances of adsorbed molecules, e.g., Rydberg states, are mostly suppressed, making these spectra easier to interpret than the respective gas phase spectra [78-79]. Typically, bonds between atoms with low atomic numbers, such as C, N, O, F, and S,

are analyzed. Single-bonded atoms have just a σ bond in the molecular axis, whereas double-bonded atoms have σ bonds and orthogonal to them π bonds. Excitations to π^* antibonding molecular orbitals are typically the lowest energy features, often below the ionization threshold (IT) [77]. Transitions to σ^* antibonding molecular orbitals are higher in excitation energy (mostly higher than the IT) [77]. Due to being oriented in between the molecular axes of atoms, σ^* features are observed as asymmetric peaks broadened by molecular vibrations [77, 80]. In a molecular orbital picture, K-shell excitations in NEXAFS can be considered as dipole transitions from an initial s-state to the p-component of the σ^* or π^* final state [77-79]. Dipole selection rules suggest that the resonance should be the largest when the electric field vector $\boldsymbol{E}$ is along the final state orbital direction of maximal amplitude (Figure 2.6a). Therefore, the NEXAFS intensities show a dependence on the orientation of $\boldsymbol{E}$ as follows:

$$I \propto |\boldsymbol{E} \cdot \boldsymbol{O}|^2 \propto cos^2\delta \qquad (2.14)$$

where $\boldsymbol{O}$ is the direction of the final state orbital (e.g. direction of maximum orbital amplitude) and δ is the angle between $\boldsymbol{E}$ and $\boldsymbol{O}$ [77].

Highly linear polarized X-ray radiation and a continuous photon energy regime are needed for NEXAFS; thus, it is mostly performed in synchrotrons. However, elliptically polarized synchrotron radiation has two finite components $E^{\parallel}$ and $E^{\perp}$. The NEXAFS intensity depends from both components of the radiation as followed:

$$I = C \cdot [P \cdot I^{\parallel} + (1 - P) \cdot I^{\perp}] \qquad (2.15)$$

with P being the polarization factor and C being a constant. Geometrical considerations provide a formula for the dependency of the intensity of the resonance on the polar angle α of the vector orbital $\boldsymbol{O}$ and the angle of the X-ray towards the surface normal θ for a substrate with a threefold symmetry as

$$I = A \cdot [P \cdot (\tfrac{1}{3} + \tfrac{1}{6}(3cos^2\theta - 1) \cdot (3cos^2\alpha - 1)) + (1 - P) \cdot (\tfrac{1}{2} sin^2\alpha - 1)] \qquad (2.16)$$

where A is a constant [77]. The corresponding angles of eq. (2.16) are indicated in Figure 2.6b.

Since the X-ray absorption of adsorbates on a surface is difficult to measure directly, one commonly quantifies the excitation cross section by one of its two decay channels: either by fluorescence or by Auger electron emission (Figure 2.6c).

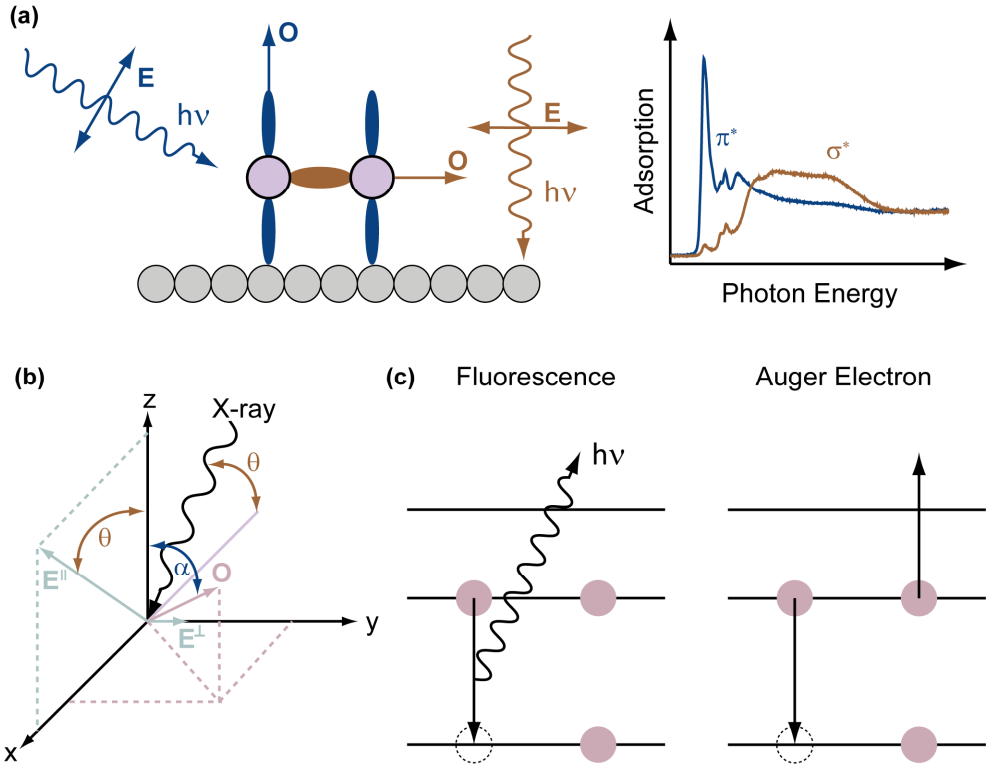

Figure 2.6: Schematic of angular dependence NEXAFS measurement for a π^* (dark blue) and σ^* (brown) antibonding orbital. The orientation of the orbital vector $\boldsymbol{O}$ and the vector $\boldsymbol{E}$ of the linear polarized X-ray radiation is given for both cases. On the right, exemplary NEXAFS spectra are shown, measured for the two indicated angles in the scheme on the left and colored as the respective orbital. (b) Orientations of the vectors $\boldsymbol{O}$ and $\boldsymbol{E}$ with z being the surface normal and the xy-plane the surface. Adapted from [77]. (c) Physical effect of fluorescence (left) and Auger electron emission (right) employed for detection in NEXAFS.

2.5 Normal Incidence X-ray Standing Wave

The X-ray standing wave (XSW) method is based on the same principles as Bragg diffraction in a crystal, where coherent incident and reflected X-ray waves combine to form a standing wave [81]. The Bragg condition is given by

$$n\lambda = 2dsin(\theta) \tag{2.17}$$

where λ is the wavelength, d is the distance between the scatter planes and θ is the angle of the incident light towards the surface. This necessitates the use of hard X-ray radiation with wavelengths on the order of crystal lattice distances. Nowadays, XSW is performed in normal incidence geometry (θ = 90°) to the Bragg plane, therefore, called normal incidence XSW [81].

The dynamical theory of X-ray diffraction is essential for understanding this phenomenon [81]. It considers the effect of multiple scattering events with a finite penetration depth [82]. In the absence of absorption, the kinematic theory predicts infinite reflectivity at the Bragg

condition, which contradicts flux conservation. The dynamical theory introduces the concept of extinction, resulting in finite total reflectivity over a range of incidence conditions, known as the Darwin curve [81-82]. Within this range, the phase of the standing wave shifts by π, influencing X-ray absorption at atomic sites. Near the low-energy end of the range, nodal planes coincide with atomic sites of the crystal plane, causing minimal absorption (Figure 2.7a,c), while at the high-energy end, antinodes lead to increased absorption (Figure 2.7b,c) [81]. The dynamics of X-ray absorption within the standing wave range provide insights into the atomic structure of solids. For absorbing crystals, the absorption behavior within the standing wave range is modified, impacting both the Darwin reflectivity curve (Darwin Prins curve) and the shape of the absorption curve (Figure 2.7c) [82].

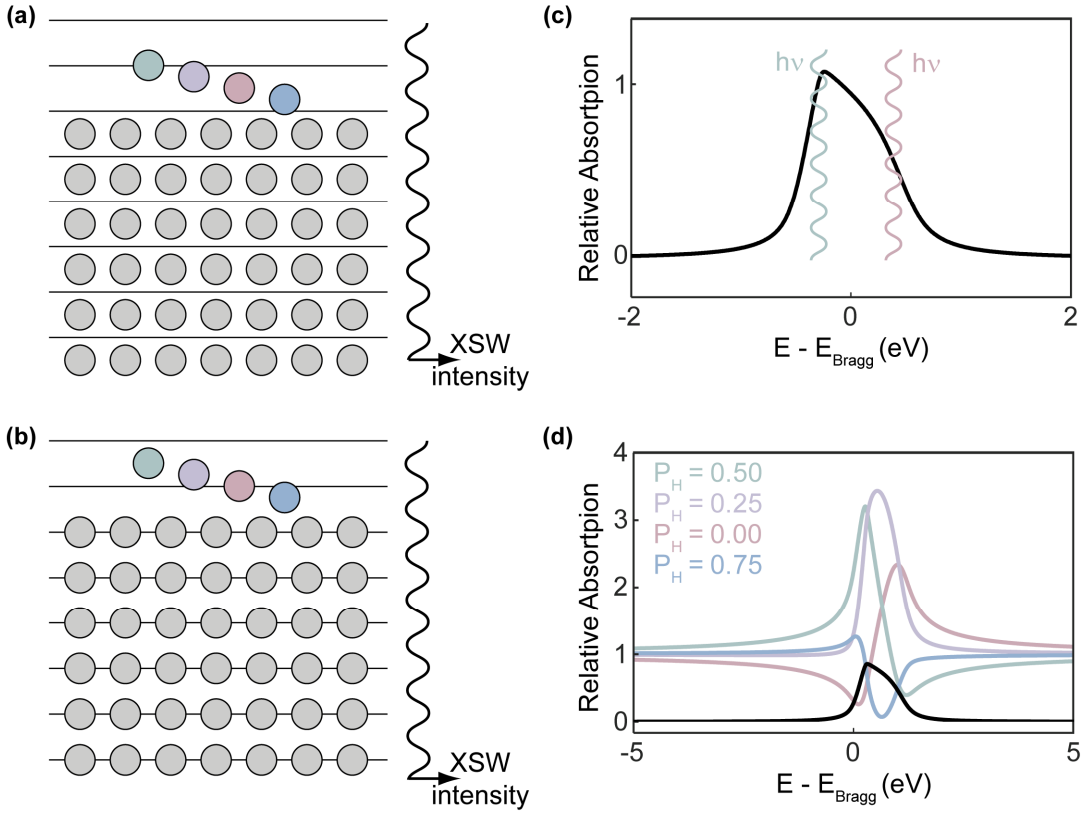

Figure 2.7: Schematics of the X-ray standing wave field (a) near the low-energy end and (b) near the high energy end of the range. (c) Shape of the Bragg reflection with absorption (black line). The red and green lines represent the energy of the incident photon for the cases represented in (a) and (b), respectively. (d) Theoretical deduced spectra for different coherent positions (P_H) and the reflectivity curve (black). The spectra are colored as the adsorbed atoms in (a) and (b), respectively. Adapted from [81, 83].

The theory behind XSW was established in the 1960s by *Boris W. Batterman* [82, 84]. The observed photoemission intensity I can be described by

$$I = 1 + R + 2\sqrt{R}\cos\left(\Phi - \frac{2\pi z}{d_H}\right), \qquad R = \left|\frac{E_r}{E_i}\right|^2 \tag{2.18}$$

with R being the reflectivity, E_i and E_r the incident and reflected X-ray amplitudes, z the perpendicular distance from the atomic scattering planes, d_H the separation of the atomic scattering planes and Φ the phase difference between the reflected and the incident wave [81]. Due to the lack of a single discrete z value, through e.g. vibrations or static and dynamic disorder, a distribution of z values has to be considered:

$$I = 1 + R + 2\,f_H\sqrt{R}\cos\left(\Phi - \frac{2\pi\,P_H}{d_H}\right) \tag{2.19}$$

where f_H is the coherent fraction and P_H is the coherent position [81]. The coherent position gives the average relative distance perpendicular to the scattering plane. It can have a value between 0 and 1. Figure 2.7d illustrates different coherent positions of adsorbed species and their respective spectrum. An adsorption height D_H can be determined by

$$D_H = (n + P_H) \cdot d_H, \qquad n = 0,1,2,\ldots. \tag{2.20}$$

Thus, multiple adsorption heights are obtained. These have to be assessed regarding their physical meaningfulness, often simplifying the interpretation to a single plausible one [81]. The coherent fraction gives the degree of uniformity of the adsorption height [81]. Its values are between 0 and 1. A value of above 0.75 is normally counted as a single adsorption height [85]. But, also, lower coherent fractions can give valuable insights for determining the investigated structure.

2.6 Temperature Programmed Desorption

Temperature programmed desorption is a technique employed for analysis of adsorbates and chemical reactions on surfaces [86]. A sample with adsorbates (e.g. molecules or atoms) is heated with a constant ramp:

$$T(t) = T_o + \beta t \tag{2.21}$$

where β is the heating rate, T_o is the starting temperature and t is the time of the heating ramp. The increase in partial pressure of the desorbing species is recorded in dependence of the temperature in a mass spectrometer. Typical heating rates are in-between 0.5 – 10 K s^{-1}. Assuming identical occupation sites and no interactions of the adsorbates, the Polanyi-Wigner-equation, given by

$$-\frac{d\theta}{dt} = \nu(\theta, T)\,\theta^n \exp\left(-\frac{E_{Des}(\theta, T)}{k_B T}\right), \tag{2.22}$$

can describe the desorption rate, where θ is the coverages of the desorbing species, E_{Des} is the desorption energy, ν is the frequency factor, k_B is the *Boltzmann* constant and n is the reaction order [87]. Combining equations (2.21) and (2.22) gives:

$$p \propto -\frac{d\theta}{dT} = \frac{\nu\,\theta^n}{\beta} \exp\left(-\frac{E_{Des}}{k_B T}\right). \tag{2.23}$$

In the case of high pumping speed, the partial pressure p, measured in the mass spectrometer, is proportional to the desorption rate $\frac{d\theta}{dT}$ [86]. The formula can be rationalized by considering two opposite trends [86]. At low temperatures, the exponential term is negligible, and its impact increases with rising temperature. However, at higher temperatures, the coverage diminishes, eventually reaching zero, resulting in the stop of the desorption process. For a non-activated chemisorption, the desorption energy equals the binding energy in the chemisorbed state. E_{Des} and ν are assumed to be independent of the coverage [87]. Nevertheless, in certain cases, such as adsorbates undergoing a phase transition [88], or due to repulsive interactions between the molecules or atoms, for instance, dipole-dipole interactions as observed for potassium ions on Fe single crystals [89-90], a coverage dependence of the desorption energy has to be considered.

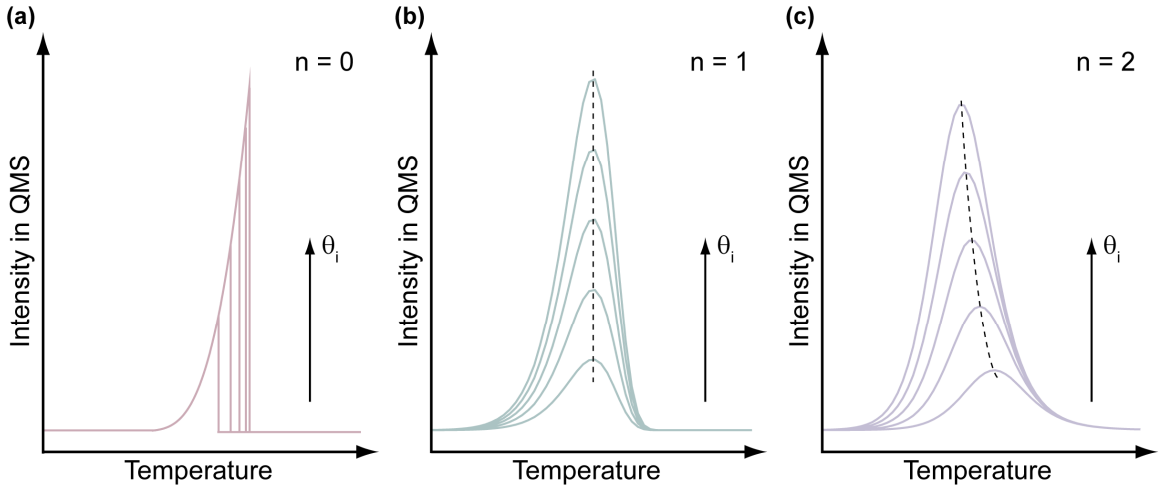

Figure 2.8: Schematics of simulated coverage-dependent desorption spectra of (a) zero-order, (b) first-order and (c) second-order kinetics.

The kinetic order provides valuable insights into the interactions and chemistry of the desorbing species [86]. The most general cases of the kinetic order of desorption are zero-order (n = 0), first-order (n = 1) and second-order kinetics (n = 2), though fractional orders are also observed. Examples of zero-order processes include multilayer desorption, while first-

order kinetics typically describe monolayer desorption from metal surfaces. Recombination of species on the surface, followed by desorption, is often characterized by second-order kinetics. The shape and its dependence on coverage can provide valuable insights into the anticipated desorption order n (Figure 2.8) [86]. Symmetric peaks usually indicate second-order desorption, while a decrease in reaction order results in more asymmetric peaks. In Figure 2.8 the coverage dependency is illustrated for the three kinetic orders. For first-order desorption, the position of the peak maximum remains independent of the initial coverage. For $n < 1$ ($n > 1$), the position of the peak maximum is shifted with higher coverages to higher (lower) temperatures, respectively. When other effects can be excluded, this shift provides means to determine the desorption order of the process [86].

2.7 Low Energy Electron Diffraction

Clinton Davisson's and *Lester Germer*'s experiments of electron scattering from nickel in the 1920s [91] lay the foundation for the development of low energy electron diffraction. *Davison* received the Nobel Prize in Physics in 1937 for these experiments [92]. In LEED, the diffraction pattern of a surface, which is hit by a low energy electron beam, is recorded. LEED uses electron with a *DeBroglie* wavelength λ in the range of atomic distances described by

$$\lambda = \frac{h}{\sqrt{2mE}} \tag{2.24}$$

with E being the energy of the electron, h the Planck constant and m the electron mass [93]. Wavelengths of the electrons are usually in-between 1 to 5 Å (E = 5 – 150 eV), enabling the investigation of diffraction patterns of surface structures. The mean free path of the electrons with these energies is just a few angstroms, thus, this technique is mostly surface sensitive [74]. For constructive interference, the *Laue* condition,

$$\boldsymbol{G} = k_f - k_i\,, \tag{2.25}$$

where $\boldsymbol{G}$ is the reciprocal lattice vector and k_i and k_f are the incident and diffracted wavevectors, respectively, has to be fulfilled [93]. This means, that if the change in the wave vectors needs to be equal to a reciprocal lattice vector. For electron diffraction, only the contribution of the top layer to the scattered intensity has to be considered, due to the small electron mean free path. This results in a modified *Laue* condition given by

$$\boldsymbol{G}_{\parallel} = k_{f,\parallel} - k_{i,\parallel}. \tag{2.26}$$

The reciprocal space picture is changed from reciprocal lattice points to a series of surface diffraction rods perpendicular to the surface [93].

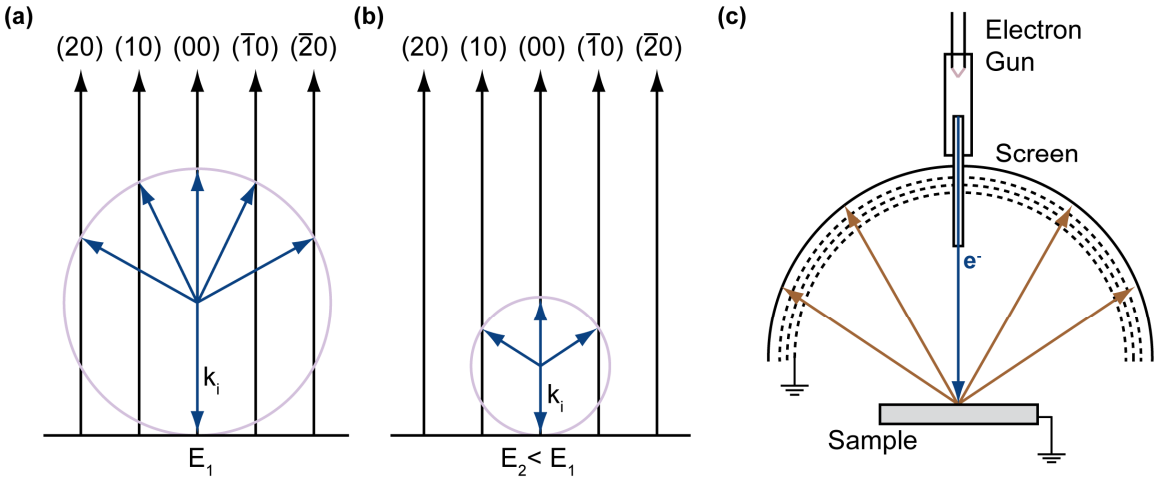

Figure 2.9: (a-b) Two Ewald spheres with different energies. (c) Schematics of a standard 3-grid LEED system. Adapted from [93].

The *Laue* condition can be visually represented by the *Ewald* sphere [93]. To illustrate, the incident wave vector is depicted with its endpoint coinciding with a reciprocal lattice point. A sphere is drawn with the radius of $|k_f|$ originating from the tail of k_i. This is because k_f and k_i have equal magnitude for elastic scattering. The *Laue* condition is met when this sphere intersects a reciprocal lattice point. In the context of LEED, the fulfillment of the *Laue* condition occurs when a reciprocal lattice rod intersects with the *Ewald* sphere (Figure 2.9a,b) [93].

A scheme of a standard 3-grid LEED system is shown in Figure 2.9c [93]. The electron beam is produced by an electron gun and directed towards the surface. The diffracted electrons encounter three grids before hitting a spherical fluorescent screen. The first grid is grounded, providing a field-free region in the scattering volume. Behind the first screen, two retarding grids filter out the inelastic secondary electrons. The elastic scattered electrons are then accelerated by 1 – 5 kV to the fluorescent screen. At normal incidence kin-para is zero and the elastic electrons scatter only in the directions of reciprocal lattice vectors [93]. Thus, the pattern of the reciprocal lattice of the surface is directly visible on the screen. A microchannel plate detector [94] can be used to increase the resolution of the LEED. However, through its non-spherical geometry, distortions are induced in the LEED pattern.

3 Instrumental Setup

This section outlines the setups and experimental procedures employed in this thesis. All experiments were performed under UHV conditions of $2 \cdot 10^{-10}$ mbar or lower.

3.1 VT-STM Setup with ES-CIBD System

This setup at the TUM, comprises three UHV chambers separated by gate valves. Two of these chambers are designated for sample preparation, with one connected to an ES-CIBD. The third chamber houses an Aarhus-type variable-temperature STM (VT-STM) from SPECS GmbH.

The home-built ES-CIBD setup is schematically outlined in Figure 3.1. ES-CIBD enables the deposition of molecules that are not sublimable by organic molecular beam epitaxy (OMBE) [32-33]. The combination with a mass filter in UHV excludes unwanted byproducts, giving a unique control over the deposited species. Beyond enabling the clean deposition of molecules, it introduces a novel approach through the choice of landing energy of the molecules on the sample, which shows promises, for example, in mechanochemistry [95].

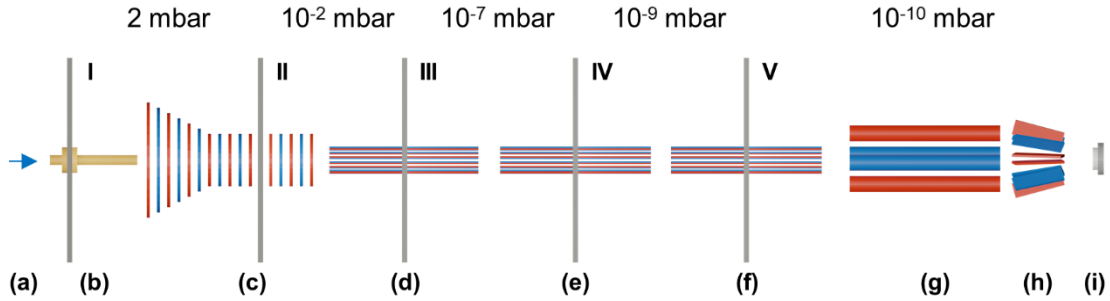

Figure 3.1: Schematic of the ES-CIBD system with (a) electrospray ionization, (b) capillary, (c) TWIN, (d-f) SIWGs, (g) dQMF, (h) blade, and (i) sample. The grey lines symbolize the interface between the vacuum chambers I to V. The corresponding pressure regime of a vacuum chamber is given above. Adapted from [34-35].

The ES-CIBD system consists of the electrospray ionization part (a) and five vacuum chambers (I-V), with pressures ranging from 2 mbar in chamber I to 10^{-10} mbar in chamber V (Figure 3.1) [34-35]. The molecules are dissolved and pumped through a small capillary, the so-called emitter. In the experiments, an uncoated fused silica with an inner diameter of 75 µm and outer diameter of 360 µm was used. A high voltage source sets the emitter to a defined potential. A capillary (b), featuring a funnel-shaped inlet followed by a small tube of around 6 cm ending in the first vacuum chamber, functions as counter electrode, generating a strong electric field to the tip of the emitter [96]. The charged droplets are accelerated in this field

towards the counter electrode. The first ion guide consists of a radiofrequencies (RF) ion funnel and ion tunnel (TWIN, (c)) to focus the ion beam and transfer it to vacuum chamber II. Three RF small wire ion guides (SWIGs, (d)-(f)), 16-pole ion guides, are transferring the ion beam further through chamber II to V. The advantages of using high number poles ion guides are a small ion beam, small pressure interfaces with reduced residual gas loads, low RF amplitudes, consequently, low RF heating of the beam and nearly loss free transportation of ions [34-35]. The beam is analyzed and filtered by a digital quadrupole mass filter (dQMF (19 mm system from Extrel), (g)) in chamber V, which is driven in a “digital” mode with square wave potentials instead of the commonly used sine shape potentials [34-35]. The final ion guide prior deposition is the BLADE (h) to focus the beam after the dQMF. A detailed discussion of this system can be found in [34-35].

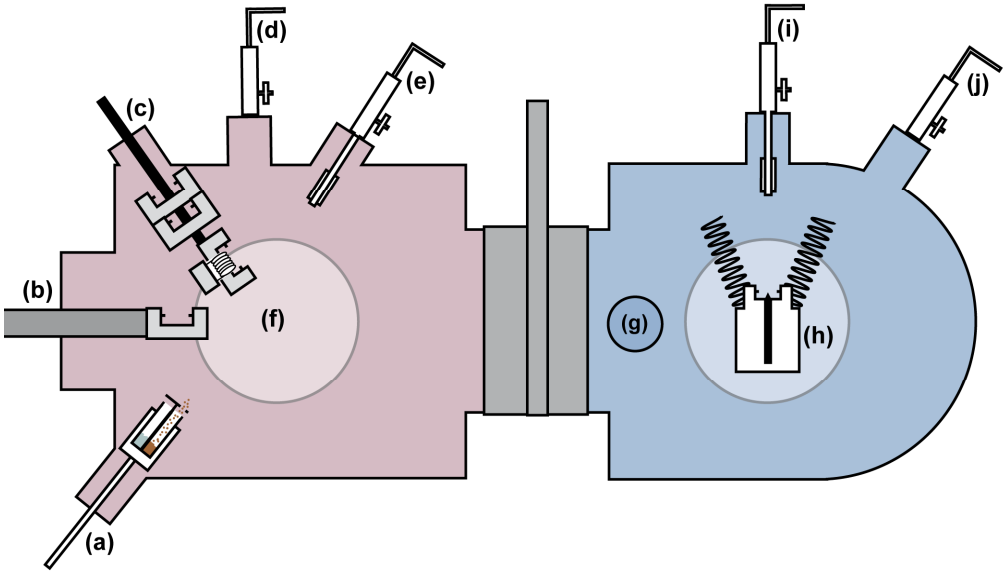

Figure 3.2: Schematic side view of the VT-STM apparatus. The preparation chamber is in red with (a) OMBE, (b) transfer arm, (c) a heating station with parking slots for up to four sample holders, (d) leak valve, (e) sputter gun, and (f) connection flange to the ES-CIBD system. The STM chamber in blue has (g) a load lock, (h) Aarhus type STM, (i) sputter gun, and (j) leak valves.

The preparation chamber of the ES-CIBD system is connected to a second preparation chamber (Figure 3.2, red), which was designed for a variety of different preparation methods, with the majority of flanges oriented toward the center of the chamber. It is pumped by a turbomolecular pump. For evaporation of organic molecules, an OMBE (a) can be mounted. There is further the option to mount metal evaporators. With the transfer arm (b), samples can be exchanged between preparation and STM chamber. For annealing and sputtering the sample as well as for storage, a combined heating station with e^- beam heating and parking for up to four sample holders (c) is used. There are several options to introduce gases (e.g. O_2) with leak valves (d). To obtaining clean, flat surfaces a sputter gun (e) with argon is

employed. Flange (f) connects the preparation chamber to the UHV chambers of the ES-CIBD system.

The STM chamber (Figure 3.2, blue) is pumped by an ion pump. New samples are introduced from ambient pressure *via* the load lock (g) without breaking the UHV in the STM chamber. The VT-STM (h) is in the center of the chamber, on which a sputter gun (i) is mounted for STM tip preparation. The bias is applied to the sample. Chemically etched tungsten tips are used. The chamber has several leak valves (j) for *in situ* preparation during scanning, for instance, with CO. The temperature range of the VT-STM for this research was between 100 K and 300 K. A SPC20 electronics (SPECS GmbH) is connected to the STM for acquiring the data.

3.2 Spectroscopy Based Setup

This chamber is a multifunctional setup for TPD, LEED, and XPS measurements at the TUM and was developed for photo-stimulated desorption (PSD). Figure 3.3 outlines the PSD system, which consist of two non-separable chambers – a preparation chamber (red) and an analysis chamber (blue). A manipulator (a), which is mounted to the preparation chamber, allows to freely position the sample in the two chambers by movement in the x, y, and z directions and rotation. The sample is attached to a home-built sample holder with radiative sample heating *via* filaments. The manipulator can also be cooled by liquid nitrogen (approximately 90 K). The temperature of the sample is measured by a K-type thermocouple and operated by a proportional-integral-derivative (PID) controller (Schlichting Physikalische Instrumente HIS 130). There are free flanges for OMBEs (b), a needle doser (c), and a sputter gun. The last two are connected to a gas dosage system with various gases (O_2, CO, Ar, Ne). A BDL800IR-LMX-ISH LEED (e) by OCI Vacuum Microengineering Inc. is also installed to the preparation chamber. A home-built X-ray tube with a twin Mg and Al anode (f) generating non-monochromatized Al and Mg Kα radiation of 1486.6 and 1253.8 eV, respectively, a gas discharge lamp for He(I) radiation (21.2 eV) and a SPECS Phoibos 100 CCD hemispherical electron energy analyzer (g) are mounted to the analyzer chamber for PES measurements. Customized Balzers QMA 140 quadrupole mass spectrometer inside a *Feulner* copper cap (h) is used for mass spectrometry [97]. The *Feulner* cap can be cooled with liquid nitrogen, which reduces the background of residual gases. A more elaborate description of this system can be found in [98].

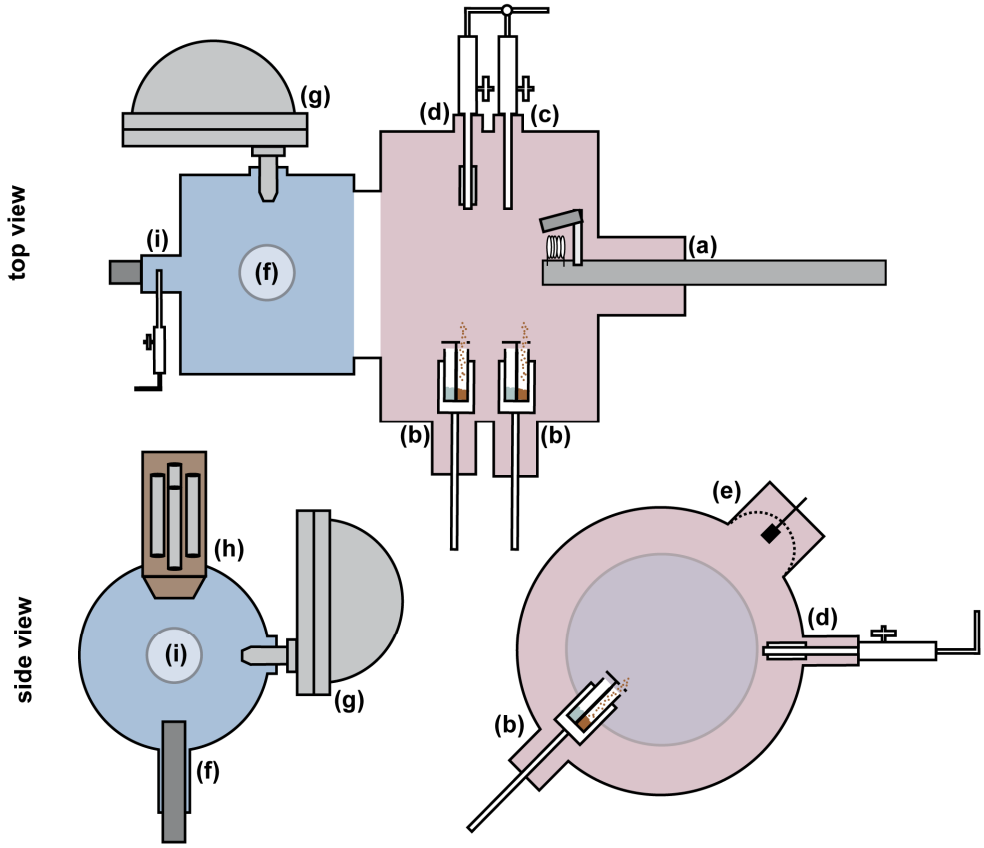

Figure 3.3: Schematic top and side view of the PSD chamber. The preparation chamber is red with (a) manipulator with integrated heating and cooling, (b) several evaporators, (c) needle valve and (d) sputter gun connected to the gas dosage system, and (e) LEED. The analysis chamber is in blue with (f) X-ray source, (g) analyzer, (h) mass spectrometer, and (i) He(I) gas discharge lamp.

3.3 Low Temperature STM Setup

This setup at the TUM consists of two main chambers and houses a combined low temperature STM (LT-STM)/non-contact atomic force microscope (ncAFM) instrument from CreaTec. The preparation chamber (red) and the analysis chamber (blue) are connected by a gate valve (Figure 3.4). A manipulator (a) with cooling is installed to transfer samples between the chambers and for sample preparation. The single crystals are mounted on commercial sample holders with a heating function (CreaTec). OMBEs (b), a sputter gun (c) and leak valves (g) are mounted to the chamber for sample preparation. The analysis chamber with the LT-STM/ncAFM instrument from CreaTec with a qPlus sensor in a cryostat system uses W tips. For noise reduction, the chamber is installed on a damping system. Further details can be found in [99].

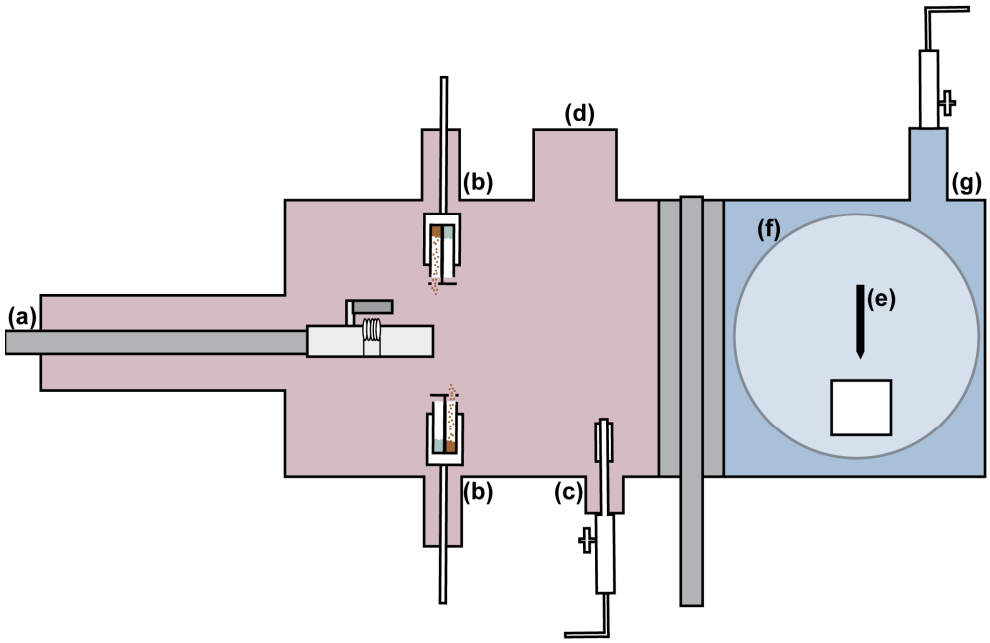

Figure 3.4: Schematic top view of the LT-AFM chamber with (a) a manipulator, (b) evaporators, (c) a sputter gun with Ar, (d) load lock entry to transfer samples, (e) LT-STM/ncAFM instrument in (f) a cryostat, and (g) a leak valve to dose CO.

3.4 End Stations in Synchrotrons

Data from several synchrotron light sources are included in this thesis. The setups are briefly described here. The preparation chambers of each setup are equipped with standard surface preparation tools such as sputter gun, leak valves (e.g. CO), sample heating and options to install evaporators for metals or organic molecules.

Photo-Emission and Atomic Resolution Laboratory (PEARL)

The PEARL beamline at the Paul Scherer Institute in Villigen, Switzerland, comprises five main chambers: two preparation chambers, a storage chamber, a chamber housing an LT-STM (Omicron) and an analysis chamber for PES. The analysis chamber is outfitted with a Scienta EW4000 hemispherical electron analyzer. For further details, see [100-101].

I09 Beamline

The permanent end station I09 at the Diamond Light Source (DLS) in Didcot, UK, consist of three UHV chambers: two for preparation and one for analysis, separated by gate valves. The manipulator in the main preparation chamber is also used for measurements in the analysis chamber, making sample transfer unnecessary. This configuration ensures continuous temperature control throughout both the preparation and measurement phases of the experiments. It can be cooled with liquid nitrogen or helium. Spectra are collected with a

Scienta EW4000 HAXPES analyzer, oriented perpendicularly to the incident X-rays in the horizontal plane of the photon linear polarization. Additionally, in the analysis chamber, a commercial OCI multichannel plate LEED apparatus is installed. Further details about the setup can be found in [102].

Flexible PhotoElectron Spectroscopy (FlexPES)

The permanent end station FlexPES in MAX IV in Lund, Sweden, consists of three chambers: two preparation chambers and one analysis chamber. On the main preparation chamber, an RGA mass spectrometer (MKS Microvision2) and LEED optics (BDL800 from OCI) are mounted. The main manipulator is utilized for both preparation and analysis, ensuring temperature control throughout the entire experiment. A hemispherical analyzer (DA30-L from ScientaOmicron) is connected to the analysis chamber. A more detailed description of the setup can be found in [103].

3.5 Sample Preparation

Substrate Preparation

In this thesis, Ag(111) and Cu(110) single crystals were employed. To achieve clean and atomically flat surfaces before depositions of molecules, cycles of sputtering with Ne^+ (only in PSD chamber) or Ar^+ (all other setups) and annealing to 650-750 K for Ag(111) or 700-800 K for Cu(110) were carried out.

bpp-COOH

The bpp-COOH molecules in Chapter 4 were provided by the *Ruben* group (*Prof. Mario Ruben*, *Dr. Nithin Suryadevara*, and *Dr. Senthil Kumar Kuppusamy*) (Figure 3.5a) [104]. After outgassing the molecules in vacuum, bpp-COOH was deposited *via* OMBE from a quartz crucible at 434 K on an Ag(111) crystal with a sample temperature of 300 K. Subsequently, the sample was heated to 373 K to obtain the self-assembly.

Foldamers

The oligoamides of 8-amino-2-quinoline-carboxylic acid foldamers (Q_n (NO_2 rest) and pyr-Q_n (pyrene rest)) in Chapter 5 were synthesized by the *Huc* group (*Prof. Ivan Huc*, *Dr. Jinhua Wang*, *Dr. Xuesong Li*, *Dr. Frédéric Rosu*, *Dr. Valérie Gabelica*, and *Dr. Victor Maurizot*) (Figure 3.5b) [105-108].

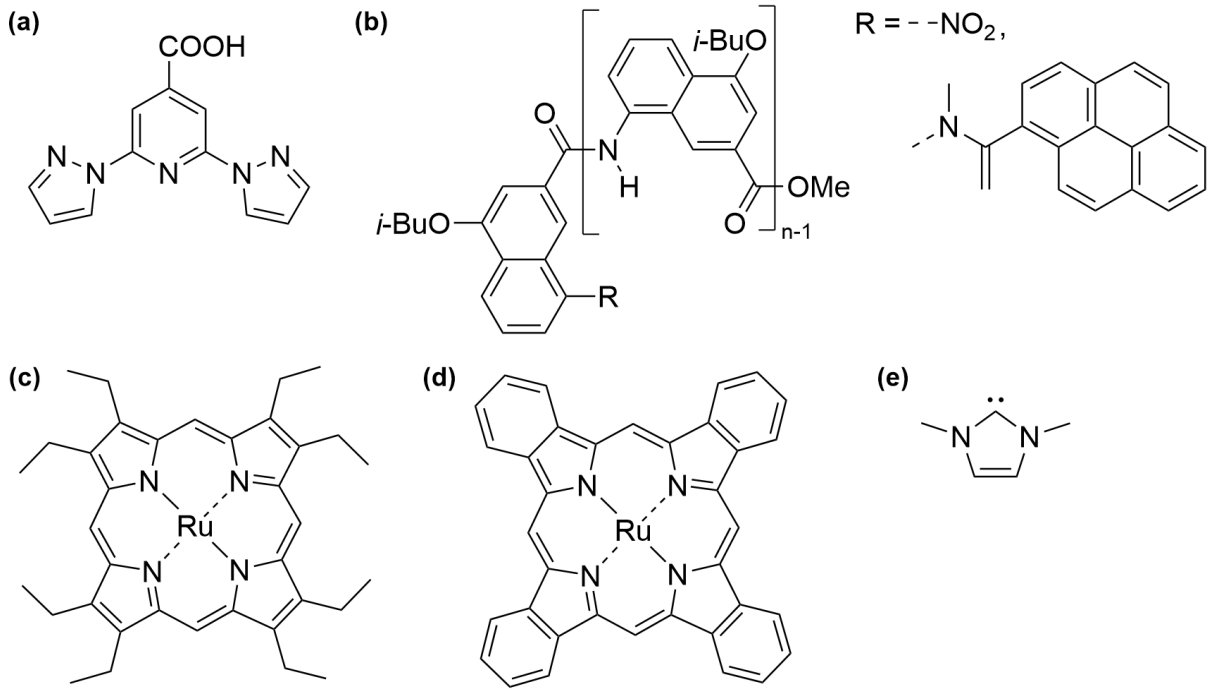

Figure 3.5: Structural formulas of (a) bpp-COOH, (b) foldamers Q_n (NO_2 rest) and pyr-Q_n (pyrene rest), (c) Ru-OEP, (d) Ru-TBP and (e) IMe.

The employed foldamers, pyr-Q_4 and pyr-Q_7, differ in the number of quinoline monomers (4 and 7). The three-dimensional structure of pyr-Q_4 is shown in Figure 3.6. The foldamers were dissolved in a mixture of acetonitrile (69 vol%) methanol (29 vol%) and acetic acid (2 vol%) and deposited *via* ES-CIBD [109]. The foldamers were positively charged by a proton. Methanol was added to stabilize the electrospray of the foldamer solution. The sprayed solutions had a concentration between 10^{-4} to 10^{-5} mol l^{-1}. The emitter voltage was set to approximately 5 kV with a flow rate of 60–90 µl/h.

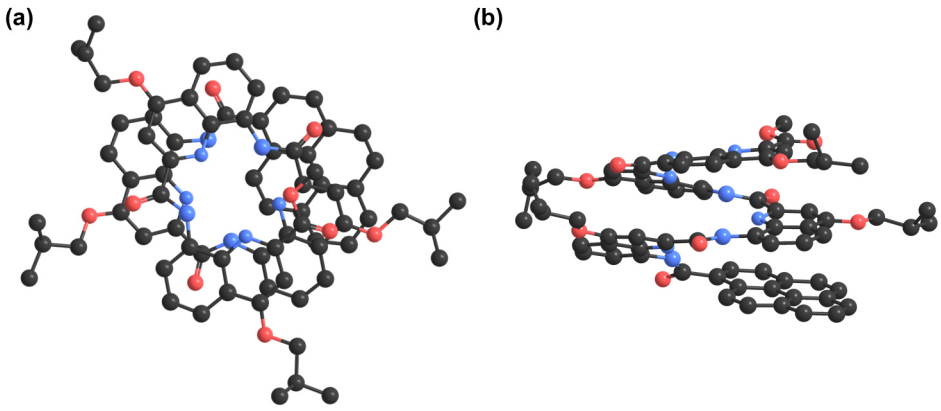

Figure 3.6: (a) Top and (b) side view of the structural model derived from the crystal structure of pyr-Q_4. Oxygen, nitrogen, and carbon are in red, blue, and black, respectively. The hydrogens are omitted for clarity. Additional structural information is given in reference [109].

Porphyrins

Following outgassing of the molecular precursor in UHV, Ru(CO)-OEP (purchased at Sigma-Aldrich) was deposited *via* OMBE by heating the crucible at 490 to 540 K. Ru-OEP (Figure 3.5c) was deposited on the Ag(111), Cu(110) or Cu(110)-(2×1)O surface at RT. The high coverage phase of Ru-OEP was achieved either by controlling the deposition time or by preparing a multilayer followed by annealing to 500 K to desorb all but the first layer. In the multilayer on Cu(110)-(2×1)O, a new peak in the O 1s core level at 533 eV was detected, which corresponds to oxygen in CO (Figure 3.7) [110]. We can, thus, conclude that the CO is still bound to the Ru center after evaporating the molecules from the crucible. The Ru-TBP (Figure 3.5d) was obtained by Ru-OEP deposition on Ag(111) at 700 K. Comparable procedures were described with octaethyl porphyrins and octaethyl tetra-aza-porphyrins on different substrates [111-113]. The completeness of the ring closure reaction was either observed by STM or by a combination of XPS and LEED.

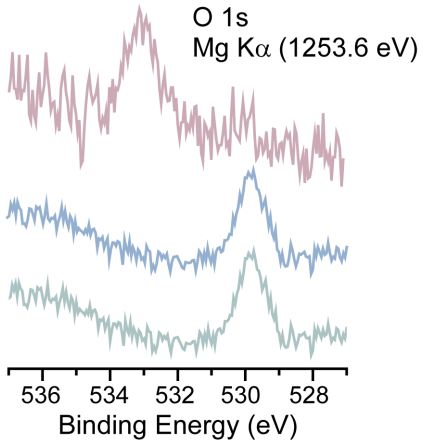

Figure 3.7: O 1s core level spectra of multilayer Ru-OEP (red) and monolayer Ru-OEP (blue) on Cu(110)-(2×1)O. For reference, a spectrum of a clean Cu(110)-(2×1)O surface is provided (green). Note that the multilayer O 1s XP spectrum comprises only two scans, resulting in a high noise level.

CO exposure

CO (Westfalen AG, purity % >99.997) was dosed using either a gas dosage system with a needle doser (in the PSD chamber) or leak valves (in all other setups). The pressure during dosage with a leak valve was between $5 \cdot 10^{-9}$ and $1 \cdot 10^{-8}$ mbar. In the experiments with Ru-OEP and Ru-TBP on Ag(111) in Chapter 7, $C^{12}O^{18}$ was utilized.

Carbene

The precursor of IMe (Figure 3.5e), CO_2-IMe, was synthesized by *Dr. Guillaume Médard* [44]. The carbene was deposited by OMBE at a temperature ranging from 360 to 380 K. Scheme 3.1 describes the decomposition of the CO_2-IMe molecules during evaporation.

Scheme 3.1: Masked CO_2-IMe to IMe and CO_2 decomposition during heating in the OMBE prior deposition in UHV [44].

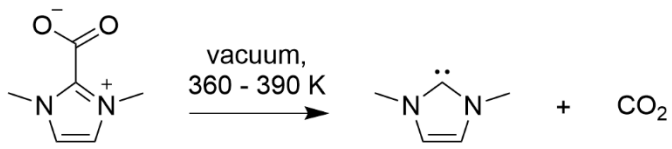

3.6 Data Acquisition and Analysis

STM

The STMs were operated in a constant current mode. The tunneling parameters and sample temperatures are provided with the STM data. The reported bias is the sample bias. The low temperature STM images in Chapter 4 were obtained at the PEARL end station by *Dr. Peter Knecht*. the LT-STM data from Chapter 6 and 7 was taken at the LT-STM/ncAFM setup and all the STM data from Chapters 4 to 8 in the temperature range of 100 K to RT was measured at the VT-STM setup. For the STM data evaluation, a combination of Gwyddion [114], routines for Igor pro 6.3 implemented by *Dr. Peter Knecht* [83], and SpmImage Tycoon [115] were used. The STM data of the VT-STM was calibrated with parameters obtained by atomic resolution images of the corresponding substrate with routines for Igor pro 6.3, also implemented by *Dr. Peter Knecht* [83].

LEED

The evaluation of the LEED data was performed with the help of LEEDpat software by *K. Hermann* and *M. A. Van Hove* (https://www.fhi.mpg.de/958975/LEEDpat4).

PES

The presented XPS data for the bpp-COOH network (Chapter 4) were acquired by cooperation partners (*Dr. Peter Knecht*, *Dr. Francesco Allegretti*, *Dr. Keitaro Eguchi*, and *Dr. Mathias Muntwiler*) in the PEARL beamline. Excitation energies of 400 eV were employed for acquiring the C 1s spectra, while O 1s spectra were obtained with excitation energies of 640 eV. The energy scales were calibrated using the Ag $3d_{5/2}$ line at 368.27 eV (O 1s spectra) or the Fermi edge (C 1s spectra).

The XPS and UPS data for Ru-OEP and Ru-TBP (Chapter 6 and 7) was obtained at the I09 and FlexPES beamlines at 200 K. A photon energy of $h\nu$ = 550 eV (N 1s core level), $h\nu$ = 450 eV (Ru 3d and C 1s core levels) or $h\nu$ = 135 eV (valence band) was used. The binding energy was calibrated with the corresponding Fermi edge. For the fits of the C 1s core level, a Shirley background was subtracted, and Voigt functions were employed to fit the individual

peaks. The here-presented spectra of the N 1s core level and the valence band aren't further processed after calibration. The work function changes were determined by secondary electron cutoff measurements in the PSD setup with non-monochromatized Al Kα radiation (hν = 1486.6 eV).

The XPS and UPS data of Ru-OEP on Cu(110) and Cu(110)-(2×1)O (Chapter 8) were obtained in the PSD setup with non-monochromatized Mg Kα radiation (hν = 1253.6 eV) in normal emission geometry. The data was calibrated by the Cu $3p_{3/2}$ core level with an energy of 932.7 eV. The data of Ru-OEP monolayers and the multilayers on Cu(110) and Cu(110)-(2×1)O were acquired at RT or 200 K.

TPD

All TPD experiments in this thesis were performed in the PSD chamber. For evaluation of the TPD data, Matlab routines implemented by *Dr. Peter Knecht* and *Dr. Peter Deimel* were used for import, background subtraction and normalization of the coverage [83]. For the IMe TPD spectra, it was assumed that the desorption curves conform to the Polanyi-Wigner equation. The shift of the maximum desorption temperature can be modelled by a coverage-dependent desorption energy $E_d(\theta)$. For Ru(IMe)-TBP/-OEP on Ag(111), a simple relation was chosen for the fit:

$$E_d(\theta) = E_d(\theta_0) - E_{des}\theta \tag{3.1}$$

where $E_d(\theta_0)$ is the desorption energy in the limit of zero coverage characterized by absence of lateral interaction and E_{des} is the coverage dependent component of the desorption energy [90]. For Ru(IMe)-OEP/Cu(110), a model proposed by *Albano,* for similar observed repulsive interactions, was employed:

$$E_d(\theta) = E_d(\theta_0) - \frac{9P^2\theta^{3/2}}{(1+9\alpha\theta^{3/2})^2} \tag{3.2}$$

where α is the polarizability and P is the magnitude of the dipole moment [90]. An assumed frequency factor of 10^{-15} s^{-1} was used to ensure comparability with the desorption of IMe on ruthenium tetraphenyl porphyrin (Ru-TPP) on Ag(111) [42].

NIXSW

The measurements of the Ru porphyrins on Ag(111) were performed with the help of *Dr. David Duncan*, *Dr. Anthoula Papageorgiou*, *Dr. Fulden Eratam*, *Pablo Vezzoni Vincente*, and *Hongxiang Xu* in the permanent end station I09 in DLS. A normal-incidence Bragg energy of hν = 2.63 keV was chosen for the (111) planes. Sequential measurements were performed at different spots on the sample. The reflectivity curve was acquired each NIXSW measurement

to precisely align the energy for individual NIXSW measurements and confirm the crystalline quality of Ag(111). XP spectra from the C 1s and Ru 3d regions were acquired before and after each NIXSW measurement and compared to each other to exclude potential beam damage. The data were evaluated by Matlab fitting procedures implemented by *Dr. David Duncan* and *Pablo Vezzoni Vincente*.

NEXAFS

The here presented NEXAFS data of the ruthenium porphyrins were taken with the help of *Dr. Alexander Generalov*, *Dr. Alexei Preobrajenski*, *Dr. David Duncan*, *Dr. Anthoula Papageorgiou*, and *Dr. Fulden Eratam* in the FlexPES beamline with partial electron yield detection. All measurements were performed at 200 K. For all systems, five different incidence angles θ between the surface normal and the **E** vector of the linearly polarized light with an assumed polarization P of 90% were measured (30°, 45°, 60°, 75° and 90°). At least three spectra for each angle were taken. Standard procedures for evaluation of the NEXAFS data sets were employed [77, 80]. The process involved subtracting the bare crystal signal from the sample spectrum, subsequently correcting for photon flux, and normalizing the edge jump to a value of one. Gaussians and asymmetric gaussians were used to fit the π^* and σ^* resonances in the spectra, respectively. For the determination of the tilt angle, the formula for a threefold symmetry or higher was employed to fit the angle dependent NEXAFS intensity [77].

IMS

The IMS data in Chapter 5 were acquired with an Agilent 6560 DTIMS-Q-TOF instrument (Agilent Technologies, Santa Clara, CA), and provided by the *Huc* group [109].

Density Functional Theory

The *Narasimhan* group (*Dr. Abhishek K. Adak*, *Dr. Sourav Mondal*, and *Prof. Shobhana Narasimhan*) conducted DFT calculations on the bpp-COOH network of Chapter 4 [104] using the Quantum ESPRESSO package [116]. The calculations employed a plane wave basis set with cut-offs of 40 Ry and 400 Ry for wavefunctions and charge densities, respectively [117]. Ultrasoft pseudopotentials described interactions between ionic cores and valence electrons [118], while the Perdew-Burke-Ernzerhof (PBE) form of the Generalized Gradient Approximation was used for exchange-correlation interactions [119]. Grimme's DFT-D2 method incorporated dispersion (van der Waals) interactions [120]. The Ag(111) support was modeled with a three-layer slab, and a vacuum spacing of approximately 15 Å was introduced in the z-direction (perpendicular to the surface). Brillouin zone sampling was limited to the zone center (Γ) for large unit cells containing the adsorbed molecules on Ag(111). Convergence was

aided by employing the Marzari-Vanderbilt smearing technique, with a width of 0.005 Ry [121]. All atomic coordinates, except for those in the bottommost Ag layer, were allowed to relax using the BFGS algorithm, except for constrained-minimization calculations used to determine the rotation barrier [122-125]. The force convergence threshold was 0.03 eV $Å^{-1}$ [126]. The Bader charge-partitioning method was utilized to calculate the charge transfer between guest molecules and the kagome network [127-128].

4 Rotation in an Enantiospecific Self-Assembled Array of Molecular Raffle Wheels

This chapter includes content that has been published in
Meier, D.; Adak, A. K.; Knecht, P.; Reichert, J.; Mondal, S.; Suryadevara, N.; Kuppusamy, S. K.; Eguchi, K.; Muntwiler, M. K.; Allegretti, F.; Ruben, M.; Barth, J. V.; Narasimhan, S.; Papageorgiou, A C., Rotation in an Enantiospecific Self-Assembled Array of Molecular Raffle Wheels. *Angew. Chem. Int. Ed.* **2021**, *60* (52), 26932-26938. Reproduced with permission from Wiley-VCH.

Inspired by biomolecular rotors that are omnipresent in nature, artificial molecular rotors have drawn attention in nanoscience due to their potential application as functional molecular nanomachines. Mounting such devices on a surface in analogy to natural motors which operate at interfaces can expand their applicability. This has triggered intense scientific interest in the last couple of decades [129-135]. The pioneering work of *Gimzewski* and co-workers demonstrated and established a methodological approach for the characterization of such rotors by combining real space visualization by STM with theoretical studies [136]. It has been shown that the molecular motion on surfaces can be tuned by molecule-substrate interactions [137-138], as well as by supramolecular interactions [139-141]. While isolated rotors have been the subject of intensive investigations, molecular rotors' programmed assembly and motion are less explored, despite having advantages in applications such as novel sensors and signal processing [142]. Different approaches have been shown to achieve this goal, including the use of bimetallic dislocation networks [143-144] and molecular networks [145-150], to control the positioning of molecular rotors directly on the surface, as well as the 2D self-assembly of molecular platforms, which were utilized for the arrangement of axially attached rotating units [151-152]. Here, we will demonstrate the regular assembly and motion of caged molecular rotors with enantiospecific stationary positions. An in-depth analysis will reveal that the energy landscape of the rotation is influenced by a combination of hydrogen bonds to the host and site-specific molecule-substrate interactions.

Results and Discussion

The investigation commenced with the discovery of an intriguing self-assembly when depositing bpp-COOH on Ag(111). Initial attempts to image the molecules using STM at 200 K and above, subsequent to RT deposition, were hindered by the high mobility of the molecules. However, upon annealing at 373 K, a stabilized complex arrangement emerged, allowing

imaging at RT (Figure 4.1a). The corresponding fast Fourier transform (FFT) of the STM image reveals long-range periodicity (Figure 4.1b). These distinct spots correspond to a unit cell which can be approximated by the epitaxial matrix of $\begin{pmatrix} 8 & 2 \\ -2 & 6 \end{pmatrix}$ on the Ag(111) lattice, corresponding to a hexagonal overlayer twisted anticlockwise by 14° with respect to the substrate lattice [153].

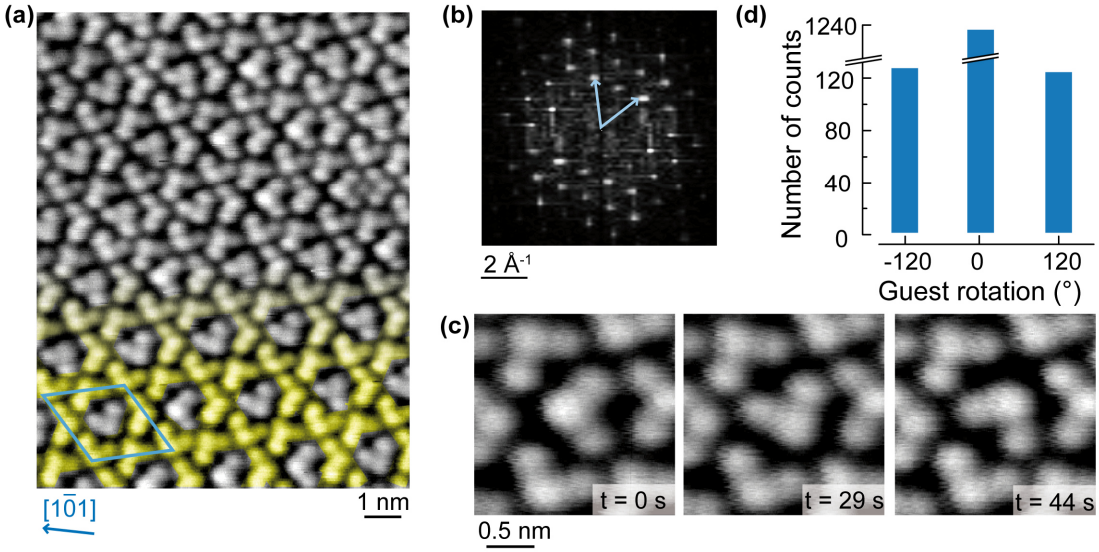

Figure 4.1: (a) Overview STM image of bpp-COOH on Ag(111) after annealing to 373 K (−625 mV, 40 pA, RT). The kagome network is highlighted in yellow on the bottom half of the image. The blue arrow indicates an Ag high symmetry axis in real space. (b) Corresponding FFT. The light blue vectors identify the unit cell. The same unit cell is indicated on the real space data in (a). (c) Consecutive STM images reveal different positions for the molecule in the larger kagome pore (-625 mV, 10 pA, RT). (d) Count of switching event of ±120° between consecutive images (around 15 s between images). Adapted from [104].

Correlating the reciprocal space periodicities to the real space data, we identify a motif containing four molecules. Three of these molecules are arranged regularly in a kagome pattern, highlighted in yellow in Figure 4.1a. The fourth one appears in the pore of the kagome pattern. The orientation of the molecules in the pores is non-periodic, causing a local disturbance in the long-range order [154]. Consecutive images revealed alterations of the same guest molecule between different orientations (Figure 4.1c and Appendix, Figure A.1). In contrast to a Brownian ratchet, no preferred directionality of the switching is expected for the thermally activated motion of the guest molecule in thermal equilibrium [155]. An analysis of the rotational events showed no clear preferential direction (Figure 4.1d). Thus, the kagome arranged molecules are considered as a 2D matrix hosting single guest molecules in various orientations, reminiscent of the assemblies of a triangular discotic liquid crystal on graphite [145] and trimeric supramolecules of bisphenol A on Ag(111) [149].

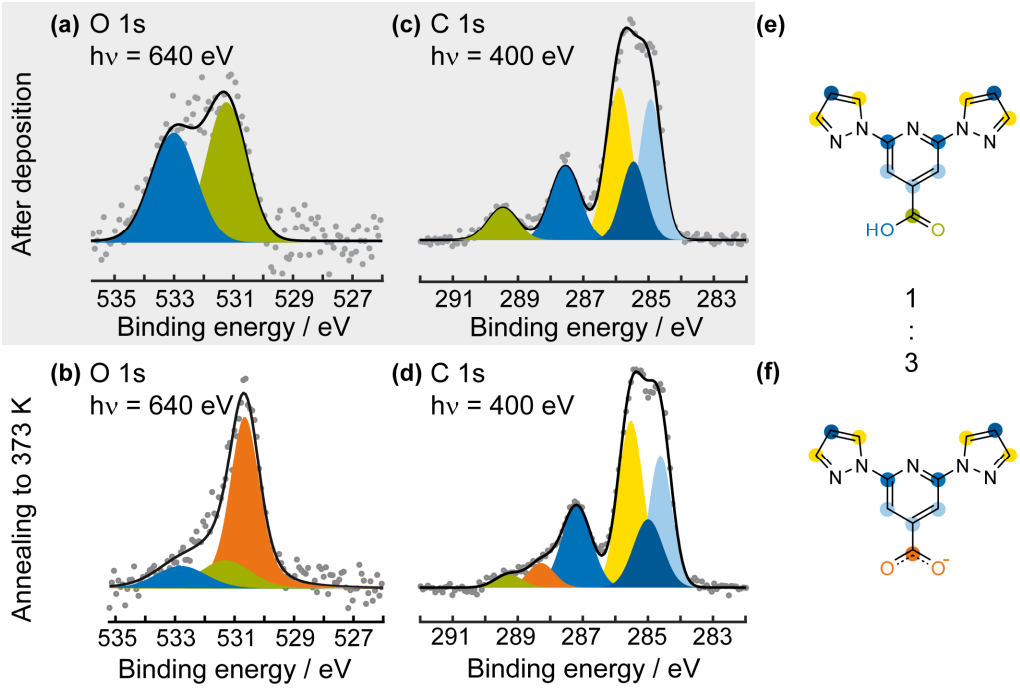

Figure 4.2: Fitted O 1s and C 1s core-level spectra corresponding to a single layer of bpp-COOH on Ag(111) after deposition at RT (a,c) and after annealing to 373 K (b,d). The spectra are deconvoluted into components assigned to the chemically inequivalent atoms as marked by the color indications in the chemical formulas of (e) bpp-COOH and (f) bpp-COO⁻. Adapted from [104].

To compare the molecular chemical state before and after annealing to 373 K, XPS analysis was conducted on the O 1s and C 1s core level region (Figure 4.2). The O 1s signal before annealing exhibits two peaks in a nearly 1:1 ratio, consistent with signals from the hydroxyl and the carbonyl O atoms of the carboxylic acid moiety of bpp-COOH (Figure 4.2a). After annealing, the signal comprises three components in ratios of approximately 6:1:1, in order of increasing binding energy. The higher binding energy components, again in a ratio of 1:1, can be attributed to bpp-COOH moieties, while the lower binding energy component can be assigned to O atoms in carboxylate moieties - bpp-COO⁻ (Figure 4.2b) [156]. The C 1s signal (Figure 4.2c,d) further supports the change upon annealing from carboxylic acid (green) to carboxylate (orange) moieties with a ratio of approximately 1:3 after annealing, due to a new signal at 288.3 eV. Considering the same 3:1 ratio of “stators” and “rotors” within the self-assembled kagome structure, we deduce that the “rotors” correspond to pristine bpp-COOH molecules (Figure 4.2e), while the “stators” are chemically modified bpp-COO⁻ molecules (Figure 4.2f). Consequently, we may associate the stabilization of the structure after annealing to 373 K with the formation of the carboxylate species, which are not initially present after the RT deposition of bpp-COOH.

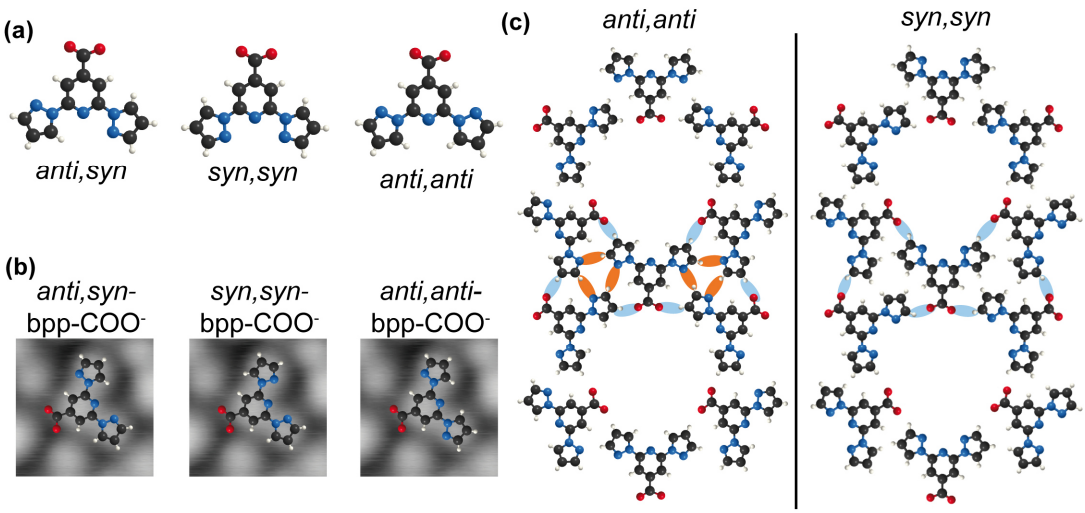

Figure 4.3 (a) Ball-and-stick models of possible bpp-COO⁻ rotamers. (b) Plausible planar bpp-COO⁻ surface rotamers, indistinguishable by STM. (c) Comparison of hydrogen bonding schemes of an *anti,anti* and a *syn,syn* kagome network. The blue ellipses show hydrogen bonds. In the *anti,anti* kagome network the orange ellipses show possible additional hydrogen bonds. C, N, O and H atoms are shown in black, blue, red and white, respectively. Adapted from [104].

After identifying the chemical state of the molecular components, we analyzed their relative arrangement. From the STM contrast, we can identify the orientation of the pyridine-carboxyl moiety, hereafter called head group. However, the pyrazole orientation is not directly evident, and similar contrast can arise from different planar rotamers (Figure 4.3a,b). The highly symmetric nature of the kagome network suggests *syn,syn*- or *anti,anti*-configurations of the N atoms in adjacent pyridine-pyrazole units. As the *anti-anti* conformation is the most stable in the solid state [157], we do not expect the emergence of an alternate rotamer after RT deposition.

Table 4.1: Adsorption energy of the pristine and deprotonated *anti,anti*-rotamer at different adsorption sites on Ag(111), as calculated by DFT.

Adsorption site (pyridine)	Isolated bpp-COOH	Isolated bpp-COO⁻
FCC hollow	0.0 eV	0.0 eV
HCP hollow	0.03 eV	0.036 eV
Atop	0.036 eV	0.028 eV
Bridge	0.059 eV	0.057 eV

However, to ensure that this is also the preferred conformation of the deprotonated molecule on the surface, DFT modelling of the supramolecular network on Ag(111) with both configurations was performed. The fcc hollow site was determined as energetically favored for the pyridine of both *anti,anti*-bpp-COOH and bpp-COO⁻ (Table 4.1) and was used to position the molecular units forming the kagome structure on Ag(111). The *anti,anti*-structure is favored by 1.86 eV per unit cell. A comparison of the hydrogen bonding schemes of the kagome

syn,syn- and the *anti,anti*-rotamers can rationalize a large energy difference between the two structures (Figure 4.3c). Furthermore, the DFT-derived preferred orientation of the guest molecule aligns with the STM images for the *anti,anti*-configuration (Figure 4.4), while the *syn,syn*-molecule's orientation predicted by DFT does not correspond to the observed orientation in STM (see Appendix, Figure A.2). Moreover, the theoretically simulated STM images, obtained from DFT calculations, also reproduce the relative contrast difference of the head group compared to the pyrazole side groups. The pyridine-carboxylic acid appears brighter than the pyridine-carboxylate, reaffirming the assignment of chemically modified bpp-COO^- tectons constituting the 2D kagome pattern on Ag(111) (Figure 4.4b,c).

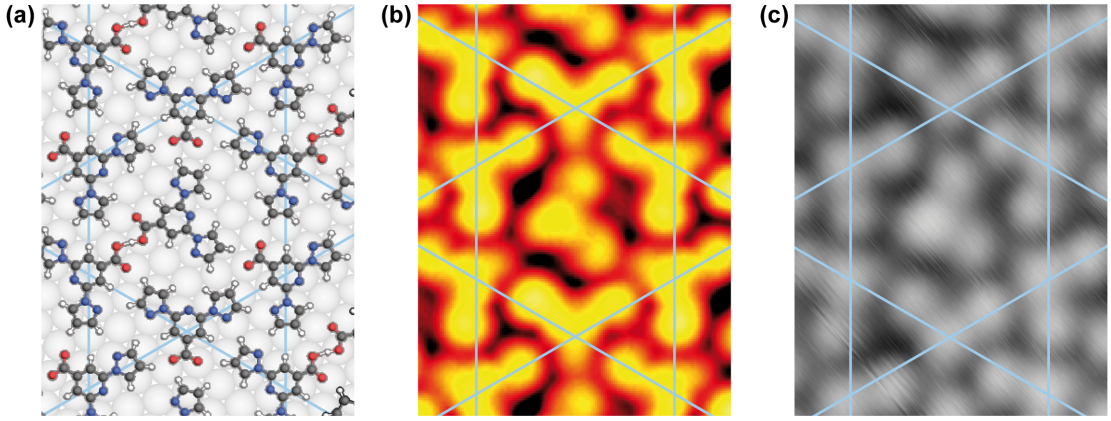

Figure 4.4: (a) Ball-and-stick model of the DFT optimized geometry. C, N, O, H, and Ag atoms are displayed in black, blue, red, white and grey, respectively. (b) Simulated constant current STM image (-500 mV). (c) Experimental STM image (-500 mV, 50 pA, 4 K). The kagome network is indicated in all images by blue lines. Adapted from [104].

Subsequently, we analyzed the orientation of the guest molecules in our "frozen" system (Figure 4.5a) by inspection of STM images acquired at 4 K (Figure 4.5b). In general, this is found to be within 15º of the head-to-head orientation between the guest molecule and the host species. We expressed this as the angle of rotation of the guest molecule within the pore, with 0° being a guest carboxylic acid to host carboxylate head-to-head arrangement (indicated in the blue frame of Figure 4.5a). Remarkably, we found a clear signature of an enantiospecific interaction for the guest molecules: 71% were rotated clockwise, 26% were not rotated and 3% were rotated anticlockwise. The clockwise angle (**CW**, orange in Figure 4.5a) implies that the carboxylic H atom is expressed predominantly as a single surface enantiomer. It should be noted that bpp-COOH is an achiral molecule, but confinement of the carbonyl carbon of bpp-COOH to the surface plane gives rise to two surface enantiomers depending on the position of the carboxylic H atom. For the remaining molecules, the position of the carboxylic H atom of the bpp-COOH guest cannot be deduced from the orientation (26%, blue in Figure 4.5a), whereas only 3% exhibit clearly the anticlockwise bpp-COOH enantiomer (**ACW**, green

in Figure 4.5a). Therefore, the host network induces chiral organization of the guest molecules. The origin of this effect can be found by looking at the registry of the kagome network on the substrate.

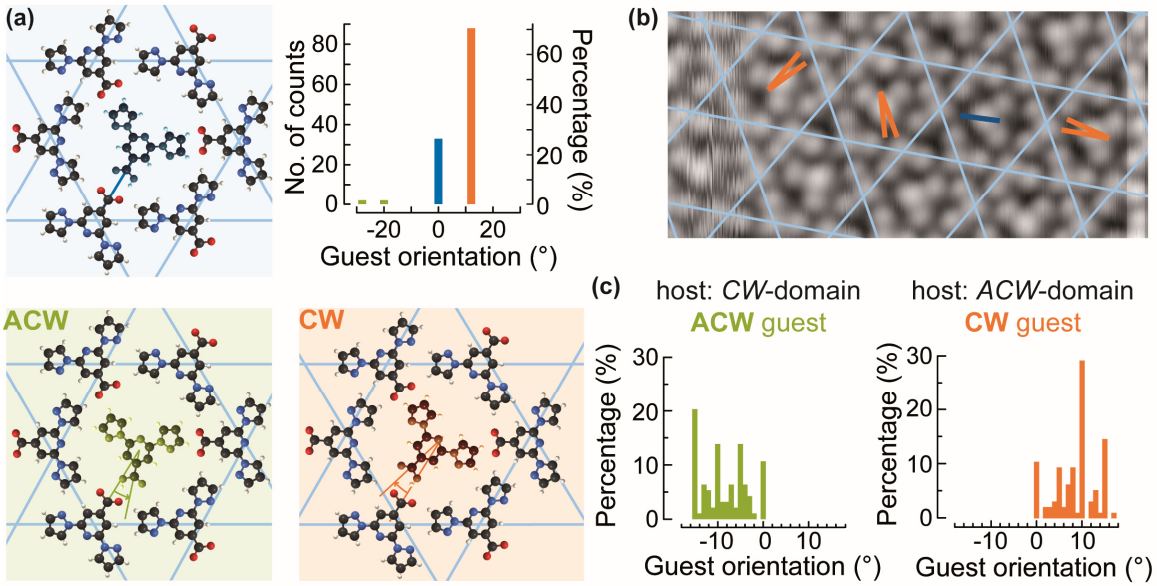

Figure 4.5: (a) Analysis of the clockwise rotation of guest molecules with respect to the nearest neighboring host for head-to-head orientation in *ACW*-domains at 4 K. The histogram of the orientation of guest molecules has a bin width of 3°. The schematics illustrate different bpp-COOH enantiomorphs of the guest molecules based on their detected geometry with respect to the kagome network. The guest molecules are colored green (**ACW**), orange (**CW**) and blue (unidentified), to represent the different **ACW** and **CW** adsorbed bpp-COOH enantiomorphs. (b) Exemplary determination of the orientation of guest molecules in an *ACW*-kagome network domain at 4 K (-500 mV, 50 pA). The lines indicate a head-to-head orientation (dark blue) or a +15° angle of clockwise rotation (orange) of the guest to the host. The kagome network is indicated by light blue lines in (a) and (b). (c) Analysis of the orientation of guest molecules with respect to the nearest neighboring host for head-to-head interaction in *CW*-domains (left) and *ACW*-domains (right) at RT. The histogram of the orientation of guest molecules has a bin width of 1°. Adapted from [104].

Enantiospecific molecular interactions on solid surfaces may stem from chiral steps or kinks [158-159] or by molecular chiral modifiers [160-161]. Unlike other reported 2D kagome networks [162-165], the one reported here is (if considering the unsupported layer) achiral, as is the bare Ag(111) surface. The origin of the enantiospecific interaction can be found in the twist when superposing the supramolecular structure to the substrate symmetry [166]. Indeed the superposition of two layers with a twist angle has been shown to give rise to chiral films [167] with topologically protected chiral 1D edge states [168]. Here, the rotated registry of the kagome network with respect to the substrate gives rise to *CW*- and *ACW*-domains of the kagome network, which correspond to clockwise and anticlockwise rotations, respectively, of the kagome network with respect to the substrate lattice vectors (Figure 4.6a). Figure 4.5a shows an analysis of solely *ACW*-domains at 4 K. The *CW*- and *ACW*-domains have opposite

chiral induction effects on the guest molecules, resulting in different enantioselectivity (Figure 4.6b). Importantly, the chiral induction is present even at RT, although the exact rotation angle of the guest has broader distribution between 0º and ±15º, respectively (Figure 4.5c).

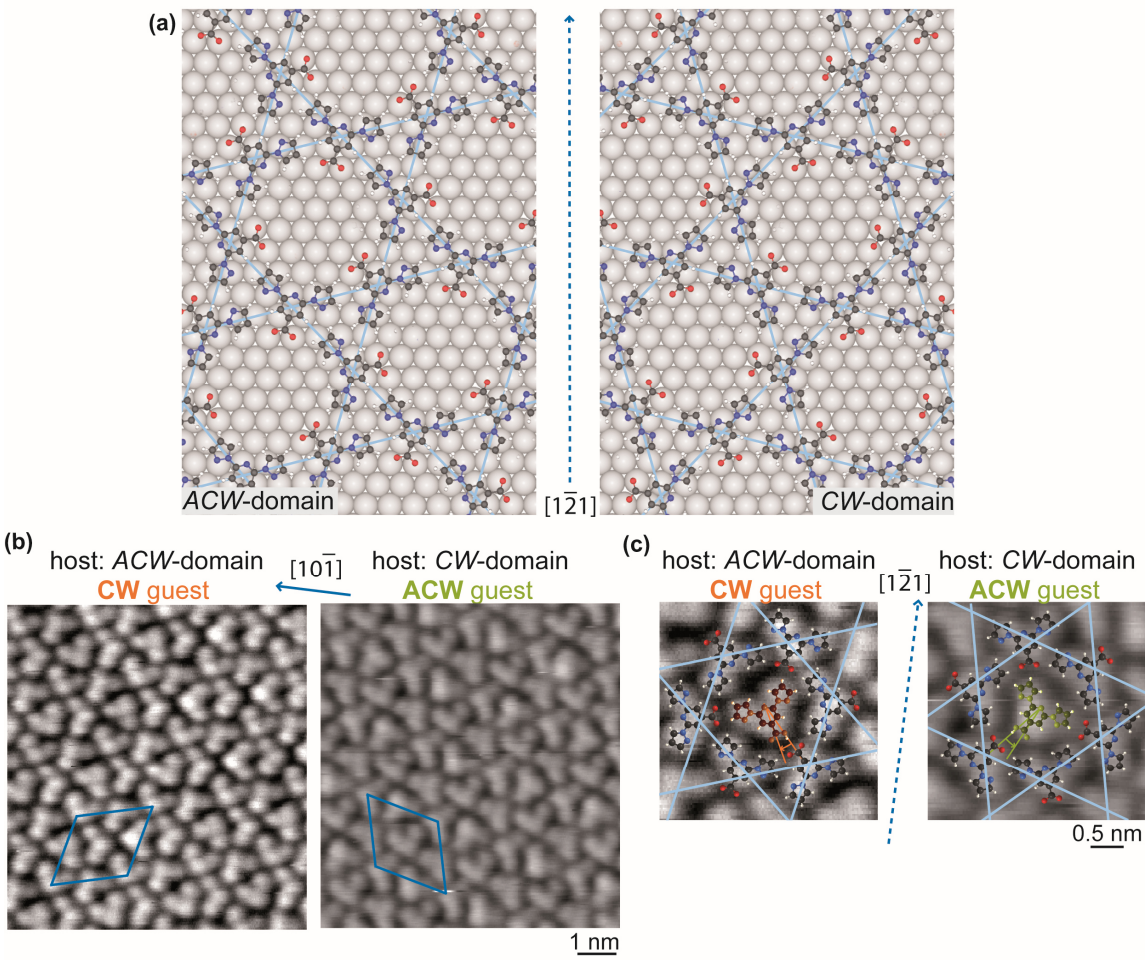

Figure 4.6: (a) *ACW*-domains (left) and *CW*-domains (right) form as a result of the mirror symmetry along the Ag [1$\bar{2}$1] direction (dotted line). (b) overviews and (c) magnification STM images of the *ACW*- (left: -625 mV, 40 pA) and *CW*- (right: 1500 mV, 100 pA) kagome domain of the host-guest network imaged at RT. The [10$\bar{1}$] and [1$\bar{2}$1] directions of the Ag(111) are indicated, respectively. The *CW*- and *ACW*-domains result in enantiomeric separation of the guest molecules. The host is represented with C, N, O, H and Ag atoms in black, blue, red, white and grey, respectively. The guest molecule is colored differently, depending on its surface chirality. Adapted from [104].

To verify the origin of this chiral induction, we investigated the effect of the Ag(111) substrate. DFT energy optimization of the supramolecular structure in the absence of the Ag substrate shows the **CW**- and **ACW**-bpp-COOH guest orientations are energetically degenerate, both have a minimum at 0°; and in addition, reflection planes at 0° and 60° transform the energy landscape of the **CW** into that of the **ACW** (Figure 4.7a). Similarly, on the bare achiral Ag(111) surface with no kagome network present, the rotational energy landscapes of the **CW** and **ACW** have energetically degenerate minima; these however occur

at different orientation angles for the two surface enantiomers and away from 0° (Figure 4.7b). Accordingly, the reflection planes now occur at different angles. This means that the degeneracy of the minima of the **CW** and **ACW** enantiomers is broken when one adds the effect of both the substrate and the kagome network (Figure 4.7a,b). Consequently, it can be inferred that it is the non-zero twist angle between the kagome network and the Ag(111) which breaks the symmetry between **CW** and **ACW** and is thus responsible for the guest chiral induction.

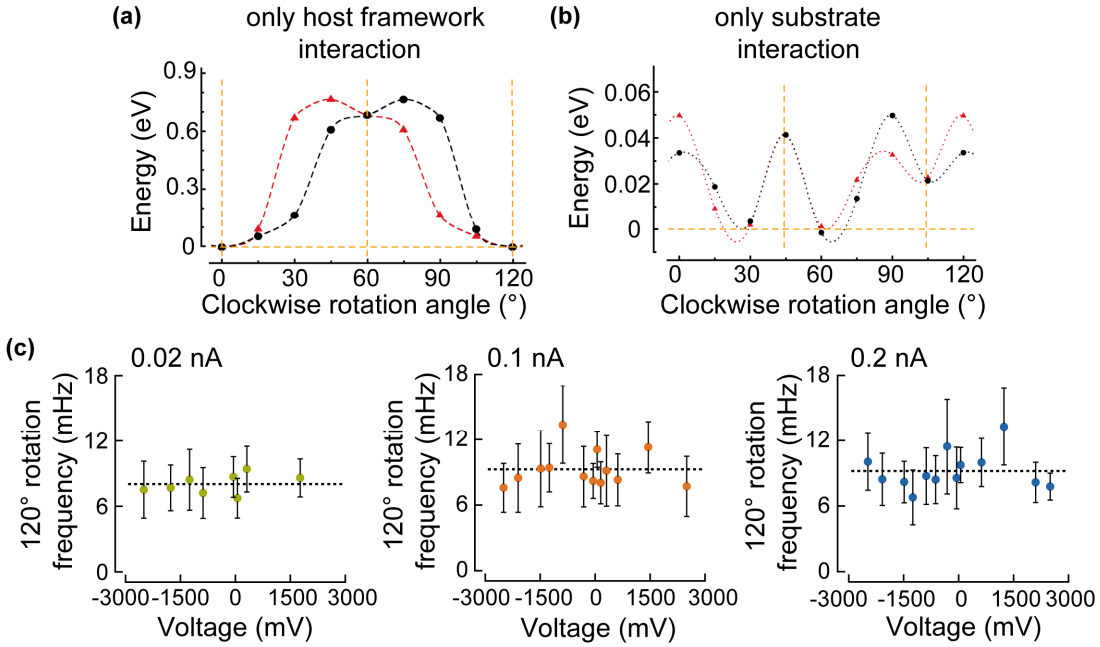

Figure 4.7: (a) The rotation energy of the **CW**-(black) and **ACW**-(red) guest in the kagome network without the presence of Ag(111). (b) The rotation energy landscape of the **CW**-(black) and **ACW**-(red) guest on Ag(111) in the absence of the kagome network. The rotation energy of the two enantiomers has minima and reflection planes (indicated by dashed vertical lines) at different rotation angles from that in (a), thus, adding the curves of the respective enantiomer from (a) and (b) will break the degeneracy between the two enantiomers. (c) The detected rotation frequency showed no dependence in the tunneling current range of 0.02 to 0.20 nA and in the tunneling bias range of -3000 to 3000 mV. Adapted from [104].

The most frequently observed orientation of guest to host molecule matches well with the DFT optimized guest geometry. Having observed the switching of the position of the molecule in consecutive STM images at RT (Figure 4.1c), we considered this a model system for a confined rotation controlled by H-bonds. To better understand the dynamics of this system, we performed a dual experimental and theoretical investigation.

We acquired systematically time resolved STM data of the switching events as a function of the temperature, tunneling bias and tunneling current. No correlation of the rotations and positions of the neighboring caged guests was noticed, we therefore considered them as independent rotors. For obtaining comparable rotation frequencies for the parameters, the total

number of observed rotation events was divided by the total number of rotors and the acquisition time. We find that the range of tunneling conditions employed here does not influence the switching events, so we can use STM to follow the natural thermally activated rotation of the guest molecules within the nanopore (Figure 4.7c). It should be noted that our investigations do not exclude the possibility of tip induced activated rotation under different tunneling conditions. We recorded the frequency of rotation events by 120° as a function of temperature (Figure 4.8a). Each obtained data point is based on at least 10 consecutive STM image with approximately 25 independent rotors (7x7 nm^2) and an acquisition time of 10 s. With an Arrhenius equation fitting, the barrier is determined to be 0.95 eV ± 0.07 eV with a corresponding pre-exponential factor of ~ $2.3 \cdot 10^{14\pm1}$ s^{-1}.

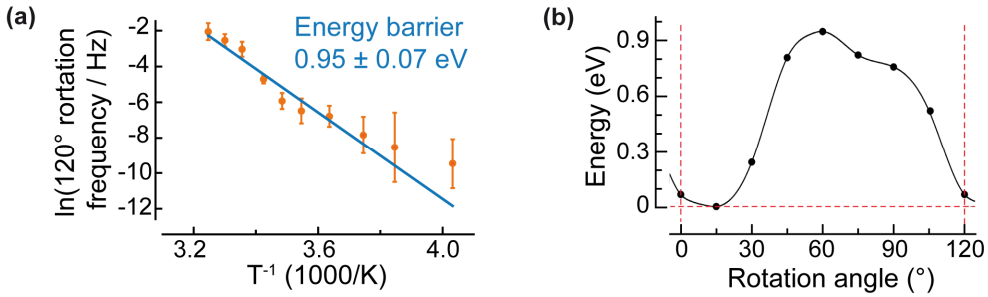

Figure 4.8: (a) Arrhenius plot of rotation frequency determined by STM data in order to deduce the energy barrier. (b) DFT derived energy relative to the optimized geometry (guest at 15º) in the path leading to a guest rotation of 120° for **CW**-guest in an *ACW*-domain. The rotation angle represents the clockwise offset from the head-to-head orientation. Adapted from [104].

Our theoretical investigations provided a more detailed understanding of this process. In excellent agreement with the experimentally deduced value, a rotational barrier of 0.94 eV is computed (Figure 4.8a,b). The main contribution to this barrier is the lateral bonding of the rotating guest to the kagome network pore by 0.77 eV (Figure 4.7a,b). We identify different intermolecular H-bonds in the charge redistribution maps corresponding to the charge density difference of the separate molecular constituents and the Ag substrate from the adsorbed host-guest system (Figure 4.9a). The signature of an attractive interaction is a line of alternating yellow and green lobes, which represent isosurfaces of the same value of electron accumulation and depletion, respectively [169-170]. Five strong hydrogen bonds can be identified in the second most frequently observed geometry (Figure 4.9a, 0°), where the kagome structure maximizes its interaction with the guest molecule. At the global energy minimum, 0.07 eV lower in energy than the head-to-head orientation, where the interaction of the guest molecule and the substrate is also optimized, three stronger and two weaker hydrogen bonds form (Figure 4.9a, 15º). As mentioned above, the twist angle between Ag(111) and the kagome network is responsible for this energy minimum. The energy maximum is found where the guest does not have significant bonding with the host (Figure 4.9a, 60º).

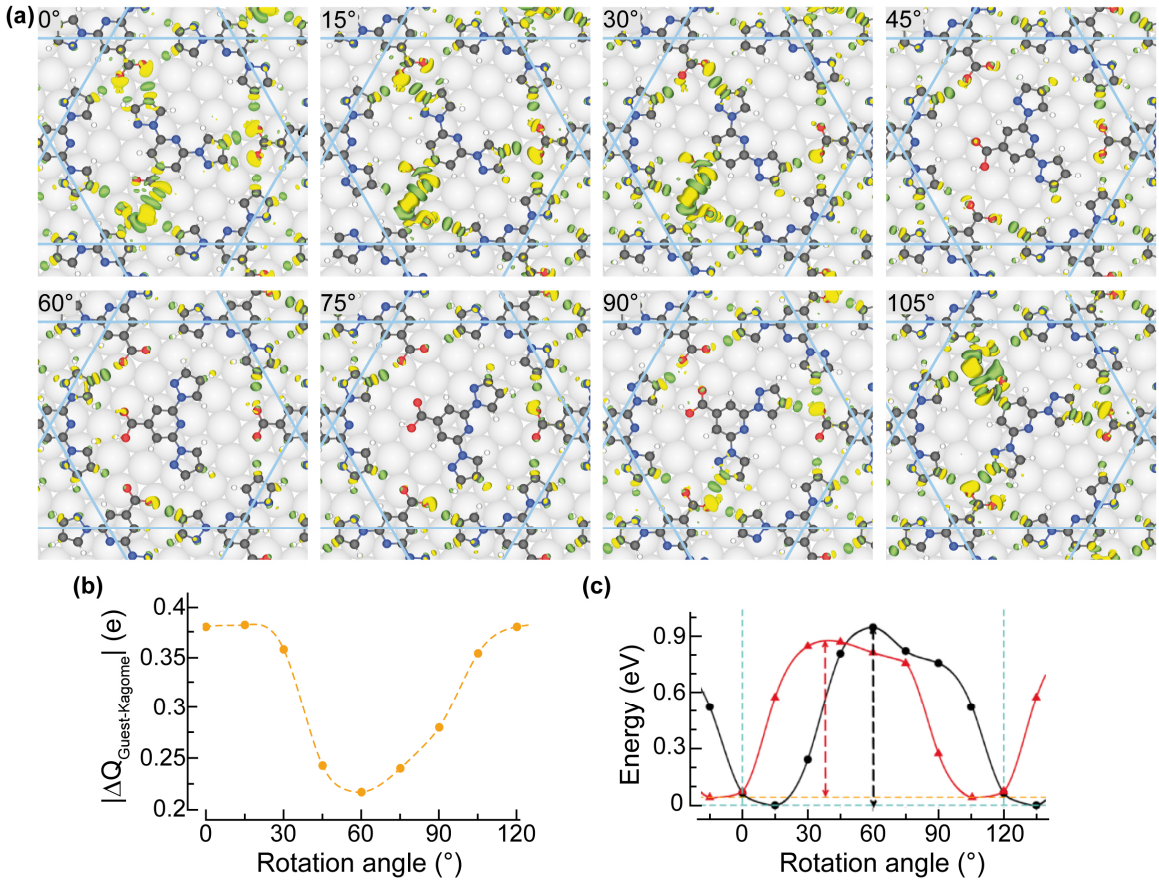

Figure 4.9: Optimized geometries and superposed differential charge distribution at different rotation angles of the guest. C, N, O, H, and Ag atoms are shown in black, blue, red, white and grey, respectively. Yellow and green lobes indicate electron accumulation and electron depletion, respectively, with isosurface values of $1.2 \cdot 10^{-3}$ e bohr^{-3}. (b) Charge transfer between the guest molecules and the kagome network *vs.* the guest's rotation angle. (c) Energy landscapes computed from DFT for the rotation of **CW**-(black) and **ACW**-(red) guest in an *ACW*-domain of the kagome network on Ag(111). Adapted from [104].

We also show that the charge transfer between the guest molecule and the host, comprising the kagome network and the Ag surface, correlates well with the height of the rotational barrier. The charge transfer is greatest at the minimum of the rotational energy landscape, and least for the most unfavorable guest orientation at 60° (Figure 4.9b). Comparison with the confinement of an **ACW**-bpp-COOH guest in an *ACW*-domain of the kagome network and its rotation (Figure 4.9c) further supports the observation of chiral induction.

Interestingly, by scrutinizing the optimized DFT geometries, the adaptability of the host with respect to the guest dynamic position in the optimized geometries becomes evident (Figure 4.9a). Displacements of 0.78 Å can be detected for the center of the pyridine ring, in line with dynamic porous features of responsive coordination polymers [171]. As a footnote, we also noticed a statistically insignificant number (less than 1%) of guests rotating too fast to be monitored with our scanning speed in our experimental data. We tentatively attribute these to

potential bpp-COO^- guests. Consideration of bpp-COO^- guests by DFT found indeed a significantly reduced barrier of 0.11 eV for rotation of such guest molecules. However, overall the bpp-COOH guest is significantly favored by 0.81 eV per unit cell (see Appendix, Figure A.3), further reinforcing our interpretation.

Conclusion

We reported on the spontaneous self-assembly of bpp-COO^- molecules on a well-defined surface into a stable kagome network filled with bpp-COOH guests in its pores. The registry of the kagome network on the Ag(111) substrate induces enantioselective organization of the guest molecule inside the pores of the kagome network. The rotation of the guest molecule inside the pore is controlled by the kagome network: the chemical structure of the pore wall provides flappers that pin the guest molecule and prevent its unhindered rotation. The spontaneous formation of the host-guest assembly reported in this study is a model system for the investigation of delicate, dynamic, and enantiospecific interactions in confined spaces, which could help design enantioselective heterogeneous catalysts. We further anticipate that such ordered large-scale networks with embedded individual switching units could be promising components for developing molecular nanodevices.

5 Structural Adaptations of Electrosprayed Aromatic Oligoamide Foldamers

This chapter is based on

Meier, D.; Schoof, B.; Wang. J.; Li, X.; Walz, A.; Huettig, A.; Schlichting, H.; Rosu, F.; Gabelica, V.; Maurizot, V.; Reichert, J.; Papageorgiou, A. C.; Huc, I.; Barth, J. V., Structural adaptations of electrosprayed aromatic oligoamide foldamers on Ag(111). *Chem. Commun.* **2022**, *58*, 8938-8941. Reproduced with permission from the Royal Chemical Society.

Aromatic foldamers adopt particularly stable and predictable conformations and constitute useful molecular platforms for applications in molecular recognition [172-177], transport through bilayer membranes [178-180] or molecular machinery [181-183]. They also feature interesting charge transport properties [106, 108, 184-185]. In the case of Q_n, depicted in Figure 5.1a, helical conformations are extremely stable in solution due to hydrogen bonding (dotted blue lines in Figure 5.1a). Furthermore, an unfolding is also hindered through repulsive interaction between the oxygen atoms of the peptide bonds and the quinolines' nitrogen (grey arrows in Figure 5.1a). An octamer shows, for example, no denaturation at 120 °C in dimethyl sulfoxide [186] and its helix handedness inversion is kinetically locked in water [30]. These helices also show strong resistance to mechanical extension [31]. No experimental conditions have been found to date under which unfolded (extended) or misfolded conformations would be significantly populated. In the course of charge transport studies of these compounds, monolayers of thiol-functionalized helices on gold were produced [108, 184-185]. Despite having the expected thickness for upstanding helices, these monolayers did not show high order, presumably due to limited surface diffusion preventing epitaxial growth. On the other hand, various helical polymers have been found to self-assemble on surfaces, albeit with their helix axes parallel to the surface plane [187-188].

We endeavored to construct 2D-crystalline monolayers of the previously described helical oligoamide foldamers by using ES-CIBD [35-36]. After mass filtering, the extracted ions are soft landed on an Ag(111) surface with controlled energy and dose [189-191]. Ag(111) is relatively inert, densely packed and of low corrugation. Thus, it is a common substrate for the self-assembly of organic molecules. Deposition of pyr-Q_4 foldamers reveals in STM the formation of ordered arrays on an atomically planar Ag(111) surface in a surprising unfolded flat ribbon conformation (Figure 5.1b,c). Pyr-Q_7 was also observed in an unfolded conformation at step edges on Ag(111) with STM. "Unfolding" often refers to a disordered conformation, as

in proteins. In contrast, the unfolded flat ribbons observed here have a well-defined structure. Complementarily, IMS measurements of Q_n foldamers indicate that the ions are helically folded in the gas phase after electrospray ionization. Therefore, the unfolding has to occur during landing of the molecules or on the metal surface.

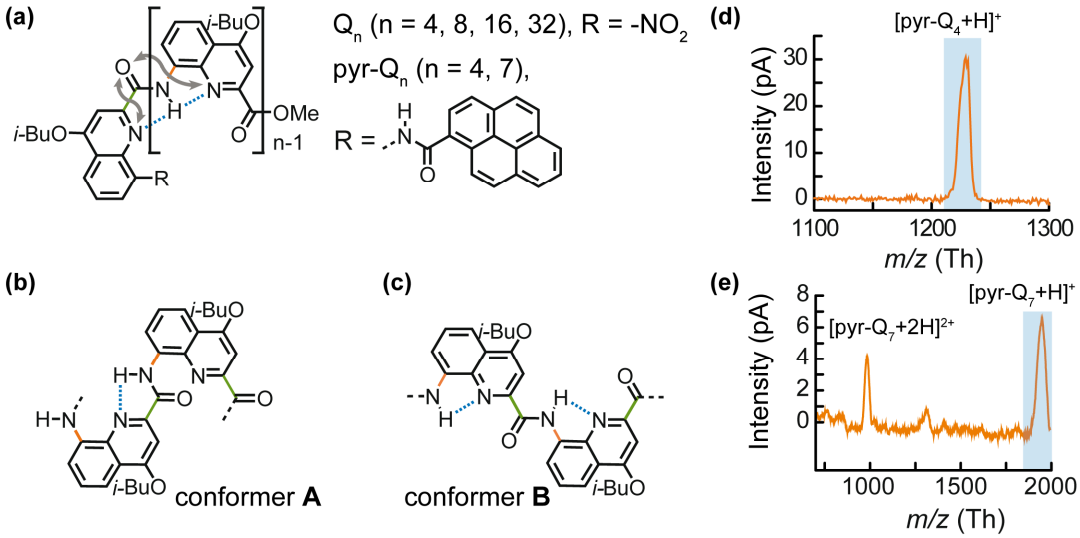

Figure 5.1: (a) Structural formulas of the foldamers Q_n and pyr-Q_n. Blue dotted lines point out hydrogen bonds and grey arrows show electrostatic repulsion. The aryl–NH and aryl–carbonyl bonds are colored orange and green, respectively. Ribbon structures of unfolded molecule through either (b) rotation of the aryl-NH bonds (orange) or (c) rotation of the aryl–carbonyl bond (green). Mass spectra prior to ES-CIBD of (d) pyr-Q_4 and (e) pyr-Q_7. The deposited *m/z* regions are emphasized with blue badges. Due to a low signal-to-noise ratio in the mass spectrum of pyr-Q_7, a 10-point average fit was applied to the presented spectrum. Adapted from [109].

Results and Discussion

Pyr-Q_4 and pyr-Q_7 (Figure 5.1a) were designed with a pyrene foot expected to provide affinity to the surface yet without hampering mobility, essential for highly ordered self-assemblies. As with the related aromatic foldamers, single crystal data show that pyr-Q_4 has a helical form. The investigation was initialized by recording the mass spectra for the two foldamer species with the dQMF before deposition (Figure 5.1d,e). The mass spectrum of pyr-Q_4 reveals a single peak at approximately 1230 Th, corresponding to $[\text{pyr-Q}_4+\text{H}]^+$, whereas pyr-$Q_7$ exhibits two primary charge states in the mass spectrum: one at 1957 Th ($[\text{pyr-Q}_7+\text{H}]^+$) and another at 979 Th ($[\text{pyr-Q}_7+2\text{H}]^{2+}$). We only deposited the single positively charged ions (blue badges in Figure 5.1d,e). It is proposed that the additional protons of $[\text{pyr-Q}_n+\text{H}]^+$ species will spill over to the silver surface at RT [192-193] and form adsorbed pyr-Q_n and atomic H. The latter recombines to form gaseous H_2 [194].

The STM investigation was started with the deposition of pyr-Q_4 on Ag(111) with a mean landing energy of ~4.5 eV z^{-1} per molecule. This energy was selected as a compromise

between the ion current of the deposited species measured on the sample and its landing energy. The adsorbed pyr-Q_4 was too mobile to image on Ag(111) at RT. However, at 180 K and low coverages (43 nC or $2.7 \cdot 10^{11}$ molecules), molecules at step edges were observed (Appendix B, Figure B.1a). Upon increasing the coverage (> 114 nC or $7.2 \cdot 10^{11}$ molecules), highly-ordered islands were imaged at 170 K with an extend over 60 nm^2 (Figure 5.2a and Appendix B, Figure B.1b). The unit cell contains two molecules rotated by 180° and is described by the epitaxial matrix $\begin{pmatrix} 11 & 3 \\ 7 & 14 \end{pmatrix}$ (marked in blue in Figure 5.2a). This corresponds to a submonolayer concentration of 0.21 molecules per nm^2.

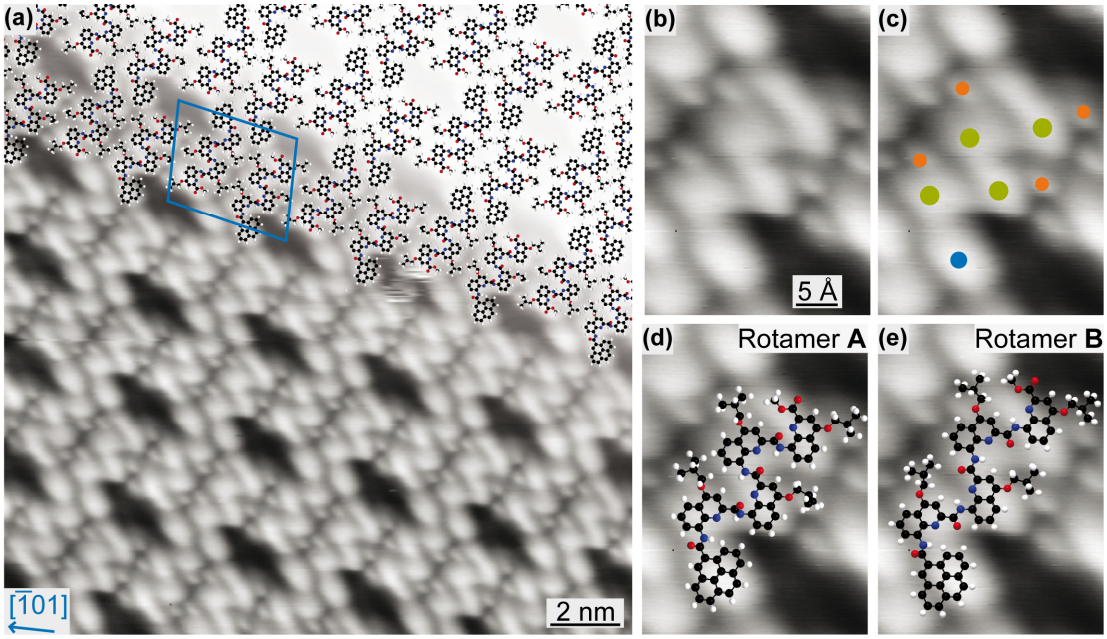

Figure 5.2: STM images of pyr-Q_4 on Ag(111). (a) Overview image (1500 mV, 100 pA, 170 K) partially overlaid with molecules (C in black, N in blue, O in red, and H in white). The unit cell is indicated in blue and a high symmetry direction of the Ag substrate is given by the blue arrow. (b-e) High resolution STM image of a single pyr-Q_4 molecule on Ag(111) (1500 mV, 30 pA, 170 K). In (c), blue, green, and orange dots mark the moieties of a single molecule assigned to pyrene, quinoline, and *i*-BuO, in this order. Rotamer **A** and **B** are overlaid over the STM data in (d) and (e), respectively. Only rotamer **A** fits the STM data. Adapted from [109].

A single molecule is identified by a constellation of five major protrusions (see blue and green dots in Figure 5.2b) forming a zig-zag like structure and four small protrusions (orange dots in Figure 5.2b) at the side. The latter can be associated with the *iso*-butoxy (*i*-BuO) side groups at the quinoline core. Therefore, the protrusions marked green can be attributed to the quinoline units. Notably, the terminal related protrusion is larger, presumably due to the methyl ester end group at the quinoline. The protrusion marked blue can be assigned to the pyrene foot. Hence, the molecules appear adsorbed in an intact, unfolded yet organized, flat ribbon state on the Ag(111) surface. It is noted that the moieties capable of forming hydrogen bonds

are too distanced (> 4 Å) between neighboring molecules. Instead, intermolecular attractive van der Waals interactions between the *i*-BuO side groups seem to play a significant role in the self-assembly. Extended aromatic oligoamide ribbons were hitherto reported to form solely under a stretching force [31]. Nevertheless, less stable polyacetylene helices have also been shown to unfold into ribbons on graphite [195]. In fact, the conformational flexibility and unfolding of ribbons on surfaces may control their self-assembly, as exemplified recently by diene surface folding in open chains and shape-persistent macrocycles [196].

Planar, ribbon conformation can be rationalized by rotations of the aryl-amine bonds (orange in Figure 5.1b) and/or of the aryl-carbonyl bonds (green in Figure 5.1c) between the quinolines, elucidating the observed flat conformation of the adsorbed molecules. Due to the regularity of the structure, we assumed that the same rotation takes place between every quinoline unit. With these considerations, we examined two conformations of the extended foldamer: one involving only rotations of all aryl-amine bonds (rotamer **A**) and the other involving only rotations of all aryl-carbonyl bonds (rotamer **B**). The former corresponds to a shorter, ribbon-like structure, while the latter yields a more stretched conformation. The geometries of these rotamers on the Ag(111) surface were optimized by molecular mechanics (see Appendix, Figure B.2). Upon comparing these rotamers with high-resolution STM data, it becomes evident that only rotamer **A** aligns closely with the STM image (Figure 5.2d,e). This is somewhat surprising, considering the pronounced repulsion between iminic N and the carbonyl in rotamer **A** (Figure 5.1c), which, in principle, is even less favored than rotamer **B**. Quantum mechanical calculations of model arylamide compounds report a 0.31 eV higher rotational barrier [197]. It is conceivable that this repulsion is partially compensated by the H^+ from the deposited species, as protonation promotes unfolding in related oligomers [198]. Alternatively, electrostatic repulsions may be screened by the image charges in the metal surface [199].

For comparison, the single positively charged [pyr-Q_7+H]$^+$ was deposited by similar spraying parameters and landing energy per charge (4.5 eV z^{-1}). At 160 K, the molecules were found immobilized exclusively at the step edges of the Ag(111) surface (Figure 5.3a). Individual molecules are identified by eight prominent protrusions marked with green and blue dots in Figure 5.3b. Additionally, seven smaller protrusions marked in orange are positioned adjacent to the moieties highlighted in green This aligns with the STM imaging of the extended pyr-Q_4, which displays five major protrusions and four smaller ones (compare Figure 5.2c and Figure 5.3b). Consequently, the protrusions are assigned to the pyrene (blue dots), quinolines (green dots) and *i*-BuO groups (orange dots) (Figure 5.3b), thus indicating an unfolded ribbon conformation for pyr-Q_7 as well. Similar considerations for the unfolding of pyr-Q_7 as those for pyr-Q_4 were taken into account, resulting in the corresponding compact and extended rotamers

A' and **B'** for pyr-Q_7. When overlaying the two optimized molecular structures obtained by molecular mechanics (see Appendix, Figure B.3) onto the STM image, it is evident that rotamer **B'** aligns better with the STM image compared to rotamer **A'** (Figure 5.3c,d), in contrast to the observed occurrence of rotamer **A** for the smaller pyr-Q_4 molecules (Figure 5.2d). Hence, it is inferred that unfolding takes place regardless of the length of the foldamer, leading to the expression of different stereoisomers on the surface, likely contingent upon the surface adsorption site (terrace vs. step edge). The presence of rotamer **A'** on the Ag(111) surface cannot be excluded and might emerge by immobilizing diffusing adsorbates at lower temperatures or of samples with higher molecular coverages. Hence, additional investigations at higher coverages are expected to unveil whether self-assembled pyr-Q_7 islands form, akin to the observation with pyr-Q_4.

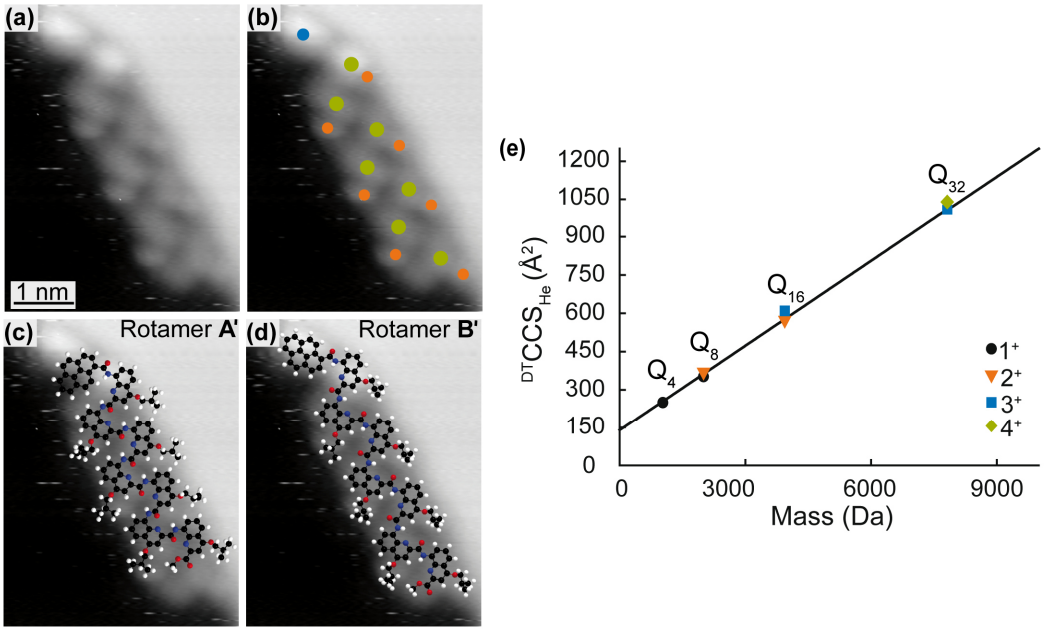

Figure 5.3: (a) STM image (-1250 mV, 80 pA, 160 K) of pyr-Q_7 on a step edge of Ag(111) (b) pyrene, quinoline, and *i*-BuO groups are marked on the STM image in blue, green and orange, respectively. STM image overlaid with (c) rotamer **A'** obtained through rotation of all aryl–NH bonds and (d) rotamer **B'** obtained through rotation of all the aryl–carbonyl bonds. (e) Evolution of the collisional cross section ($^{DT}CCS_{He}$) as a function of the Q_n mass. The linear regression (R^2 = 0.99) indicates a perfectly cylindrical shape. Adapted from [109].

Following this analysis, the question arises as to whether the unfolding occurs during the spraying or upon adsorption. In solution, the helices of Q_n oligomers remain folded in acids as strong as pure trifluoroacetic acid. To investigate the potential destabilizing effect of the ionizing H^+ on the helix structure, IMS measurements were carried out on a series of Q_n helical molecules (without pyrene platform) with n ranging from 4 (less than two helix turns) to 32 (almost 13 helix turns). These experiments allow one to estimate the size of ions in the gas phase after electrospray ionization. Figure 5.3e shows a linear relation between the collisional

cross section ($^{DT}CCS_{He}$) of the different Q_n molecules and their mass. Calculated $^{DT}CCS_{He}$ values based on theoretically optimized structures are in agreement with the experimental data (see Appendix, Figure B.4) [109]. The linear evolution of the $^{DT}CCS_{He}$ with the size of the foldamer indicates a perfectly cylindrical (i.e. compact helical) shape and therefore a conservation of the foldamers' compact helical conformation in the gas phase. Notably, no changes of the $^{DT}CCS_{He}$ are found with increasing charge states up to 4^+ for Q_{32}. Thus, Q_n molecules with higher charge state are also in a helical structure during electrospray ionization.

Moreover, the charge states of the pyr-Q_4 and pyr-Q_7 ions within the presented experiments provide additional evidence supporting a helical structure in the gas phase. The *Rayleigh* limit provides the maximum charge carried by a droplet [60]. As electrospray ions originate from such charged droplets, *Rayleigh* limit also gives valuable information on the conformation of ions based on their charge states. Its charge depends on the apparent surface, which is determined by the molecule's geometry. The surface tension of a solution of acetonitrile (69 vol%) and methanol (29 vol%) can be estimated as $\gamma \sim 25$ mN m^{-1} [200]. Further, assuming a density of $\rho \sim 1.22$ g cm^{-3} as in the single crystal [109], we can approximate the sizes of the foldamers. In the helical form, pyr-Q_4 and pyr-Q_7 have aspect ratios close to unity and may therefore be approximated by spherical droplets of approximately 0.74 nm and 0.86 nm radius. The resulting maximum charges of 1.5 e and 1.9 e coincide with the measured charge states of pyr-Q_4, which exclusively occurs singly charged, and pyr-Q_7, which is preferably singly charged with additional doubly charged species of lower abundance, respectively. For a completely unfolded and stretched molecule having an elongated cylindrical (elliptical) shape, one would expect slightly higher charging due to the larger surface and length and therefore lower *Coulomb* repulsion between the charge carriers.

Based on these calculations and the IMS measurements, it is reasonable to assume that the pyr-Q_n molecules will maintain their helical conformation after electrospray ionization and that the observed unfolding only occurred on the Ag(111) surface. A variety of factors can account for the structural change after landing. These include the high affinity of the aromatic units towards the metal surface, the screening of electrostatic repulsion by the metal surface (which eventually overrides intramolecular forces), deposition at RT, and a kind of "reactive landing" caused by the impinging energy of 4.5 eV z^{-1}, which is considered to be "less soft" [190]. This shall be evaluated in follow-up experiments.

Conclusion

We report on the adsorption of flat extended pyr-Q_4 and pyr-Q_7 molecules on Ag(111) in UHV after deposition *via* ES-CIBD. As both pyr-Q_4 and pyr-Q_7 are mobile at RT, the self-assembly scenario may be extended to other planar surfaces of inert metals, such as gold. Through IMS

measurements, we were able to rule out any influence of electrospray on the conformation of the folded helical molecules. Therefore, upon deposition onto the metal surface, these molecules have to undergo unfolding, implying that either the landing energy of the molecules or their interactions with the substrate initiates the unfolding process. Additional investigations using various substrates, including passivated surfaces, and employing different landing energies could provide a clearer understanding of the separate influences of these two factors. The insight provided by the present study is anticipated to be crucial in controlling the folding of biological and biomimetic molecules when integrated on metallic surfaces.

6 Multiple-Technique Approach for a Comparative Study of Ruthenium Porphyrins on Ag(111)

Metalloporphyrins and their partially hydrogenated equivalents play a pivotal role in nature due to their high occurrence, the stabilization of various metal centers, and showcasing of diverse abilities. Traces of porphyrins date back over 1.1 billion years, as evidenced by their discovery in the fossils of marine black shales [201-202], playing a crucial role in the evolution of life. Their functionalities range from transport of respiratory gases, such as O_2 and CO_2 by hemoglobin (Figure 6.1a), to light harvesting and electron transfer by, e.g., chlorophyll (Figure 6.1b) [203]. Their importance and high occurrence inspired Nobel Prize research by *Richard Martin Willstätter*, awarded in 1915 "for his researches on plant pigments, especially chlorophyll" [204], or by *Hans Fischer*, awarded in 1930 “for his researches into the constitution of haemin and chlorophyll and especially for his synthesis of haemin” [205].

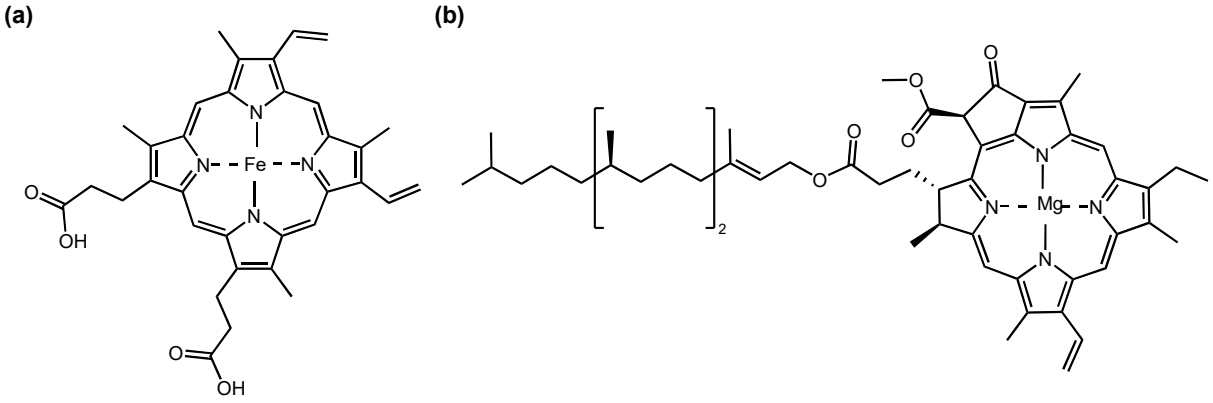

Figure 6.1: Molecular structure of (a) heme B and (b) chlorophyll a.

With the improvement in surface sciences techniques, numerous research efforts were undertaken to functionalize solid surfaces with porphyrins and investigate the properties of the interfaces [38-39]. One notable advantage of these strategies is the capacity of porphyrins to effectively stabilize a diversity of metals in their cavities, p-block as well as f-block elements, providing the flexibility to synthesize architectures with different functionalities [131, 206-207]. The possibility of tuning the magnetic behavior [208-211] or adsorption behavior of small ligand molecules to the metal center [40, 50, 212-214] makes these interfaces of interest for potential applications in spintronics, gas sensing, or heterogeneous catalysis. Not only the metal center can be varied, but also the substrate, which provides further possibilities to influence the physicochemical properties of the resulting porphyrin-based interface [215-217].

Another way to influence porphyrins’ functionalities is by changing their substituents at the macrocycle [218-223]. For example, iron tetrabenzo porphyrin shows an increase in effective

spin moment compared to iron octalethyl porphyrin on Au(111) [221], whereas cobalt octaethyl porphyrin (Co-OEP) has a spin magnetic moment on Cu(100), which is totally quenched for cobalt tetrabenzo porphyrin (Co-TBP) on the same substrate [224]. Another effect of porphyrins' substituents on their functionality is seen in the adsorption of small molecules. While CO adsorbs on the metal center of Ru-TPP on Ag(111), the planarized Ru-TPP counterpart does not exhibit the ability to bind CO at accessible temperatures [223]. Hence, understanding the modifications introduced by different porphyrins' substituents is essential for tailoring the functionalities of metal porphyrin interfaces. On-surface ring-closure reactions are a viable way to change the constitution of the porphyrins and phthalocyanines [111-112, 225]. An example is the electrocyclic ring closure reactions of octaethyl porphyrins and phthalocyanine precursors forming TBPs or phthalocyanines, respectively [111-112]. During the planarization of Ru-TPP molecules, cyclodehydrogenation leads to the formation of 5-membered rings at the periphery of the macrocycle, giving rise to new surface species. The selectivity of this process is dependent on the initial symmetry of the Ru-TPP molecules [83, 225].

Here, we present findings on the impact of substituents and coverage on Ru porphyrins on Ag(111). This study aims to explore how changes in substituents influence both the porphyrin macrocycle and the ruthenium metal center and, additionally, how molecular density can affect the porphyrin macrocycle. To achieve this, we investigated interfaces of Ru-OEP and Ru-TBP on Ag(111) in UHV using multiple techniques such as STM, LEED, XPS, NIXSW, and NEXAFS. These two molecules exhibit variations in the chemical composition of their substituents, with Ru-OEP featuring ethyl side chains and Ru-TBP incorporating phenyl rings attached to the pyrroles of the porphyrin macrocycle. We examined three systems on Ag(111) to address the posed questions. Two distinct self-assemblies of Ru-OEP, a lower coverage phase (submonolayer phase) and a high coverage phase (compressed phase), were observed. For Ru-TBP, only one phase was observed and investigated. These systems are differentiated throughout the chapter using the following color code: submonolayer phase of Ru-OEP (green), compressed phase of Ru-OEP (orange), and Ru-TBP (blue).

Scanning Tunneling Microscopy

The investigation started with the deposition of Ru-OEP on Ag(111). Individual molecules can be recognized in STM, see Figure 6.2a, where a single molecule is outlined in white. It exhibits a central protrusion encircled by four pairs of smaller protrusions appearing with similar apparent heights at a bias of 525 mV. The central feature is assigned to the porphyrin macrocycle, while the eight small protrusions are ascribed to the ethyl side chains [226-228]. Two distinct orientations can be discerned, differentiated by a rotation of 31° ± 2° (Figure 6.2a),

significantly larger than other octaethyl porphyrins on single crystal, low-index metal surfaces (0° to 15°) [226, 228-230]. The axis through two opposite *meso* carbons in both orientations of the Ru-OEP aligns closely with a high symmetry axis of the Ag(111) substrate. Consequently, we attribute the observed higher difference in rotation within the same domain to interaction with the substrate. A well-ordered self-assembly is formed by alternating rows consisting of molecules with only one of the two orientations (Figure 6.2a). Therefore, the surface unit cell contains two molecules. The unit cell was also derived by LEED, which is described by the commensurate epitaxy matrix of $\begin{pmatrix} 8 & -1 \\ 4 & 6 \end{pmatrix}$ marked in Figure 6.2b (see Appendix C, Figure C.1). This unit cell corresponds to a molecular density of 0.53 molecules · nm^{-2}. This packing is observed for surfaces with bare Ag(111) patches and can completely wet the Ag(111) surface.

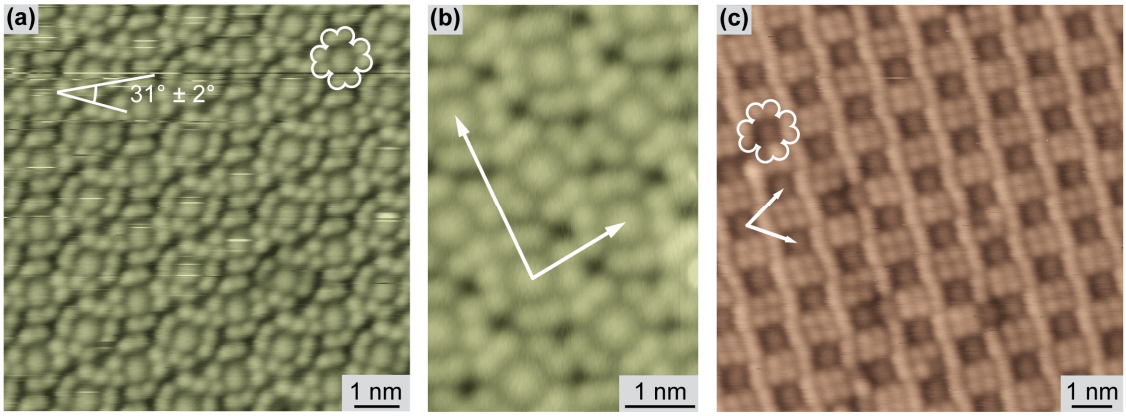

Figure 6.2: STM image of (a,b) submonolayer phase of Ru-OEP (a: 40 pA, 525 mV, 170 K; b: 40 pA, 300 mV, 5 K), and (c) compressed phase of Ru-OEP (20 pA, 312.5 mV, RT). The derived LEED unit cell vectors are marked in white in the corresponding STM image. A single molecule is outlined in white for each self-assembly. In (a), an exemplary determination of the rotation of two adjacent porphyrins is shown.

By increasing the coverage of Ru-OEP to a saturated monolayer, a more compressed phase was achieved (Figure 6.2c). The occurrence of a separate, high coverage phase was also described for Ru-TPP on Ag(111) [231]. The apparent height of Ru-OEP is strongly bias dependent. The same appearance as described for the submonolayer phase is observable. However, at a bias of 1250 mV we see the ethyl chains brighter compared to the central porphyrin ring (Figure 6.2c). A similar contrast change is noticeable for negative biases (see Appendix C, Figure C.4). Notably, no rotation of the adjacent porphyrins in the compressed phase could be observed, making the unit cell consist of one molecule with an epitaxy matrix of $\begin{pmatrix} 4.75 & 0 \\ 4.5 & 5 \end{pmatrix}$, also derived by LEED (see Appendix C, Figure C.2). The epitaxy excludes a single adsorption site. The density is increased compared to the submonolayer phase to 0.58 molecules · nm^{-2}. However, the molecules show the same orientation with respect to the high symmetry axis as in the submonolayer phase.

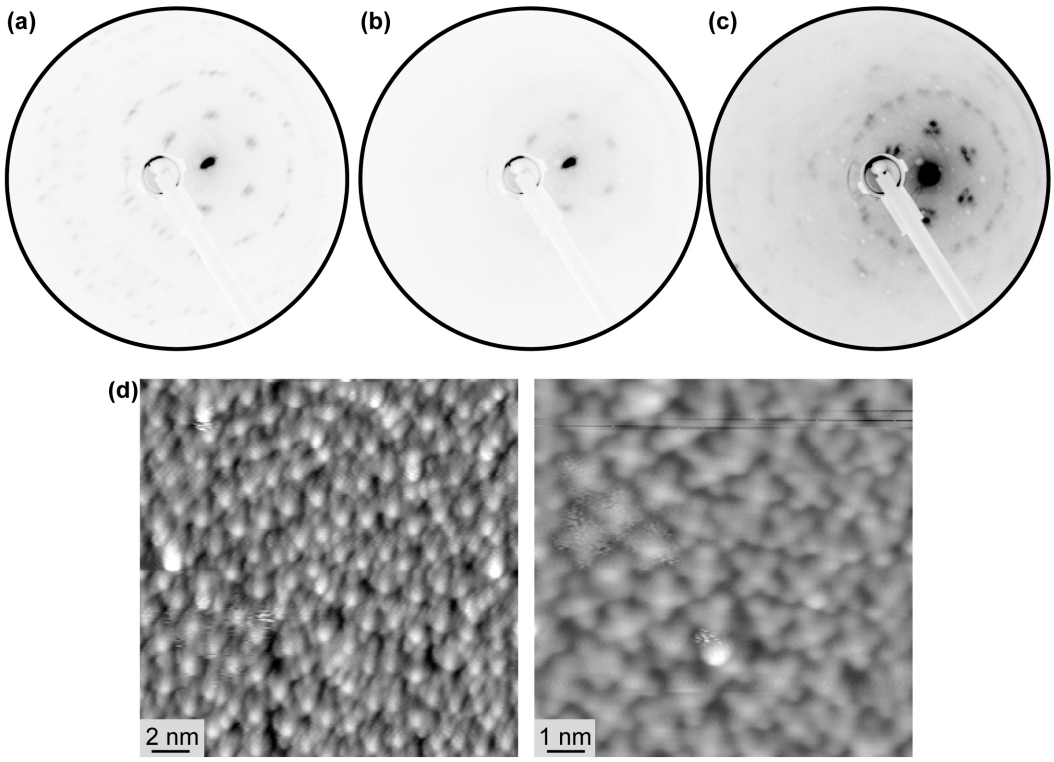

Figure 6.3: LEED of (a) compressed phase of Ru-OEP, (b) after annealing to 600 K, and (c) Ru-TBP prepared on a sample at 700 K. All LEED patterns were taken with an electron energy of 30 eV at the PSD setup. (d) STM images of a monolayer of Ru-OEP annealed to 493 K (left: -1768 mV, 80 pA, RT; right: 1768 mV, 110 pA, RT).

As another presumably flat ruthenium porphyrin, Ru-TBP was selected to investigate the impact of substituents on the Ru center within the macrocycle. Ring closure reaction are reported for octaethyl porphyrins, leading to the formation of Ru-TBP. However, heating the compressed phase of Ru-OEP to temperatures above 600 K resulted in no well-ordered arrangement on the substrate (Figure 6.3a-c). The selectivity for intramolecular over intermolecular reactions of the ethyl side chains is low, hence multiple intermolecular reaction products are observed (Figure 6.3d). To prevent this, Ru-OEP was deposited on a surface at 700 K. At a low coverage, individual molecules were discerned in STM (Figure 6.4a). Nearly no connected porphyrin molecules *via* intermolecular reactions were observed. Upon increasing the coverage of Ru-TBP, self-assembled islands are formed (Figure 6.4b). The contrast of a single molecule is highlighted in white on the STM image and is characterized by a central protrusion surrounded by four smaller protrusions on each side. The latter is assigned to the newly formed phenyl rings, comparable to other metallo tetrabenzo porphyrins and phthalocyanines [111-112]. The contrast of Ru-TBP exhibits a bias dependency, with the center more pronounced at lower biases and the phenyl rings dominating at higher biases (see Appendix C, Figure C.5). The epitaxy matrix of $\begin{pmatrix} 4.3 & \text{-}1 \\ 4.6 & 4.9 \end{pmatrix}$ describes approximately the unit cell detected by LEED (see Appendix C, Figure C.3). This yields a molecular density of

0.52 molecules · nm^{-2}. Discrepancies between the LEED derived unit cell and the STM images can be observed (see Appendix C, Figure C.6) and may be attributed to the different acquisition temperatures and, possibly, different layer strain. The LEED data was taken at 200 K, whereas the STM images were recorded at 5 K. Mobility of the Ru-TBP molecules can lead to an averaged position observed in LEED, whereas all mobility is frozen in the STM images, giving rise to the discrepancies in position.

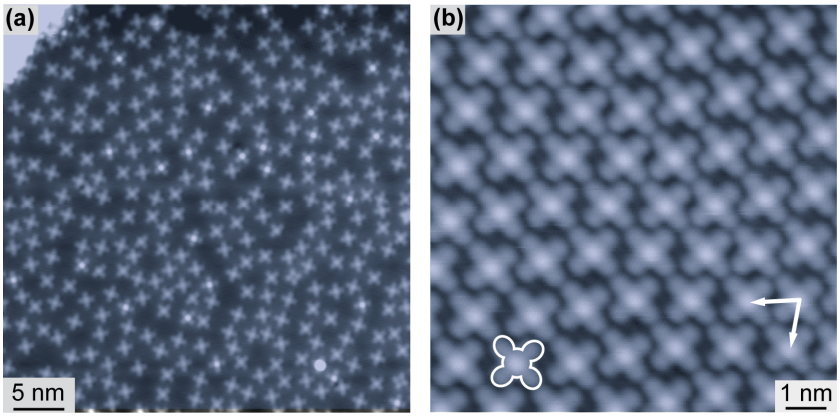

Figure 6.4: STM image of (a) submonolayer coverage of Ru-TBP (50 pA, 200 mV, 5 K) and (b) monolayer of Ru-TBP (50 pA, 200 mV, 5 K) on Ag(111). In (b), the derived LEED unit cell vectors are marked and a single molecule is outlined in white.

X-ray Photoelectron Spectroscopy

The chemical state of the ruthenium porphyrins was analyzed *via* XPS. Analysis of the XP spectra for both the submonolayer and compressed phases of Ru-OEP revealed no apparent differences (Figure 6.5a). Consequently, we focus here on the description of the compressed phase, and assume that the same observations hold true for the submonolayer phase. The Ru $3d_{5/2}$ core level was chosen to assess the oxidation state of the Ru metal center (Figure 6.5b), since the Ru $3d_{3/2}$ peak overlaps with the C 1s peak envelope (Ru 3d spin orbit splitting of 4.2 eV) [76]. The binding energy of the Ru $3d_{5/2}$ peak is 279.2 eV. This value corresponds to metallic ruthenium [232] rather than the expected oxidation state of ruthenium +2 shown in, e.g., a multilayer of Ru porphyrins [231, 233]. This behavior is comparable to other Ru porphyrin species on Ag(111) [231]. The shift can be partially ascribed to final state screening effects of the metal substrate [234-236]. Nonetheless, the binding energy indicates a substantial charge transfer from the substrate to the sample and, thus, a strong chemisorption of the ruthenium porphyrins. Further exploration of this phenomenon will be discussed in subsequent sections.

The XPS of the C 1s core level of Ru-OEP shows a peak at 283.9 eV (green, Figure 6.5c,e). This peak is assigned to the terminal -CH_3 carbons of the side chains [222]. It amounts to 23.7% of the total peak intensity, which fits well with the expected proportion of 22.2% (8 out

of 36 atoms). The three other major peaks in Figure 6.5e are assigned as follows: aliphatic carbons (–CH_2–) of the ethyl side chains (dark blue, 284.5 eV), sp^2-hybridized carbons (bright blue, 284.9 eV), and α-pyrrole carbons with a bond to a nitrogen atom (orange, 285.3 eV). In addition, a weak component has to be attributed to the Ru $3d_{3/2}$ core level (yellow, 283.4 eV) and the higher binding energy peak is assigned to a C 1s shake-up satellite (violet, 285.7 eV).

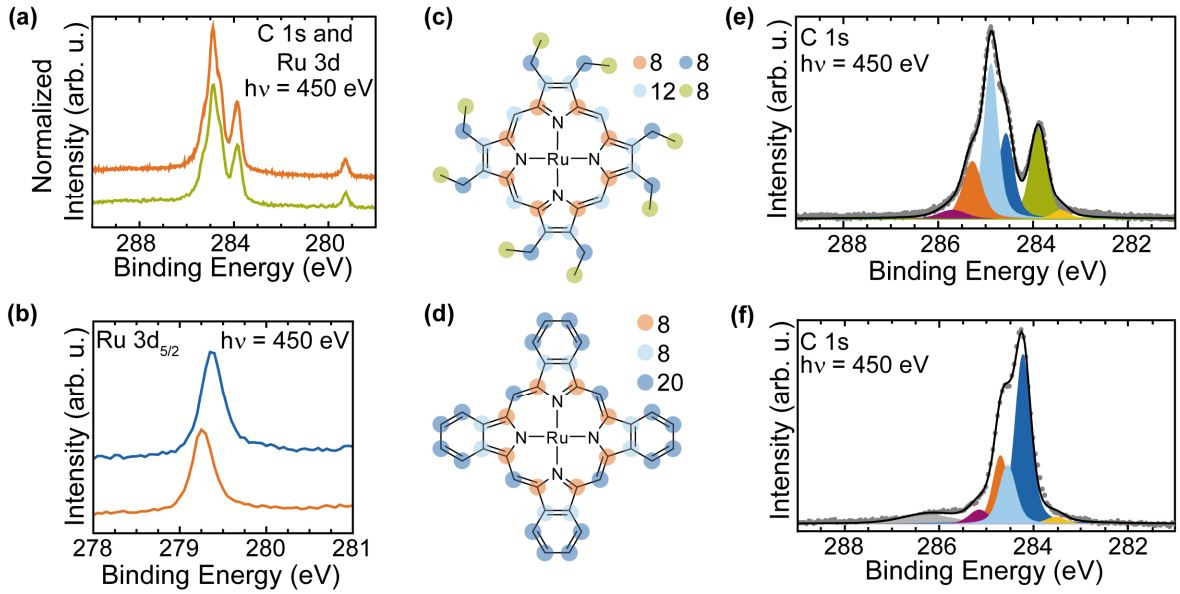

Figure 6.5: (a) Normalized spectra in the C 1s and Ru 3d region of the submonolayer phase (green) and the compressed phase (orange) of Ru-OEP. (b) Ru $3d_{5/2}$ core level of compressed phase Ru-OEP (orange) and Ru-TBP (blue) on Ag(111). Molecular model of (c) Ru-OEP and (d) Ru-TBP. Fitted C 1s XP spectra of (e) compressed phase of Ru-OEP and (f) Ru-TBP on Ag(111). The fitted peaks are colored the same as the corresponding carbons in the respective molecular model; the overlapping Ru $3d_{3/2}$ component is highlighted in yellow.

The XP spectrum of Ru-TBP reveals a similar shift to lower binding energies of the Ru $3d_{5/2}$ peak as observed in Ru-OEP (Figure 6.5b), suggesting similar strong interactions with the substrate. The peak in Ru-TBP is just shifted by 0.1 eV to higher binding energies. However, a strong change in the C 1s core level can be observed. Ru-TBP has a narrower C 1s signal due to the increase in sp^2 hybridized carbons, making the chemical state of all carbon atoms more similar than in Ru-OEP (Figure 6.5d,f). Furthermore, the distinct peak of the ethyl side chains is not observable anymore. This signals the completion of the intramolecular ring closure reactions [222]. Consequentially, the carbon signal was fitted by three distinct peaks, which are attributed to α-pyrrole carbons with a bond to nitrogen (orange, 284.7 eV), sp^2 hybridized carbons with three C–C bonds (bright blue, 284.5 eV) and carbons with two C–C bonds (dark blue, 284.2 eV) (Figure 6.5d,f). A broad peak at binding energy of 286.2 eV is also presented. We assign this feature to a low amount of highly oxidized carbon species, which form during the deposition of Ru-OEP on Ag(111) at 700 K.

Table 6.1: Assignment of the fitted peaks of the C 1s XP spectra of Ru-OEP and Ru-TBP of Figure 6.5 and the respective binding energies. The number of carbons derived by the percentage of the fitted area of a peak and the number of carbons in the corresponding porphyrin are given in columns 3 and 4, respectively.

Component	Binding Energy	#C by fit	#C in molecule
Compressed Phase Ru-OEP on Ag(111)			
–C–N	285.3 eV	6.3	8
sp^2 hybrid. C	284.9 eV	13.0	12
$–CH_2–$	284.6 eV	8.6	8
$–CH_3$	283.9 eV	8.1	8
Ru-TBP on Ag(111)			
–C–N	284.7 eV	19.6	20
sp^2 C with 3 C–C bonds	284.5 eV	7.9	8
sp^2 C with 2 C–C bonds	284.2 eV	8.5	8

Only one peak in the N 1s core level region of both porphyrins is observable due to the chemical equivalence of all four nitrogen atoms in the molecules (Figure 6.6a). However, the peak in Ru-TBP is shifted by 0.3 eV to higher binding energies in comparison to the Ru-OEP peak.

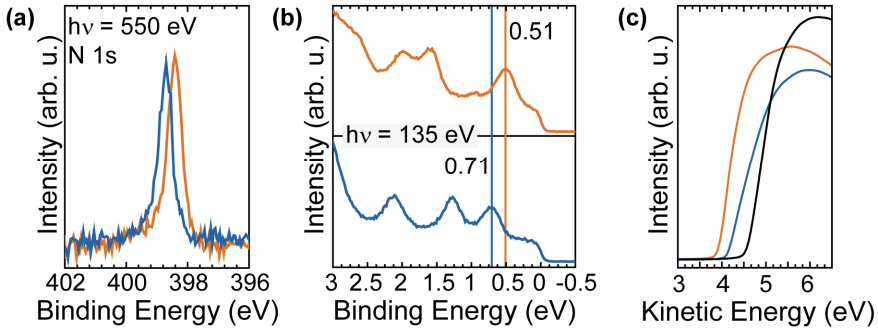

Figure 6.6: (a) XP spectra of the N 1s core level of the compressed phase of Ru-OEP (orange) and Ru-TBP (blue). (b) Valence band of compressed phase Ru-OEP (orange) and Ru-TBP (blue) on Ag(111). (c) XPS secondary electron cutoff measurements of the compressed phase Ru-OEP (orange) and Ru-TBP (blue) functionalized Ag(111) surface and a clean Ag(111) surface (black) used to determine the respective work function changes.

The valence bands of Ru-OEP and Ru-TBP were measured with synchrotron radiation ($h\nu$ = 135 eV), revealing significant differences between the two porphyrin species (Figure 6.6b and Table 6.2). In both molecules, a state near the Fermi edge is observed, indicative of charge transfer from the substrate to the Ru d orbitals, as found before for other metalloporphyrins [235, 237]. This state agrees well with the bright contrast of the porphyrin macrocycle at low negative biases. Though, these two states differ by 0.2 eV. Ru-TPP on Ag(111) shows a similar state at an even lower binding energy of 0.4 eV [223]. Ru-TBP as well as Ru-OEP exhibit two

further states, but these differ in their positions towards each other. Ru-TBP has a state at 1.3 eV and 2.1 eV, whereas Ru-OEP has states at 1.6 eV and 2.0 eV. Surprisingly, quite different valence bands of the two porphyrins were observed, whereas related Co compounds (Co-OEP and Co-TBP) on Ag(110) show only minor differences [222]. The work function change upon adsorption of Ru-OEP and Ru-TBP on Ag(111) was determined by recording the photoemission secondary electron cutoff (Figure 6.6c and Table 6.2). A change of -0.63 eV for Ru-OEP, which is similar to Ru-TPP (-0.67 eV) [42], and of -0.42 eV for Ru-TBP was observed. Thus, we see electronic differences in the interfaces introduced by the change in the porphyrins' substituents.

Table 6.2: Summary of the work function changes, $\Delta\Phi = \Phi(\text{Ru-P/Ag(111)}) - \Phi(\text{Ag(111)})$, by XPS secondary cutoff measurements and of the energetic positions of the HOMO with respect to the Fermi level determined by UPS for the compressed phase of Ru-OEP and Ru-TBP.

Molecules	ΔΦ	HOMO
Ru-OEP	-0.63 eV	-0.51 eV
Ru-TBP	-0.42 eV	-0.71 eV

Near Edge X-ray Absorption Fine Structure

Polarization-dependent N K-edge NEXAFS measurements were conducted to gain insights into the orientation of the porphyrins' molecular moieties relative to the substrate. The spectra from the compressed phase of Ru-OEP exhibit pronounced dichroism in the π^* region (Figure 6.7a). Similar observations were made for the submonolayer phase of Ru-OEP (see Appendix C, Figure C.7). Two distinct resonances are detected at photon energies of 398.9 eV and 401.4 eV, with the maximal intensity observed when the linear X-ray polarization is largely perpendicular to the surface (tilted 30°). Conversely, when the linear X-ray polarization is aligned parallel to the surface, the π^* region is largely suppressed. The C K-edge shows a similar dichroism (Figure 6.7b). As a result, the porphyrin demonstrates a predominantly parallel orientation to the substrate, similar to other octaethyl porphyrins species [214, 222, 238]. A peak at 401.9 eV has the opposite dichroism as the π^* transition. We assign it to a σ^* resonance attributed to a mixed ligand Ru antibonding orbital [222, 239]. For a quantitative estimation of the orientation of the porphyrin macrocycle, polarization-dependent NEXAFS intensities were analyzed. The best fit for the π^* resonance peak at 398.9 eV is shown in Figure 6.7c, and corresponds to a tilt angle of 4.6° ± 5°.

The C and N K-edge NEXAFS spectra of Ru-TBP exhibit a similar strong dichroism in the π^* region as seen for the Ru-OEP (Figure 6.7d,e) and are also reported for other tetrabenzo porphyrin and phthalocyanine molecules [222, 240]. Hence, Ru-TBP is also in a mostly parallel orientation to the substrate. However, unlike Ru-OEP on Ag(111), the N K-edge shows three

π* resonances below 403 eV. An analogous evaluation of the polarization-dependent π* resonance intensities of the peak at 392 eV was conducted (Figure 6.7f) and yielded a tilt angle of 5.2° ± 5°. Therefore, we can infer that both porphyrins are adsorbed in a mostly flat orientation towards the surface.

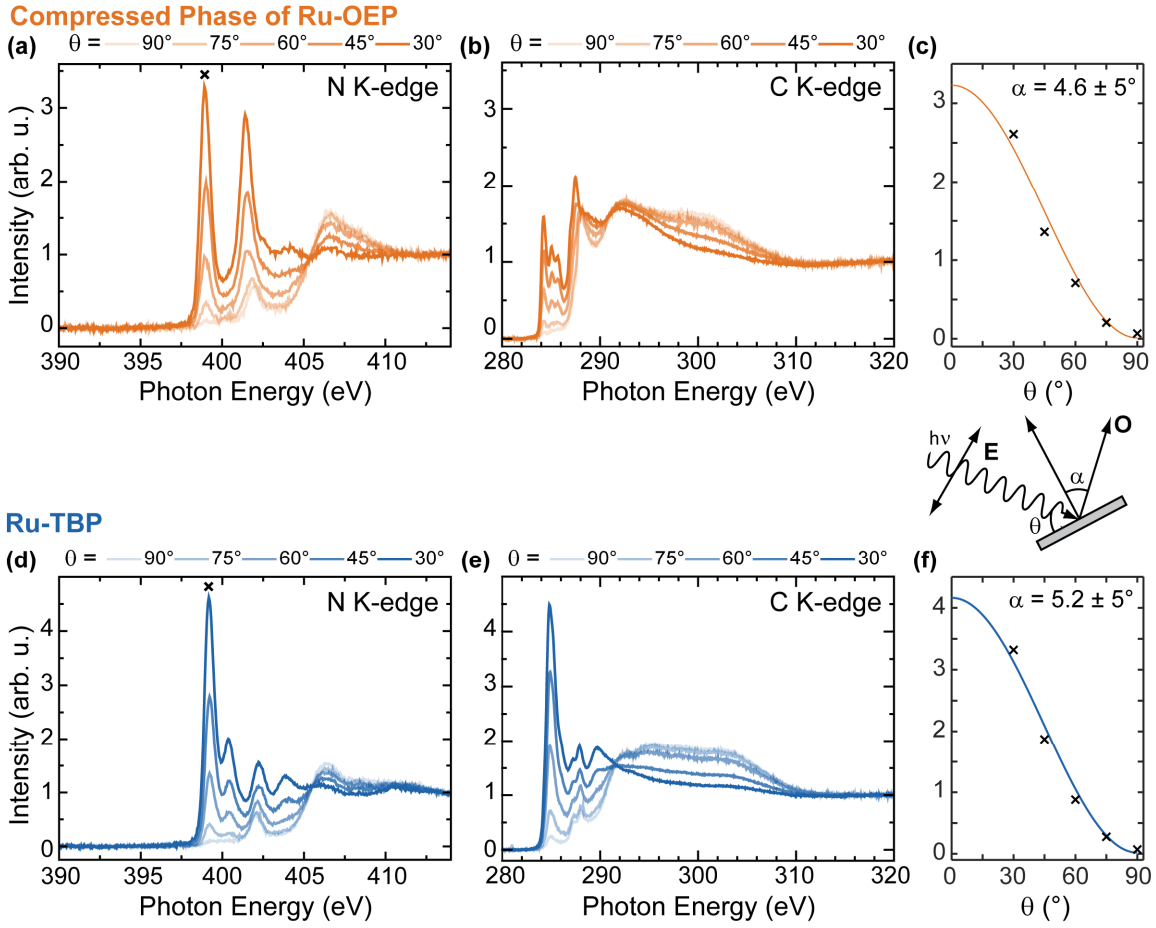

Figure 6.7: (a) N and (b) C K-edge NEXAFS measurements of the compressed phase of Ru-OEP on Ag(111) acquired at five different angles of photon incidence. (c) Curve fitting analysis of the π* resonance indicated by a cross mark in (a). (d) N and (e) C K-edge NEXAFS measurements of the compressed phase of Ru-OEP on Ag(111) acquired at five different angles of photon incidence. (f) Curve fitting analysis of the π* resonance denoted by a cross mark in (d). The inset shows the corresponding angles in (c) and (f).

Normal Incidence X-ray Standing Wave

To improve the understanding of the out-of-plane positions of the atoms, the NIXSW technique at the (111) reflection of the Ag substrate was employed. We measured the NIXSW absorption profiles from the N 1s, C 1s, and Ru 3d core levels. The results are summarized in Figure 6.8 and Table 6.3. The Ru $3d_{5/2}$ profiles are similar between the compressed phase and the submonolayer phase of Ru-OEP, measuring an adsorption height of 2.45 ± 0.09 Å and 2.50 ± 0.09 Å, respectively, with a coherent fraction exceeding 0.8. The proximity to the

surface of the metal center strongly suggests a robust chemisorption. Coherent fractions exceeding 0.75 is typically indicative of a single adsorption height [85] and, therefore, we assume a single adsorption height of the Ru metal centers in both phases. The adsorption heights of the ruthenium matches well with the reported one of planarized Ru-TPP on Ag(111) (2.45 ± 0.02 Å) [231].

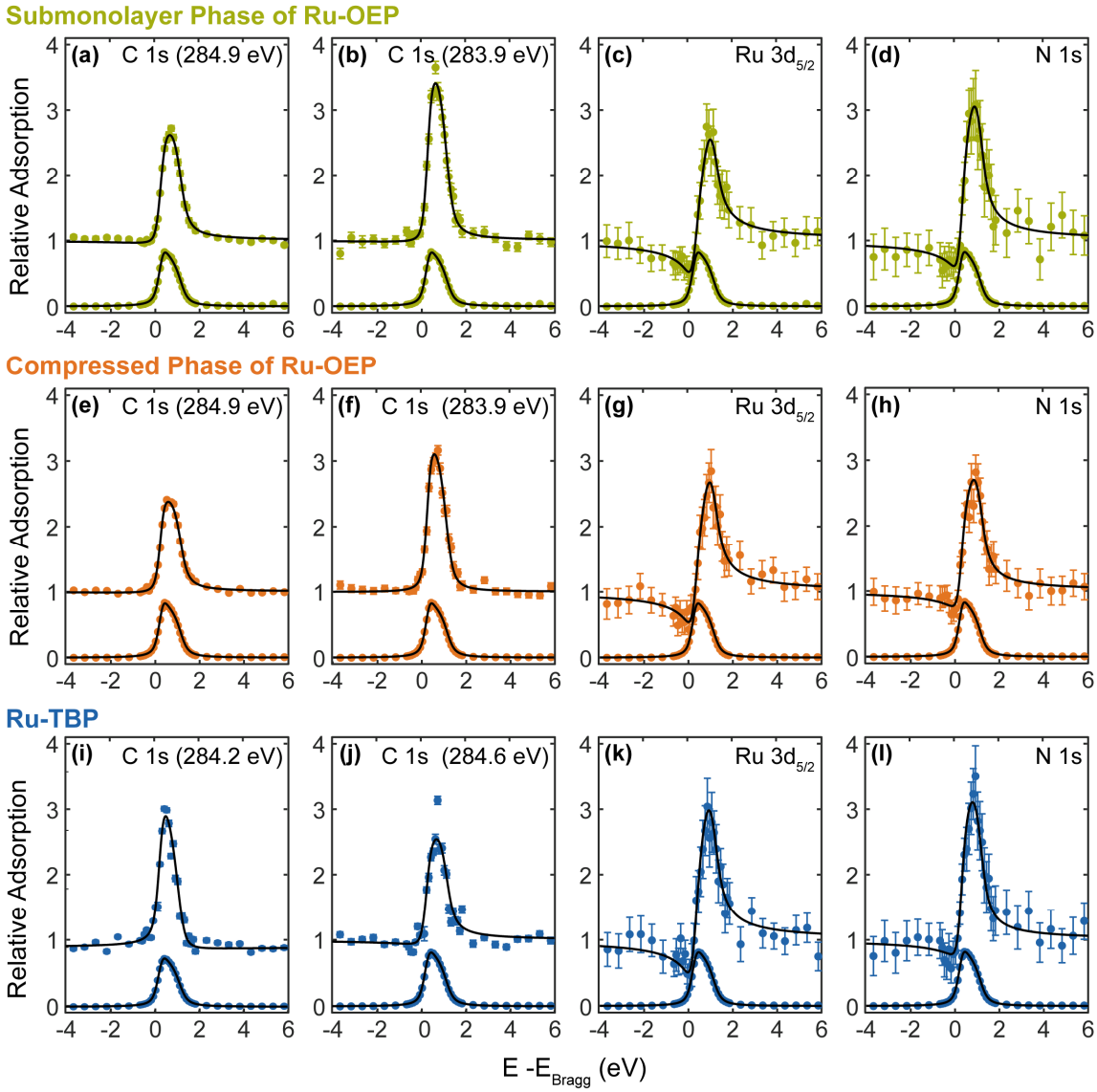

Figure 6.8: (111) NIXSW data of the submonolayer phase ((a)-(d)) and the compressed phase ((e)-(h)) of Ru-OEP and Ru-TBP ((i)-(l)), respectively, on Ag(111). The coherent position and coherent fraction extracted by the fits are summarized in Table 6.3. The assignments of the binding energy of the two C 1s core level peaks are derived from XP spectra labeled in the respective fit.

For the fit of the C 1s core level of the submonolayer and the compressed phase, two peaks were employed – one at 283.9 eV for the methyl end groups and one peak at 284.9 eV for the other carbon species. The peak positions were derived by XPS. The coherent position of the peak at 283.9 eV in the submonolayer phase of Ru-OEP shows a high coherent fraction of 0.8,

which hints to a uniform adsorption height of the side chains [85]. The C 1s core level peak at 284.9 eV has a low coherent fraction of 0.42. Hence, no single adsorption height can be determined, which is expected when fitting different carbon species. The N 1s profile indicates an adsorption height of 2.62 ± 0.12 Å with high coherent fraction (0.89). The higher adsorption height of the methyl side chains compared to the rest of the carbon and the nitrogen atoms is explainable by an upwards orientation of the ethyl side chains. This agrees well with the bias dependent contrast seen in STM, where at high bias the ethyl side chains are far more prominent than the center, supporting higher-lying ethyl side chains to the porphyrin core. Due to the high coherent fraction of the Ru metal center, a random distribution of the carbons can be excluded. However, the low coherent fraction makes it unreasonable to assume a perfectly planar conformation of the macrocycle, even when considering the 8 $–CH_2–$ carbons having a different adsorption height than the carbon atoms of the flat porphyrin macrocycle. Therefore, a distortion of the porphyrin core can be inferred which aligns well with the small tilt angle observed in NEXAFS.

Table 6.3: Summary of the coherent fraction and position derived by NIXSW. The experimental adsorption height was determined with an assumed (111) d spacing of 2.35 Å. Note that the given adsorption heights for species with a coherent fraction below 0.75 cannot be assumed to correspond to a uniform adsorption height.

Component	Binding Energy (eV)	f_{111}	P_{111}	Adsorption height (Å)
Submonolayer phase Ru-OEP				
C 1s	284.9	0.42 ± 0.03	0.19 ± 0.02	2.81 ± 0.05
C 1s	283.9	0.80 ± 0.06	0.24 ± 0.03	5.26 ± 0.07
N 1s	-	0.89 ± 0.13	0.11 ± 0.05	2.62 ± 0.12
Ru $3d_{5/2}$	-	0.81 ± 0.09	0.04 ± 0.04	2.45 ± 0.09
Compressed phase Ru-OEP				
C 1s	284.9	0.25 ± 0.02	0.20 ± 0.02	2.83 ± 0.05
C 1s	283.9	0.61 ± 0.06	0.27 ± 0.03	5.33 ± 0.07
N 1s	-	0.64 ± 0.09	0.11 ± 0.05	2.62 ± 0.12
Ru $3d_{5/2}$	-	0.82 ± 0.09	0.06 ± 0.04	2.50 ± 0.09
Ru-TBP				
C 1s	284.2	0.66 ± 0.09	0.31 ± 0.04	3.08 ± 0.09
C 1s	284.6	0.41 ± 0.11	0.17 ± 0.07	2.75 ± 0.14
N 1s	-	0.80 ± 0.13	0.15 ± 0.06	2.69 ± 0.12
Ru $3d_{5/2}$	-	0.94 ± 0.13	0.09 ± 0.05	2.57 ± 0.12

Different distortions of porphyrins' or phthalocyanines' macrocycles are reported as saddle-shape, bowl-shape, or a vertical offset model [212, 231, 240-241]. The high coherent fraction of nitrogen and the low coherent fraction of the macrocycles' carbon atoms, along with the lower average adsorption height of nitrogen compared to carbon, can be elucidated by a bowl-

like distortion in the porphyrin macrocycle. A saddle shape distortion would contradict the high coherent fraction of the methyl end groups and also their higher adsorption height compared to the macrocycle.

The compressed phase shows a reduction of coherent fraction in the NIXSW of C 1s and N 1s core levels compared to the submonolayer phase. However, porphyrins forming a second layer or different adsorption heights of the carbons can be excluded due to the still high coherent fraction of Ru. Therefore, the loss in coherent fraction has to arise from a stronger distortion in the porphyrin macrocycle and substituents. The methyl groups' peak has a coherent fraction of 0.61, excluding a single adsorption height. Distinct variations are also discernible within the structure in STM, as evident by the contrast difference of ethyl group features with the same orientation towards the scanning direction (Figure 6.2c). This indicates subtle alterations in their respective heights. The reduction of the coherent fraction can also be observed on the other carbon peak and the nitrogen peak. However, the similarity in coherent positions to the submonolayer phase of Ru-OEP indicates a resemblance in the average conformation of Ru-OEP in both phases. A uniform adsorption site, as seen in the submonolayer, is lost in the transition to the compressed phase. This could introduce slight variances in the conformation of the porphyrins. Furthermore, there could be small deviations from the porphyrins' optimal conformation due to the reduction in space through increase in coverage. This explains a reduction of the overall coherent fraction. In conclusion, a transition from the submonolayer to the compressed phase of Ru-OEP has an impact on the porphyrin ring, but the metal center does not appear to be significantly influenced.

Ru-TBP shows a slightly elevated adsorption height compared to Ru-OEP revealed by NIXSW of Ru $3d_{5/2}$. The coherent fraction remains high (Figure 6.8i-l and Table 6.3). Consequently, we attribute a singular adsorption height to the Ru metal center. A two-component fit was employed for the C 1s core level, with one component at 284.2 eV for the carbon with two C–C bonds and another at 284.6 eV for the carbons with N bonds and the carbons with three C–C bonds. The positions of the fitted peaks were determined from the XPS data. The carbon atoms associated with two C–C bonds exhibit a coherent fraction of 0.66, situated at an average height of 3.08 ± 0.09 Å. On the other hand, the remaining carbon species display a lower position and a reduced coherent fraction. It is noteworthy that this peak comprises two distinct carbon species; thus, a lower coherent fraction is anticipated, if the porphyrin's macrocycle has a non-flat conformation. Furthermore, the N 1s profile exhibits a high coherent fraction with a lower coherent position in comparison to the different carbon species. A distortion of the macrocycle has to occur to explain the low coherent fraction of the carbon species and the adsorption height differences between carbon and nitrogen. A tilt of the molecule away from the substrate fails to explain the high coherent fraction of the nitrogen.

Therefore, the observed tilt in NEXAFS must be attributed to internal structural deviation. In a saddle shape conformation, we would expect a lower coherent fraction of the carbon in the phenyl ring, due to two of them are bent upwards and two downwards, which is not observed. We assume, therefore, a bowl shape conformation. This can explain the lower position of the porphyrin macrocycle to the phenyl rings and the high coherent fraction of the phenyl rings. A bowl shape would also fit the observed STM contrast change, in which the prevailing contrast of the center is shifted to the phenyl rings with increasing bias.

Conclusion

We conducted a comprehensive investigation of two distinct porphyrins, Ru-OEP and Ru-TBP, on Ag(111), delving into the impact of coverage and substituents on adsorption geometry and self-assembly. By employing a diverse array of techniques, we elucidated the molecular conformations of Ru-OEP and Ru-TBP, revealing a substantial influence of substituents on the porphyrin macrocycle and the electronic structure. A coverage induced effect phase change induced a distortion in the Ru-OEP conformation, as evidenced by NIXSW measurements. In contrast, no second phase by coverage increase was detectable for Ru-TBP. A notable disparity in the electronic structure of Ru-OEP and Ru-TBP was identified in the valence band and changes in the work function. The observed variations in the properties of the two porphyrins in this study may have implications for various porphyrin functions, such as adsorption. Therefore, further investigations were conducted in the subsequent chapters of this thesis.

7 Investigation of Differences in the Ligation Behavior of Carbene and CO to Ruthenium Porphyrins

To progress from the 2D self-assembly of the porphyrin pedestal to 3D architectures, out-of-plane linker molecules are required. The stability of the intermolecular bonds between these linkers and the porphyrin metal center is crucial for the overall structural integrity. A viable option for linker molecules is the well-established molecular group of N-heterocyclic carbenes, known for their robust binding affinity to various single metal atoms [45-46, 242-244]. Another advantage is the possibility to functionalize these molecules further, allowing for additional opportunities for the 3D architectures' utility [43, 245].

Recently, RT carbene adsorption on a ruthenium porphyrin on a low index, single-crystal, metal surface was reported [41-42]. Specifically, it was shown that Ru-TPP, which are bound almost covalently *via* the Ru atom on Ag(111), are displaced significantly further away from the surface upon IMe adsorption: 1 Å on the Ru atom, whereas a portion of the porphyrin molecules may be ejected from the Ag surface and form a second layer [42]. This reported displacement of the metal center upon ligation exemplifies the structural surface *trans* effect, wherein the NHC and the silver surface act as competing *trans* ligands to the Ru center [38, 50-52]. However, the different behavior of Ru-TPP and planarized Ru-TPP upon CO ligation was highlighted, whereby CO binds to the metal center of Ru-TPP, but does not form a bond with the planarized Ru-TPP at 200 K [223]. Therefore, further investigations of the effect of the porphyrins' substituents on the binding behavior is important to gain insights into the adsorption of potential linker molecules and for the choice of adequate pedestals. A fine control of the molecular reactivity can also affect other fields, notably catalysis, where Ru(NHC)-porphyrins have exhibited interesting activity [246].

We initiated our investigation by conducting desorption experiments involving two out-of-plane ligands, CO and IMe, on the compressed phase of Ru-OEP and Ru-TBP on Ag(111) (Figure 7.1). Both ligands were adsorbed at 200 K. The desorption of the NHC parent ion (*m/z* 96) and CO (*m/z* 30) was monitored by mass spectrometry. Surprisingly, the desorption of CO occurs at a higher temperature on Ru-OEP as on Ru-TBP, whereas when it comes to IMe, its desorption temperature is higher on Ru-TBP compared to Ru-OEP. Intrigued by these preliminary findings, we conducted a multifaceted investigation, employing various techniques such as STM, XPS, NIXSW, NEXAFS and TPD, to delve deeper into the underlying factors

influencing the desorption behaviors of the two ligands. We will commence our analysis by examining adsorption of the carbene, followed by an investigation into CO adsorption.

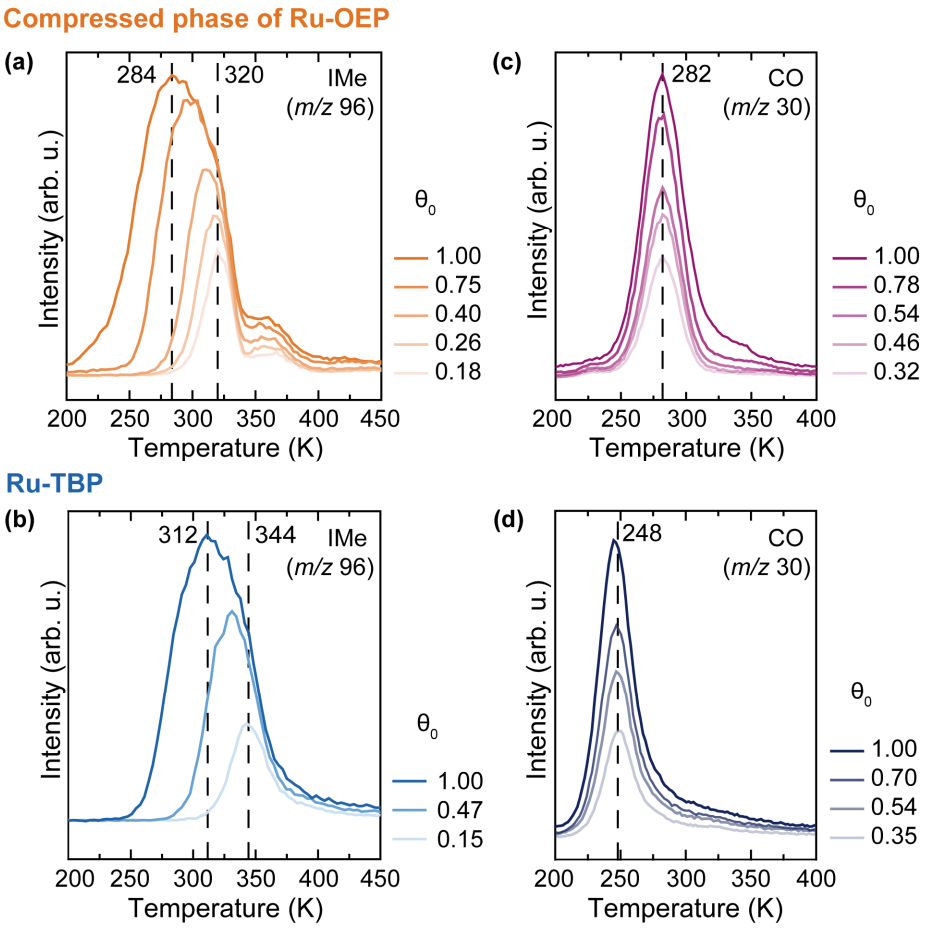

Figure 7.1: Coverage dependent TPD spectra of IMe (*m/z* 96) desorption from (a) the compressed phase of Ru-OEP and (b) Ru-TBP monolayer on Ag(111). Coverage dependent TPD spectra of CO (*m/z* 30) desorption from (c) the compressed phase of Ru-OEP and (d) Ru-TBP monolayer on Ag(111). All adsorptions were performed at 200 K. All spectra were taken with a heating rate of 2 K s^{-1}. The initial coverage of IMe/CO capped Ru centers is noted as θ_0 next to the respective TPD spectra.

IMe adsorption on ruthenium porphyrins on Ag(111)

For both porphyrin metal interfaces, IMe desorption experiments reveal a coverage-dependent shift of the peak maximum towards lower temperatures (Figure 7.1a,b). This shift is attributed to dipole-dipole interactions among the adsorbed carbenes [42, 247]. The occurrence of dipoles upon IMe ligation is further evidenced by the decrease in the work function, with Ru-OEP and Ru-TBP experiencing a reduction of approximately 1 eV (Figure 7.2a). For comparison with the IMe desorption from Ru-TPP on Ag(111) [42], the IMe desorption spectra were fitted by employing a model incorporating a reduction in desorption energy with increasing coverage of the IMe capped porphyrins and a frequency factor of $\nu = 10^{15}$ s^{-1} (Figure 7.2b,c). For Ru-OEP and Ru-TBP, IMe desorption energies of $E_{des} = (1.03 - 0.21 \cdot \theta)$ eV and

E_{des} = (1.09 - 0.19·θ) eV, where θ is the coverage of the IMe capped Ru centers normalized to the initial porphyrin coverage, were obtained, respectively. Therefore, for a complete monolayer of carbene capped porphyrins, the desorption energies are 0.82 eV (Ru-OEP) and 0.90 eV (Ru-TBP), respectively. These energies are, in both cases, lower than the IMe desorption energy of 0.96 eV observed for Ru(IMe)-TPP on Ag(111) [42]. LEED analysis was performed on IMe capped porphyrins and on uncapped porphyrins after IMe TPD (see Appendix D, Figure D.1), revealing no alterations in the LEED pattern. Therefore, a second layer formation, as seen for IMe deposition on Ru-TPP/Ag(111) at RT can be excluded [42]. Consequently, we may assume that IMe ligation does not induce any significant modification in the self-assembly of these Ru porphyrins on Ag(111) at 200 K. The cause of the differences in binding strength for the two porphyrin pedestals will be investigated further to deduce the influence of the porphyrins' substituents and of the initial conformation of the porphyrins' macrocycles.

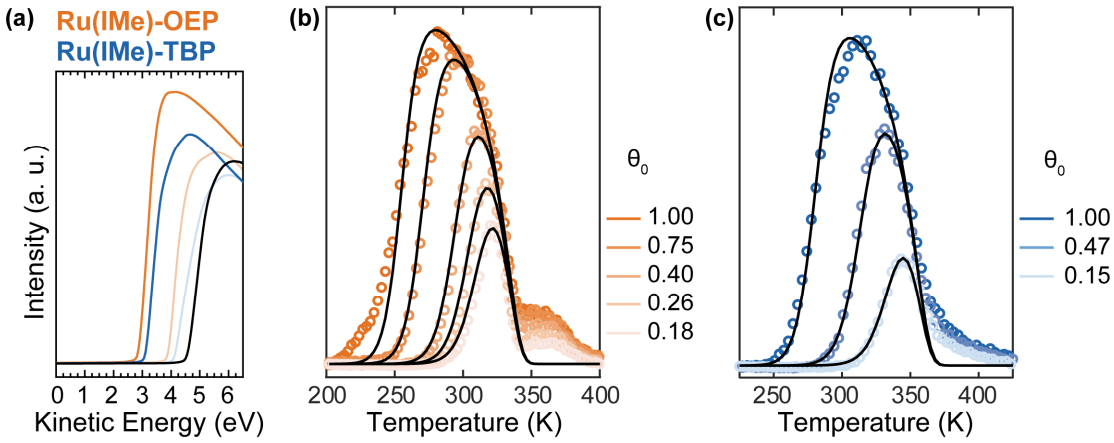

Figure 7.2: (a) XPS secondary electron cutoff measurements of the compressed phase Ru(IMe)-OEP (orange) and Ru(IMe)-TBP (blue) functionalized Ag(111) surface and a clean Ag(111) surface (black) used to determine the respective work function changes. The spectra of the uncapped porphyrins from Figure 6.4c are given in the respective lighter color tone of the corresponding porphyrin as comparison. Coverage dependent, fitted TPD data of IMe desorption of (b) Ru-OEP and (c) Ru-TBP on Ag(111) by assumption of a coverage dependent change of the desorption energy ($E_d(\theta) = E_d(\theta_0) - E_{des}\cdot\theta$). The initial coverage of each spectrum is shown.

For Ru-OEP, a high temperature desorption signature of IMe surface species can be observed in the TPD spectra at temperatures above 350 K (Figure 7.1a). This peak is already present at very low Ru(IMe)-OEP coverages and is not significantly increased by higher coverages of carbene capped porphyrins. The TPD spectra of Ru-TBP also exhibit a tail towards higher temperatures, but no distinct peak (Figure 7.1b). Since the experiments were performed on a fully porphyrin covered surfaces, we assume that the high temperature

desorption is related to IMe molecules bonded to porphyrins on step edges and/or on other defect sides, or IMe molecules directly bonding to free step edges.

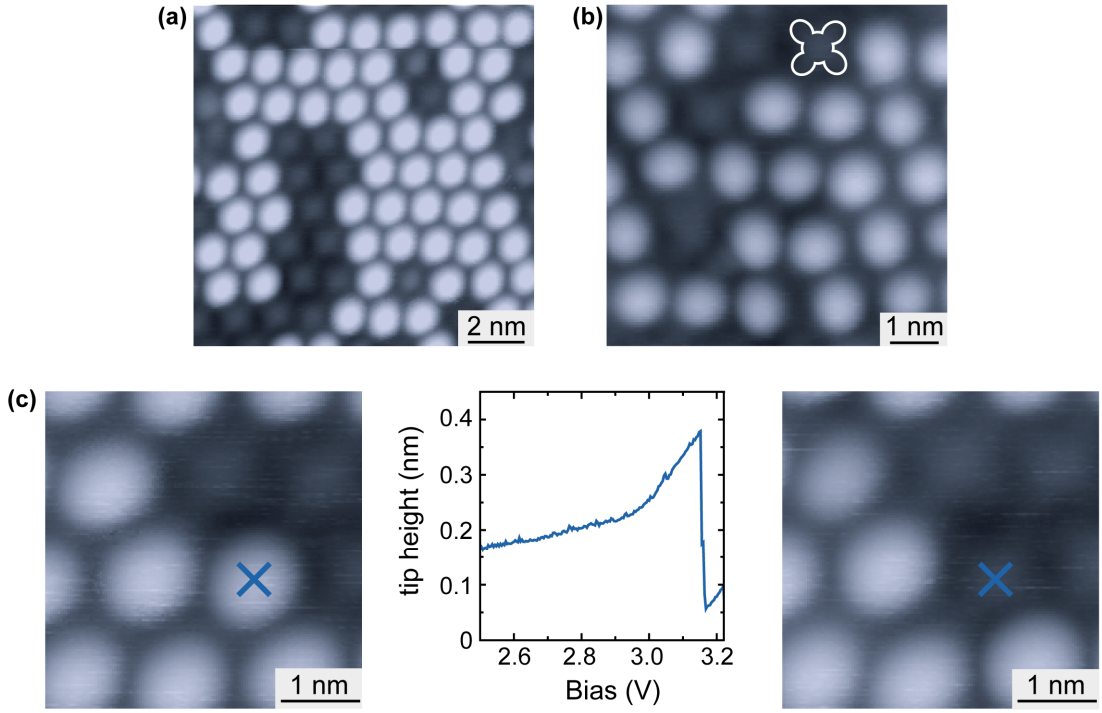

Figure 7.3: (a) STM image of Ru(IMe)-TBP (20 pA, 200 mV, 5 K). (b) High resolution STM image of Ru(IMe)-TBP (20 pA, 200 mV, 5 K). Differences in orientation of the carbenes are observable. An uncapped Ru-TBP molecule is outlined in white. (c) STM image of an IMe capped Ru-TBP molecule, marked by a blue cross, before (left) and after (right) removal of the carbene with the tip (50 pA, 200 mV, 5 K). The spectrum in the middle shows a plot of the applied bias *vs.* the tip displacement at a fixed tunneling current (50 pA). At 3150 mV, the carbene is lifted, and thus the tip decreases in height.

We used STM measurements to confirm IMe binding to the metal centers. Figure 7.3a shows IMe capped Ru-TBP molecules as bright protrusions at 5 K. The orientation of IMe uncapped Ru-TBP molecules is distinguishable, allowing to observe the self-assembly of the pedestal beneath the carbenes (Figure 7.3b, outlined in white). Therefore, we can also deduce from STM that no significant change in the self-assembly upon IMe adsorption takes place. In high resolution STM images, variations in the orientation of the IMe molecules were discernable (Figure 7.3b). This observation indicates potential occurrence of dynamic effects at elevated temperatures, likely originating from the rotational movements of the adsorbed IMe on the pedestal. Figure 7.3c shows the interaction of the STM tip with a single carbene molecule (marked with a blue cross). The tip position was fixed on top of the carbene. When increasing the bias to 3150 mV, a drop in the z position was observed, indicating the removal of the carbene. The STM image after the spectrum shows an uncapped porphyrin at the position of the former IMe capped porphyrin. The controlled removal of IMe molecules from the porphyrin pedestal demonstrates the potential for 2D data storage applications.

Subsequently, XPS experiments with a synchrotron light source were performed to see potential chemical changes upon IMe ligation. To prevent beam damage and IMe desorption with beam exposure, the photon intensity was reduced and the beam was suitably defocused. Therefore, the signal-to-noise ratio in this chapter is lower than in the previous chapter. The chemical state of the porphyrins' metal center was evaluated by the Ru $3d_{5/2}$ peak, which is shifted to higher binding energies upon ligation: to 280.4 eV for Ru-OEP (Figure 7.4a, top) and to 280.5 eV for Ru-TBP (Figure 7.4a, bottom). Thus, a decoupling of the metal centers to the substrate takes place, resulting in the reduction of the charge transfer from the substrate. Furthermore, the Ru $3d_{5/2}$ peak is broadened upon IMe ligation for both porphyrins. For Ru-OEP/Ru-TBP, the full width at half maximum values of the Ru $3d_{5/2}$ peak were determined to change from 0.29/0.31 eV before ligation to 0.64/0.52 eV after ligation, respectively. The broadening can be tracked by XPS as the coverage of IMe-capped molecules increases (Figure 7.4b). This differs significantly from the behavior observed for Ru(IMe)-TPP/Ag(111), where similar broad peaks with and without IMe ligation to the metal center were detected [83]. It is reasonable to assume that only intact IMe binds to the Ru metal center, since no bond cleavages during IMe evaporation or on the surface have been reported [45, 83]. Hence, a broadening of the XPS spectra suggests a less uniform environment for the Ru(IMe) metal centers.

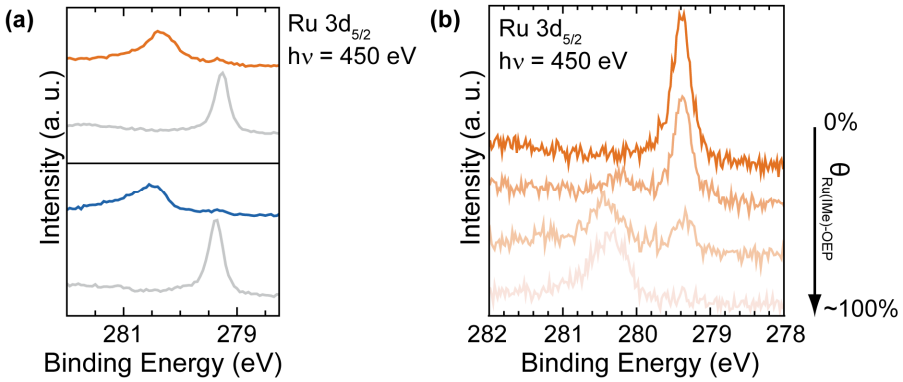

Figure 7.4: (a) XP spectra of Ru $3d_{5/2}$ core level of IMe on Ru-OEP (orange, top) and Ru-TBP (blue, bottom). The XP spectra of the respective uncapped porphyrin interface are given in grey in the corresponding panel. (b) IMe coverage dependent XP spectra of Ru $3d_{5/2}$. The IMe capped porphyrin coverage is increased from top to bottom.

The C 1s core level spectrum of Ru(IMe)-OEP shows a shift of 0.2 eV to higher binding energies (Figure 7.5a). This is attributed to a lifting of the porphyrin pedestal upon IMe ligation and therefore a reduction of the surface charge transfer to the porphyrins and/or of the screening by the substrate. The distinct peak of the methyl end groups of the ethyl chains at 284.1 eV is still observable. The C 1s core level of Ru(IMe)-TBP shows a similar shift to higher binding energies (Figure 7.5a).

For both porphyrins, the state near the Fermi edge of the uncapped porphyrin associated with interactions of the Ru metal center with the substrate is quenched upon ligation (Figure 7.5b) [50]. This proves the reduction of the charge transfer from the substrate to the metal center and hence an electronic decoupling. At Ru-OEP, the HOMO and HOMO-1 are shifted to lower binding energies upon ligation, whereas a shift to higher binding energies is observed for Ru-TBP. Carbene adsorption thus affects the valence band for the two porphyrin Ag(111) interfaces differently.

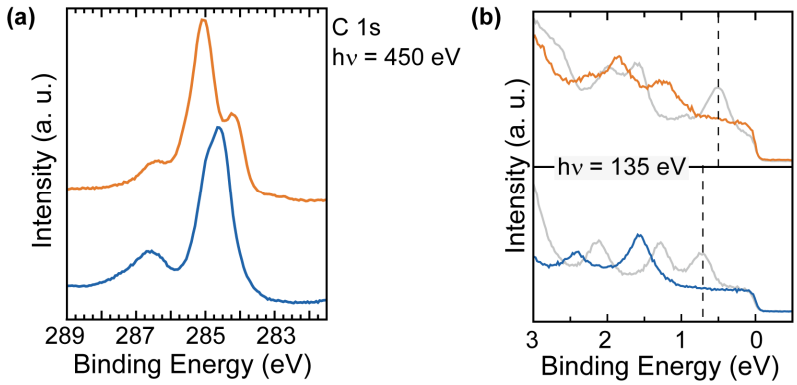

Figure 7.5: (a) C 1s core level XP spectra of Ru(IMe)-OEP (orange) and Ru(IMe)-TBP (blue). (b) Valence band of Ru(IMe)-OEP (top, orange) and Ru(IMe)-TBP (bottom, blue). The valence band spectra of the respective uncapped porphyrin interface are given in grey in the corresponding panel.

The out-of-plane orientation of the capped molecules from the surface was investigated by NIXSW measurements (Figure 7.6 and Table 7.1). The Ru $3d_{5/2}$ was used for the evaluation of the ruthenium adsorption height. Ru(IMe)-OEP exhibits a decrease in coherent fraction of Ru by 0.2 compared to the uncapped Ru-OEP (0.62 ± 0.09). Due to ligation of only IMe to the Ru metal center and no change in the self-assembly, a coherent fraction of 0.62 can be possibly explained by two distinct adsorption heights or a distribution of adsorption heights [85]. Two distinct adsorption heights would imply a difference of 0.83 Å between them. This high value seems unreasonable for interactions with the same ligand. Therefore, a distribution of adsorption heights of 0.3 Å is proposed. Alterations in adsorption heights with the same ligand would suggest an unprecedented variation of the adsorbed ligand binding, presumably linked to a variation of the NHC-Ru_{porph}-$Ag_{surface}$ *trans* ligands. The metal center is then elevated at different heights upon IMe adsorption. This observation is consistent with the broadening of the Ru $3d_{5/2}$ peak seen in XPS. Ru-TBP shows a similar decrease in coherent fraction of ruthenium, from 0.94 ± 0.13 to 0.60 ± 0.10, as Ru-OEP with a coherent position of 0.41 ± 0.05 (Table 7.1 and Table 6.3). Therefore, similar considerations have to be assumed for the IMe ligation to the metal center as for Ru-OEP/Ag(111). Thus, we assume that the higher temperatures IMe desorption species, which were predominantly seen at Ru-OEP, is not the major contribution to the loss in coherent fraction.

Table 7.1: Summary of the NIXSW measurements of Ru(IMe)-OEP and Ru(IMe)-TBP on Ag(111). The given binding energy is deduced from the fitted C 1s core level XP spectrum of Ru-OEP. Note that the given adsorption heights are just an average and for the respective coherent fraction, no single adsorption height can be assumed.

Component	Binding Energy (eV)	f_{111}	P_{111}	Adsorption height (Å)
Ru(IMe)-OEP				
C 1s	285.1	0.31 ± 0.03	0.29 ± 0.02	3.04 ± 0.05
C 1s	284.1	0.61 ± 0.04	0.30 ± 0.02	5.41 ± 0.05
Ru $3d_{5/2}$	-	0.62 ± 0.09	0.36 ± 0.05	3.21 ± 0.12
Ru(IMe)-TBP				
C 1s	-	0.52 ± 0.02	0.34 ± 0.01	3.16 ± 0.02
Ru $3d_{5/2}$	-	0.60 ± 0.10	0.41 ± 0.05	3.33 ± 0.12

The average adsorption height of the Ru metal center deduced by NIXSW for a fully IMe capped Ru-OEP and Ru-TBP interface is 3.21 ± 0.12 Å and 3.33 ± 0.12 Å, respectively. The higher average adsorption height of Ru corresponds to a higher desorption energy of IMe on Ru-TBP/Ag(111). Moreover, these values align with the data for the square phase Ru-TPP on Ag(111), which exhibits an adsorption height of 3.48 ± 0.09 Å and a higher IMe desorption energy (0.93 to 1.00 eV) [83]. The difference in average adsorption height could, therefore, be correlated with the binding strength of IMe. However, the uncertainty of the values is high and allows only tentative conclusions. DFT optimizations of the structure would help to improve the understanding further. It is also to note that aside from differences in adsorption strength, adsorption height differences of the Ru atoms might also be caused by steric or electronic effects of, e.g., the porphyrins.

The C 1s core level of Ru-OEP was analyzed by fitting two peaks, as described in the previous chapter. The coherent fractions of the carbon peaks are similar for the porphyrins with and without IMe ligation (Table 7.1 and Table 6.3). For the methyl $–CH_3$ species of the ethyl side chains, the average adsorption height increases by just 0.07 Å. The remaining carbon atoms are at an average increased distance of 0.21 Å. Therefore, the lifting of the porphyrins by IMe ligation is mostly seen on the adsorption height of the porphyrin's macrocycle. Due to the different lifting of the carbon species, it can be assumed that the conformation of the IMe capped porphyrin is slightly changed compared to the uncapped species. For Ru-TBP, the C 1s signal of the IMe uncapped and capped Ru-TBP was analyzed by fitting with one peak instead of the two peak fit discussed in the previous chapter due to the higher signal-to-noise ratio. Lift of an average adsorption height of 0.16 Å between Ru-TBP (f_{111} = 0.49 ± 0.03 and P_{111} = 0.27 ± 0.02) and Ru(IMe)-TBP on Ag(111) was obtained. The lifting effect of adsorbed IMe is, hence, not limited to the Ru metal center but also impacts the porphyrin molecule.

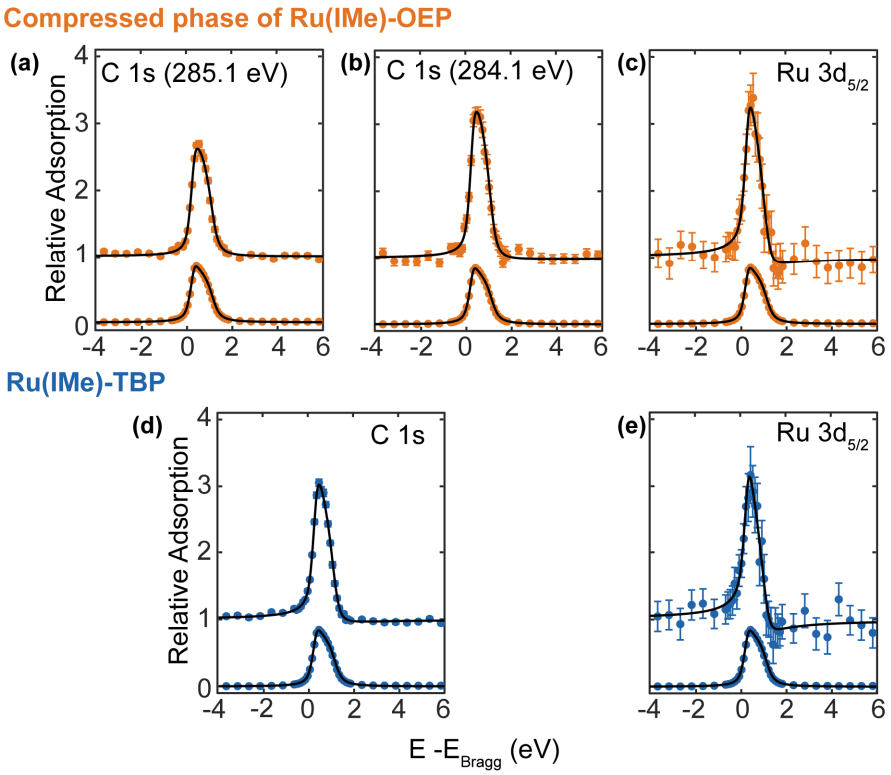

Figure 7.6: The (111) NIXSW data of Ru(IMe)-OEP ((a)-(c)) and of Ru(IMe)-TBP ((d), (e)). The coherent position and coherent fraction of the fits are summarized in Table 7.1.

To infer the orientation of the carbene and the porphyrins, NEXAFS measurements were conducted. In the π* region of the N K-edge, the resonance at a photon energy of 398.8 eV (marked by a black cross in Figure 7.7a,b) exhibits the expected dichroism of the porphyrins [213, 221-222, 224, 248]. The highest intensity is observed when the linear X-ray polarization has a 30° tilt to the surface (predominantly perpendicular), whereas with a parallel alignment the features are mostly suppressed. However, in both spectra a new feature at a photon energy of 402.1 eV with an inverse dichroism to the porphyrins' can be observed. This resonance is attributed to the carbene [249]. It shows the highest intensity at a parallel X-ray polarization to the surface normal. Polarization-dependent π* resonance intensities were used for the derivation of the tilt angles of the carbene and the porphyrin by standard procedures [77, 80]. For Ru-OEP and Ru-TBP, tilt angles of 9° ± 5° and 15° ± 5° were obtained, respectively (Figure 7.7c,d). Therefore, there is an increase in the tilt angle of 4° and 10° compared to the respective uncapped molecules. This is attributed to conformational changes of the macrocycle upon adsorption, which were previously observed for different porphyrins [237]. IMe adsorption on Ru-TBP shows a stronger effect on the porphyrin macrocycle than on Ru-OEP. Thus, a higher adaptation of Ru-TBP upon ligation can be assumed, which could also strengthen the IMe-Ru bond or, in reverse, a low conformational adaptation could weaken the bond for Ru(IMe)-OEP.

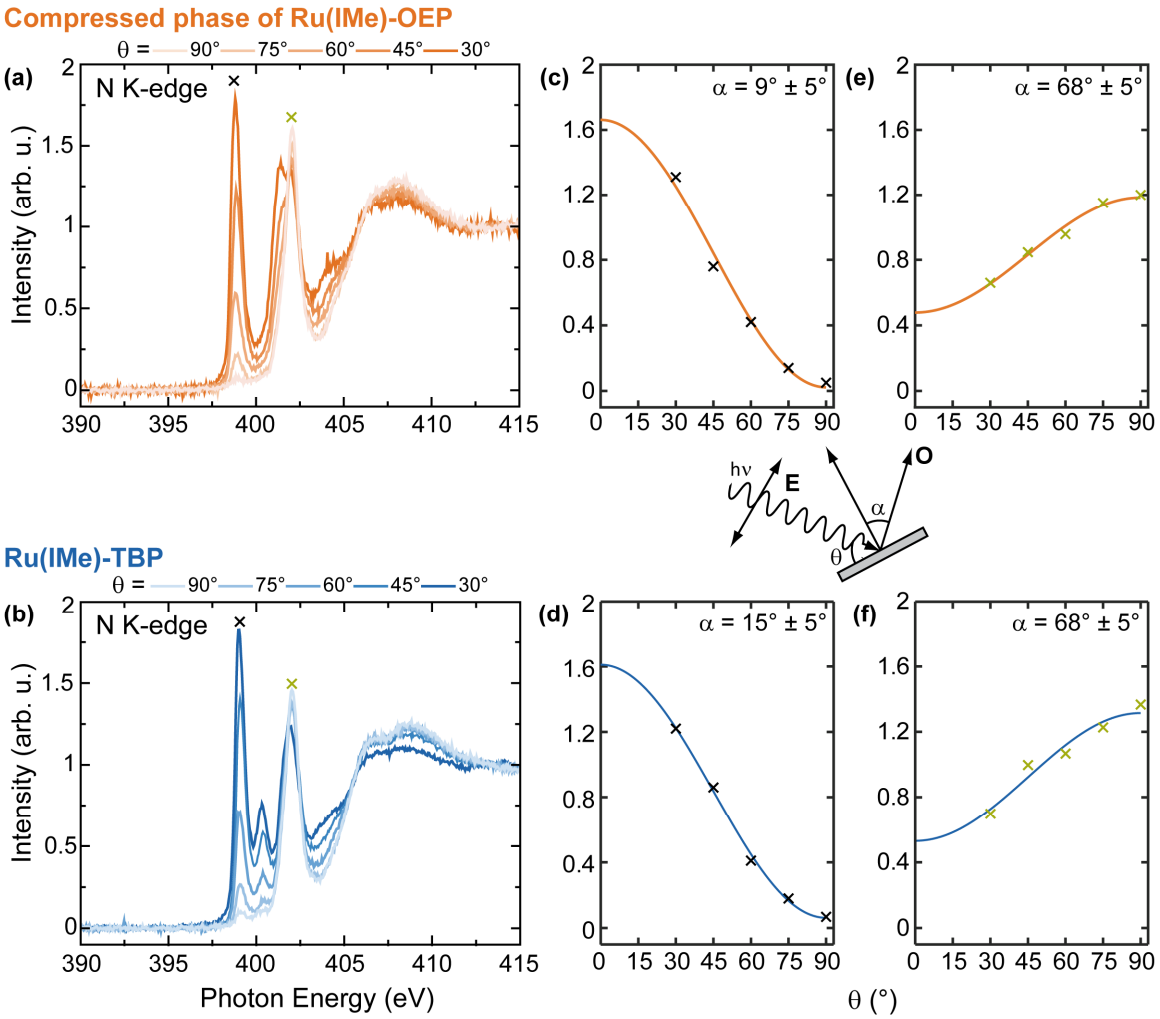

Figure 7.7: N K-edge NEXAFS of (a) Ru-OEP and (b) Ru-TBP on Ag(111). Fitted data for the porphyrin macrocycle of (c) Ru(IMe)-OEP and (d) Ru(IMe)-TBP and the carbene of (e) Ru(IMe)-OEP and (f) Ru(IMe)-TBP. The peaks for the fits are marked by the corresponding colored crosses in (a) and (b). The inset shows the corresponding angles in (c) and (f).

For the carbene, an angle of 68° was derived for both interfaces, making the adsorbed carbene bend by 22° from the substrate normal (Figure 7.7e,f). A stable coordination bond with the Ru metal center at 22° of the surface's normal seems unlikely due to the weakened orbital overlap of ligand and metal center. Furthermore, a uniform adsorption geometry of the ligand does not align with the observation by XPS and NIXSW. Hence, we propose a dynamic behavior for the adsorbed carbene, suggesting that the value derived from NEXAFS represents an averaged angle over time. An oscillation from one side to the other would change the interaction with the Ru metal center due to different alignments of the ligand's and metal center's orbitals. A strengthening or weakening of the IMe-Ru bond would affect the adsorption height of the metal center. At a temperature of 200 K, a movement is still reasonable to assume. This could explain the drop in coherent fraction observed in NIXSW and the

broadening observed in XPS. Molecular dynamic calculations are planned to substantiate or invalidate the proposed interpretation.

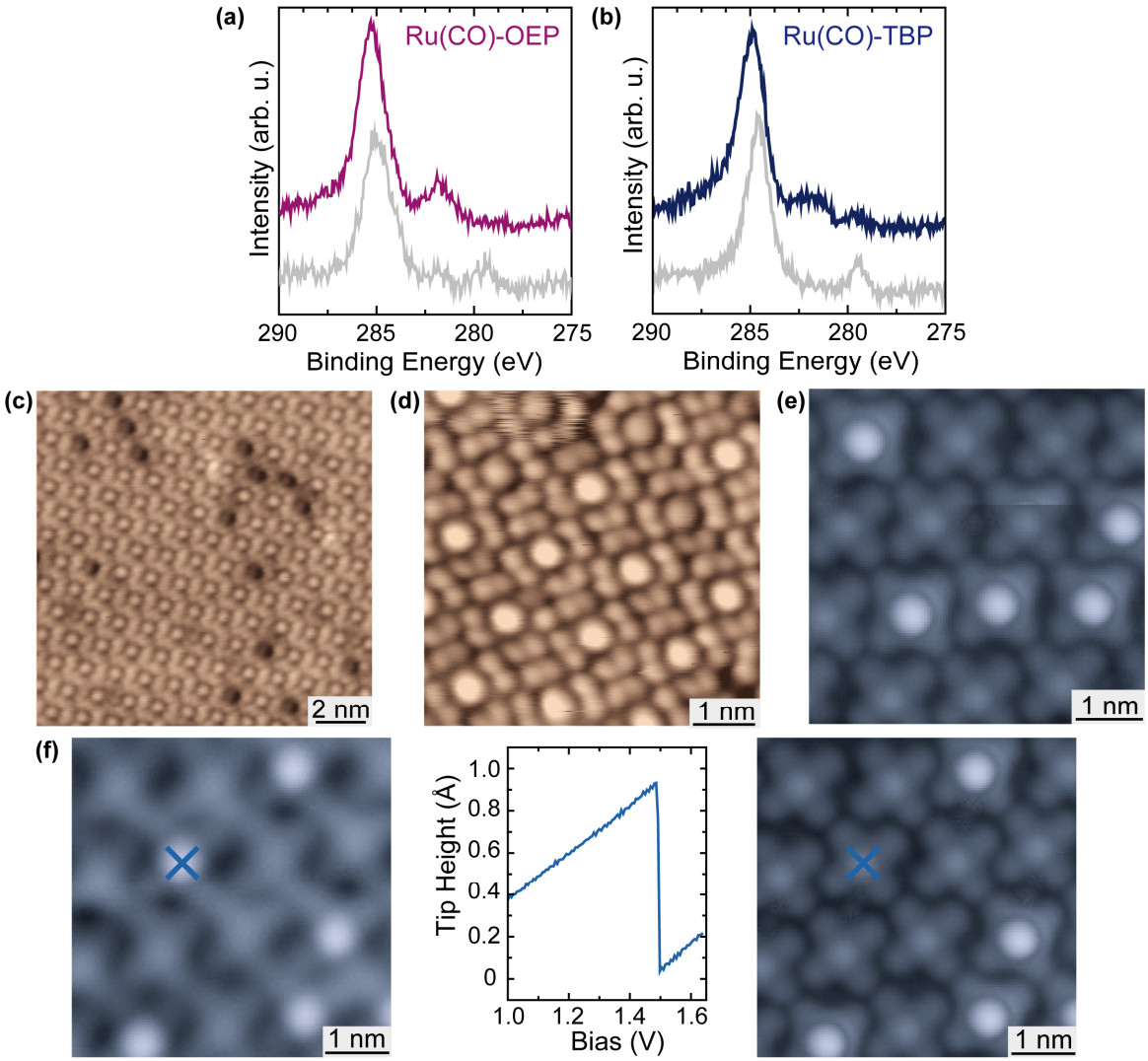

Figure 7.8: C 1s and Ru $3d_{5/3}$ core level XP spectra of (a) Ru(CO)-OEP (purple) and (b) Ru(CO)-TBP (dark blue). The respective uncapped porphyrin spectrum was added in grey. STM image of (c,d) Ru(CO)-OEP (c: 1051 mV, 50 pA, 150 K; d: -33 mV, 30 pA, 150 K) and (e) Ru(CO)-TBP (200 mV, 50 pA, 5 K). (f) STM tip interaction with Ru(CO)-TBP on Ag(111). The left, middle and right panel shows an STM images before removal, bias *vs.* tip height z and an STM image with the uncapped Ru-TBP (both STM images: 200 mV, 50 pA, 5 K). The position of the tip during the bias increase is marked by a blue cross. The STM image resolution is strongly improved after the CO removal and is assumed to be caused by a functionalization of the STM tip with CO.

CO adsorption on ruthenium porphyrins on Ag(111)

The initially showed CO desorption data are impossible to model assuming a first order desorption with a single desorption energy. This is also reported for Ru(CO)-TPP on Ag(111) [223]. XPS was performed to analyze the changes upon CO adsorption for Ru-OEP and Ru-TBP on Ag(111) (Figure 7.8a,b). A shift to 281.9 eV and 281.7 of the Ru $3d_{5/2}$ peaks upon

CO ligation was observed for Ru-OEP and Ru-TBP, respectively. This strong shift is characteristic for CO adsorption [223]. We investigate the behavior of CO adsorption with STM. Figure 7.8c shows an STM image of Ru-OEP with nearly all centers capped by CO. The depressions correspond to the uncapped molecules, and the bright protrusions to the CO capped porphyrins. Figure 7.8d has a zoomed-in image of uncapped and capped Ru-OEP molecules. At 5 K, only monocarbonyl Ru-TBP species can be observed as bright protrusions (Figure 7.8e). STM tip functionalization with adsorbed CO on Ru-OEP was achieved at 5 K observable by the resolution increase in the STM image after picking up a CO at high biases, which is typical for a CO functionalized tip (Figure 7.8f).

Conclusion

We investigated the ligation behavior of CO and IMe to the metal center of Ru-OEP and Ru-TBP on Ag(111). The porphyrins show a different trend in the desorption temperatures for CO and IMe. CO has a lower desorption temperature on Ru-TBP than on Ru-OEP, whereas IMe exhibits a lower desorption temperature on Ru-OEP compared to Ru-TBP. Furthermore, the CO desorption temperature on Ru-TBP (248 K) seems unexpectedly low compared to Ru-OEP (282 K) and Ru-TPP (300 K) [223], especially when taking into consideration the IMe desorption temperatures of the respective porphyrins. Hence, the strength of ligand binding is influenced not only by the choice of substrate and metal center but also significantly by the entire structure of the porphyrin molecules. This variability can result in opposite systematics for different ligands. Consequently, this study underscores the impact of porphyrin substituents on ligation to the metal centers. Moreover, through various experimental methods, this study unveiled strong indications of the coexistence of diverse Ru(IMe) states for both porphyrins. We proposed a dynamic tilting of the carbene from the surface normal, which affects the orbital overlap of ligand and metal center and, hence, the *trans* effect. A theoretical driven investigation was started to validate or invalidate the proposed dynamics of the ligand.

8 Passivation of a Metal Surface Strengthens the Binding of an N-heterocyclic Carbene to a Metalloporphyrin Pedestal

At all the IMe porphyrin interfaces described in the previous chapter, as well as at Ru(IMe)-TPP on Ag(111) [42], desorption at or below RT occurs, rendering the systems not stable at RT for long periods. This prompts the question: How can the binding strength of IMe to Ru be further enhanced? Previous investigations have demonstrated profound effects resulting from decoupling of organic molecules from metal substrates passivated by interlayers, including changes in conformation [250], adsorption behavior [251] and distance to the substrate [252]. Porphyrins' and phthalocyanines' metal centers were analyzed with spectroscopic methods and showed electronic decoupling from the substrate [40, 253-254]. The surface passivation was realized by different interlayers on the metal substrate, such as molecular interlayers [37, 255-256], oxidized metal surfaces [40, 253-254, 257-259], non-metallic 2D materials [260-264] or intercalation of iodine [251-252, 265].

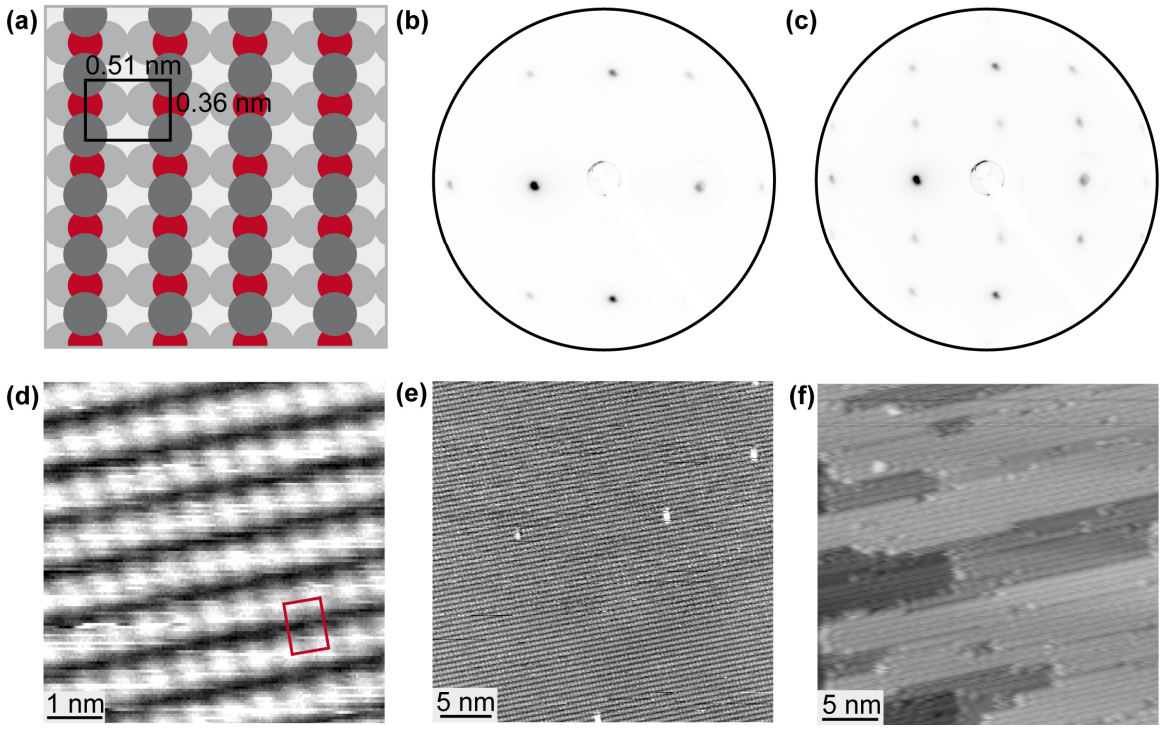

Figure 8.1: (a) Schematic of the Cu(110)-(2×1)O reconstruction [266-267]. The copper atoms and the oxygen atoms are colored in grey and red, respectively. (b) LEED pattern of Cu(110) and of Cu(110)-(2×1)O with an electron energy of 100 eV. (d) STM image of Cu(110)-(2×1)O after deposition of O_2 with the sample at 500 K (312.5 mV, 50 pA, RT). The unit cell is highlighted in red. Overview STM images of Cu(110)-(2×1)O after O_2 exposure to a sample (e) at 500 K (312.5 mV, 50 pA, RT) and (f) at RT (156 mV,140 pA, RT).

Here, we present a comparative study on the effect of a chemical modification of the metal surface on the IMe-Ru binding strength in UHV. As a substrate, we chose Cu(110) because it is reported to form a (2×1)O reconstruction upon oxygenation (Figure 8.1a). The response to adsorption of the carbene to Ru-OEP was examined on both Cu(110) and Cu(110)-(2×1)O. Our characterization employed a multiple-technique approach with STM, XPS, UPS, and TPD. The Cu(110)-(2×1)O surface was prepared by exposing a clean Cu(110) surface to 10^{-8} mbar of O_2 for 2 min (VT-STM chamber) or 20 L O_2 (PSD chamber) while holding the sample at 500 K. A fully reconstructed surface with extended, atomically planar domains was observed in LEED (Figure 8.1b,c) and STM (Figure 8.1d,e). When the same procedure was performed with a sample at RT, a much more stepped surface was obtained (Figure 8.1f).

Self-assembly of Ru-OEP on Cu(110) and Cu(110)-(2x1)O

The self-assembly and quality of the porphyrin overlayers were investigated by STM. Ru-OEP on Cu(110)-(2×1)O forms islands with stripes composed by two species with their apparent heights differing by approximately 1 Å from each other (Figure 8.2a,b). Both species have similar lateral dimensions and comprise a central protrusion surrounded by eight smaller protrusions (Figure 8.2c). The central feature is attributed to the porphyrin ring with a Ru center, and the smaller protrusions of varying contrast to the ethyl side chains [37, 226, 228]. As the free base octaethyl porphyrin exhibits a dark center rather than a protrusion [111, 228, 230], intact Ru-OEP molecules are assigned to both species. LEED shows that the (2×1)O reconstruction is still present beneath the self-assembly (Figure 8.2d). On the Cu(110) surface, a similar shape can be identified for the single molecule, albeit at a uniform apparent height (Figure 8.2e), indicating a well-defined and equal adsorption configuration. The molecules self-assemble in at least two close packed structures, which feature a large density of domain boundaries, indicative of limited mobility during island formation (Figure 8.2e). In contrast, the domains on Cu(110)-(2×1)O are well organized without irregularities or phase transitions (Figure 8.2a). This is attributed to higher mobility and weaker interactions of the porphyrin with the Cu(110)-(2×1)O substrate.

Next, the apparent height variations of the Ru-OEP on Cu(110)-(2×1)O are addressed, which are not observed on the pristine Cu(110). The molecule rows are twisted by 43° ± 2° with respect to the Cu-O-rows of the substrate. When the Cu(110)-(2×1)O structure is overlaid with an STM image (Figure 8.2f), an alteration in Ru centers' adsorption sites can be observed: it can either be on top of a Cu-O-row or in between them. Thus, the contrast alterations can be well correlated with a difference in the adsorption site. It is further noted that the brighter ethyl chain pairs are located in the direction of the Cu-O-rows.

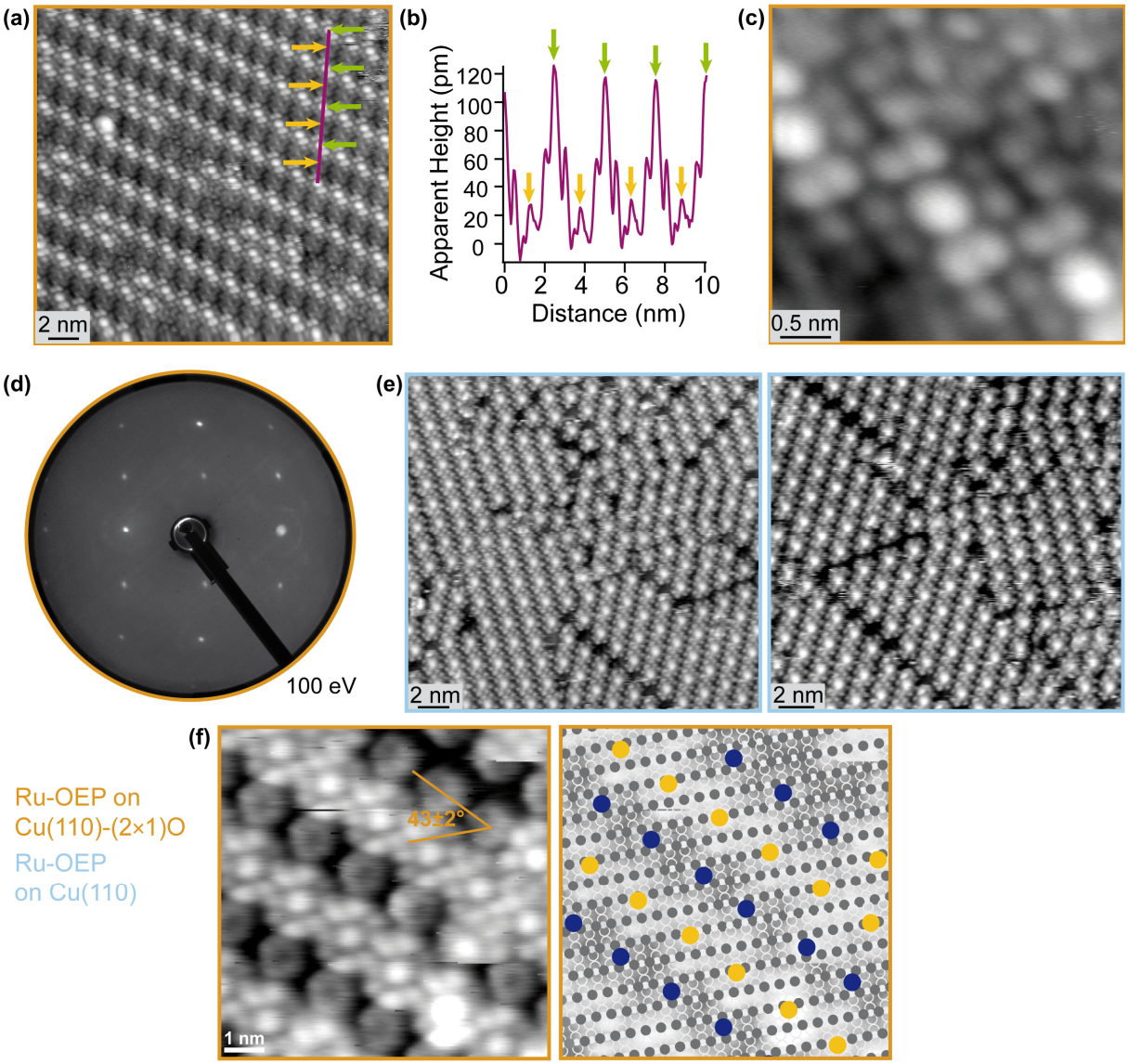

Figure 8.2: (a) STM image of Ru-OEP on Cu(110)-(2×1)O (1051 mV, 100 pA, RT). (b) Line profile corresponding to the purple line indicated in (a). The arrows emphasize the positions of the porphyrin centers. (c) High-resolution STM image of the two Ru-OEP species with different apparent height on Cu(110)-(2×1)O (1487 mV, 80 pA, RT). (d) LEED of Ru-OEP on Cu(110)-(2×1)O with an electron energy of 100 eV. The (2×1)O reconstruction is still intact after deposition of Ru-OEP (compare Figure 8.1c). (e) STM images of Ru-OEP on Cu(110) (both: -156 mV, 20 pA, RT). (f) STM image of Ru-OEP on Cu(110)-(2×1)O (20 pA, -1250 mV, RT) with the substrate highlighted on top of the right image. The centers of the two Ru-OEP species with different apparent heights in STM are marked in yellow and dark blue, respectively.

Thermal stability of Ru-OEP on Cu(110) and Cu(110)-(2×1)O

In order to gain insight into the thermal stability of the Ru-OEP/Cu(110)-(2×1)O interface, a TPD study supported by XPS measurements was conducted (Figure 8.3a). The TPD spectra unveil significant desorption peaks at *m/z* 18, 27, 28, and 44 at approximately 450 K. Additionally, trace amounts of *m/z* 13, 14, 15, 29, 43, and 45 were also discerned at this

temperature. Hydrogen (*m/z* 2) desorption became apparent at temperatures exceeding 500 K. Notably, no oxygen desorption (*m/z* 32) was detectable across the entire temperature range. For comparison, the same TPD procedure was employed for the Ru-OEP on the unreconstructed Cu(110) surface (Figure 8.3b), where only hydrogen (*m/z* 2) desorption was detected at temperatures above 500 K. Ring closure reactions of octaethyl porphyrins' side chains along with hydrogen formation are reported at similar temperatures on different substrates [111-112] and in previous chapters of this thesis. Hence, the observed hydrogen desorption is presumably caused by inter- and intramolecular reactions of the ethyl side chains on both substrates.

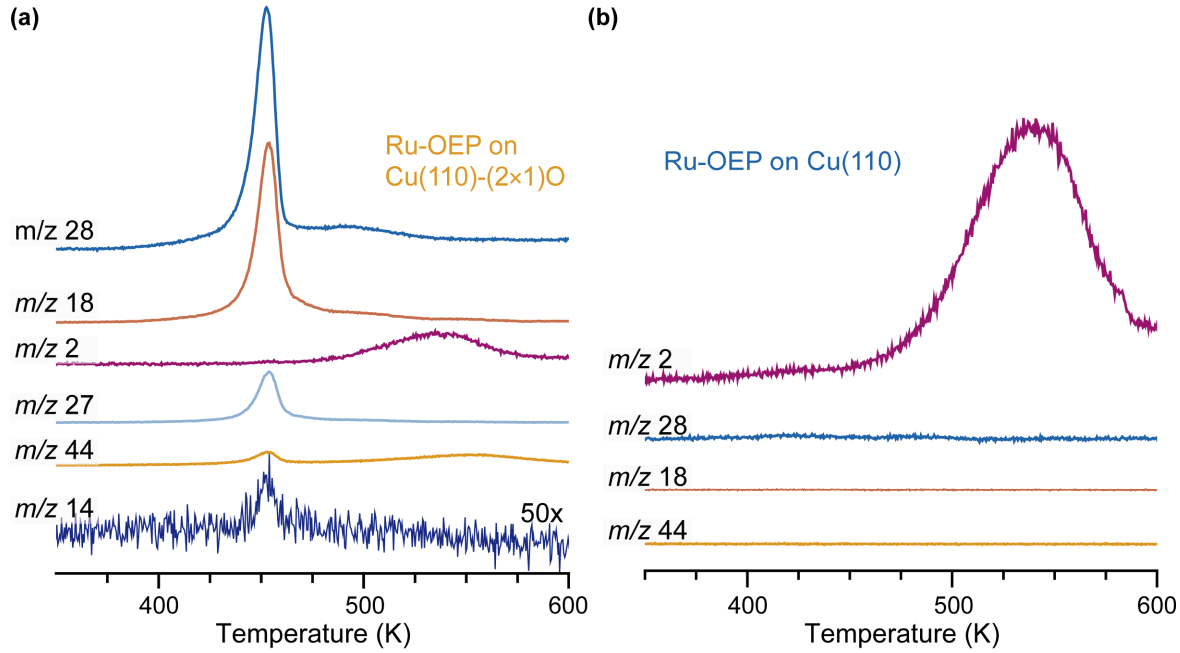

Figure 8.3: TPD spectra of Ru-OEP on (a) Cu(110)-(2×1)O and (b) Cu(110) from 350 to 600 K with a heating rate of 0.5 K s^{-1}. The *m/z* ratios are given next to the respective spectrum.

XPS experiments were performed to gain insight into changes in the chemical state of the Ru-OEP molecules and the Cu(110)-(2×1)O substrate during annealing (Figure 8.4a,b). The temperature differences between TPD and XPS data are due to variations in experimental procedures; each XPS spectrum was acquired after 10 min of annealing and not with a constant heating rate as in TPD. After annealing Ru-OEP/Cu(110)-(2×1)O to 420 K, loss of the surface oxygen (Figure 8.4b) and a shift of the Ru $3d_{5/2}$ peak from 281.2 to 279.5 eV (Figure 8.4a) were observed in XPS. The peak position of 279.5 eV is similar to the discussed position in Ru-OEP and -TBP on Ag(111) in previous chapters and Ru-OEP on Cu(110) (Figure 8.4c), indicating the formation of the metallic substrate. The XPS of Ru-OEP on Cu(110) shows no shift in the Ru $3d_{5/2}$ peak upon annealing (279.5 eV). A shift to a lower binding energy in the

carbon peak occurs, matching an increase in sp^2 hybridized carbons through the assumed ring closure reactions.

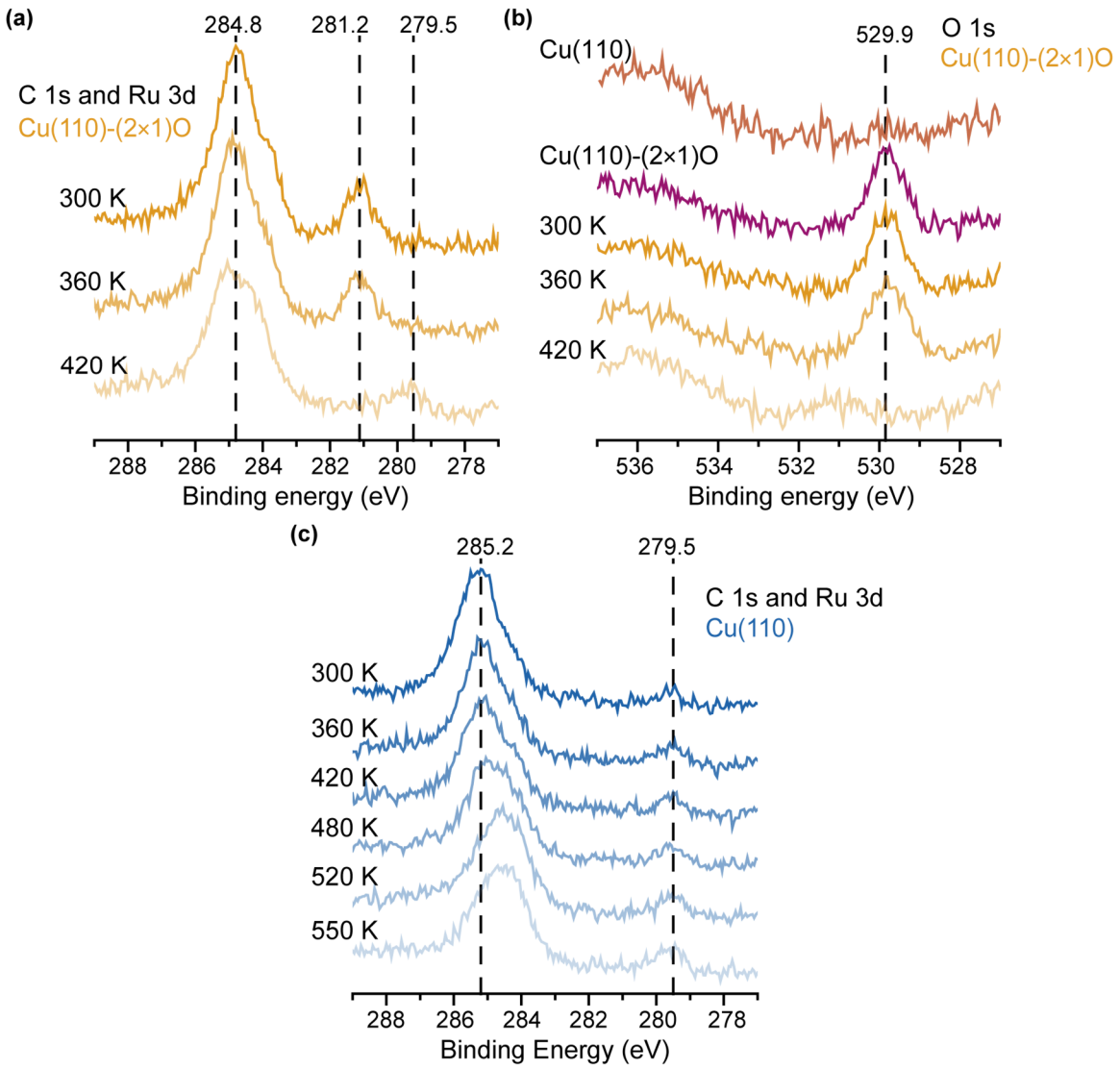

Figure 8.4: (a) C 1s and Ru 3d and (b) O 1s core level of stepwise annealed Ru-OEP on Cu(110)-(2×1)O. (c) C 1s core level of stepwise annealed Ru-OEP on Cu(110). Every spectrum was taken after 10 min annealing. The annealing temperature is given at the respective spectrum. All XPS data is taken with Mg Kα radiation (hν = 1253.6 eV).

The integrity of most porphyrin macrocycles after annealing is demonstrated by CO adsorption and desorption experiments using XPS and TPD (Figure 8.5). Upon CO adsorption, the XP spectrum of annealed Ru-OEP on Cu(110)-(2×1)O shows a shift of the Ru $3d_{5/2}$ peak from 279.5 to 281.1 eV (Figure 8.5a), previously also observed for Ru-TPP/Ru(CO)-TPP on Ag(111) [223]. The behavior of CO adsorption on Ru-OEP/Cu(110) also exhibits a similar trend. (Figure 8.5b). TPD experiments were performed on the CO exposed Ru-OEP/Cu(110) and annealed Ru-OEP/Cu(110)-(2×1)O, revealing CO desorption below 300 K (Figure 8.5c,d). However, the CO desorption peak on Ru-OEP/Cu(110) is sharper compared to that of the

annealed Ru-OEP/Cu(110)-(2x1)O. This difference is anticipated due to high variations in the porphyrins' substituents resulting from inter- and intramolecular ring closure reactions of the ethyl side chains. The effect of the substituents on CO adsorption was shown on Ru-OEP/-TBP on Ag(111) in a previous chapter. Given the similarity of CO adsorption and desorption on both systems, combined with the results from the XP measurements, it is assumed that the central porphyrin ring remains intact after annealing to 600 K. Consequently, reactions of the ethyl side chains with the surface oxygen are expected to lead to the observed products in TPD.

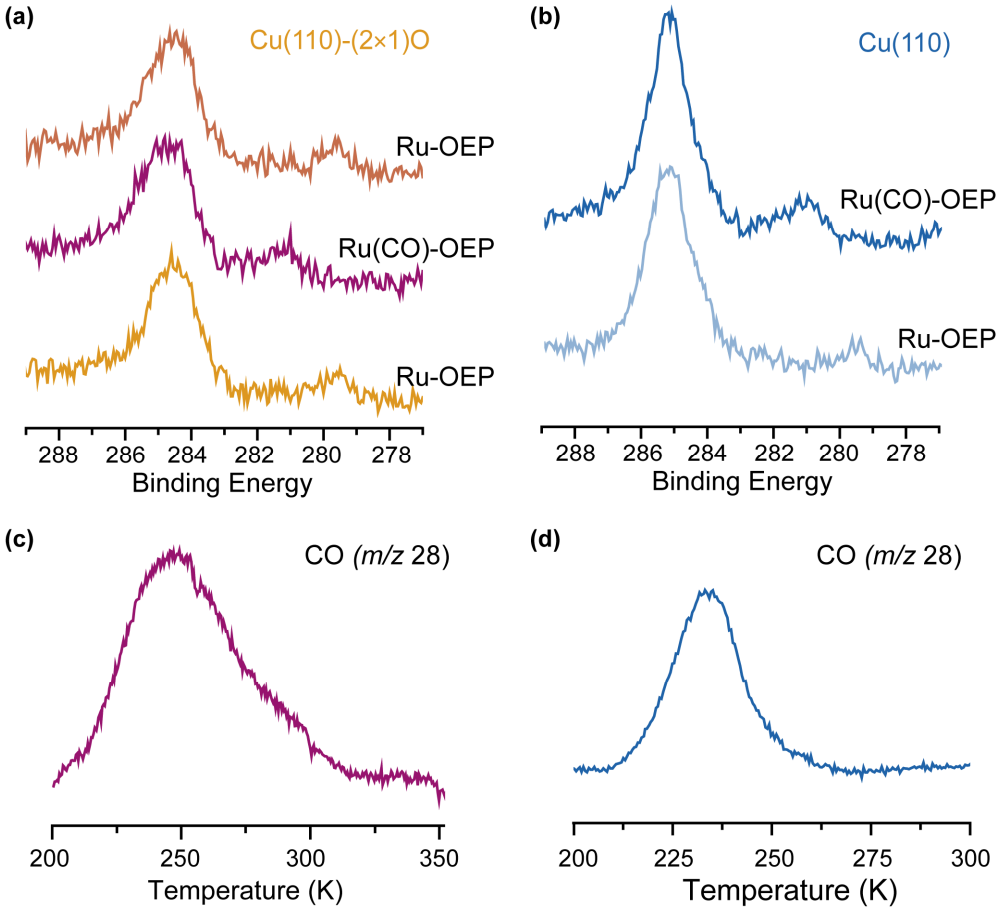

Figure 8.5: (a) Sequential XP spectra depicting Ru-OEP/Cu(110)-(2×1)O after annealing to 600 K (orange), following CO exposure (in purple), and after subsequent annealing to 600 K (in dark orange). (b) XP spectra of Ru-OEP/Cu(110) before (light blue) and after (dark blue) CO exposure. All XPS data were taken with Mg Kα radiation (hν = 1253.6 eV). TPD spectra of *m/z* 28 (CO) with a rate of 0.5 K s^{-1} of (c) the annealed Ru-OEP/Cu(110)-(2×1)O and (d) Ru-OEP/Cu(110) both after CO exposure.

With these observations by XPS, we proceed to explore potential species that align with the observed desorption in TPD. (Figure 8.3a). The likely explanation for the detected desorption peaks is a C–C bond cleavage reaction between the porphyrin macrocycle and the ethyl side chain, catalyzed by oxygen. The low abundance of *m/z* 14 and 15 (CH_2 and CH_3 species) suggests a limited occurrence of additional C–C bond cleavage of the CH_2CH_3 species formed by the ethyl side chains on the substrate. The data align well with ethylene (m/z 28, CH_2CH_2)

and acetaldehyde (m/z 44, $OCHCH_3$). The primary ionization product of ethylene, *m/z* 27 [268], is also observed in the mass spectrometer. Therefore, we propose the formation of CH_2CH_2 and $OCHCH_3$. Both proposed formation reactions lead to adsorbed atomic hydrogen. The adsorbed hydrogen and the surface oxygen subsequently combine to form the detected H_2O (*m/z* 18) in TPD. A complete oxidation of carbon to CO (*m/z* 28) and CO_2 (*m/z* 44) seems unlikely due to earlier desorption of intermediate products and the detection of the *m/z* 27 species in the mass spectrometer, which cannot solely be explained by CO formation. Nevertheless, the possibility of CO and CO_2 desorption cannot entirely be excluded. In summary, we propose a reaction scheme that includes three major steps: bond cleavage reaction of the ethyl side chains, formation of acetaldehyde/ethylene and water formation (Scheme 8.1).

Scheme 8.1: Proposed reactions of Ru-OEP on Cu(110)-(2×1)O at temperatures above 400 K.

Ethyl side chain bond cleavage:

$$(RuC_{20}H_4N_4)(CH_2CH_3)_8 + x\,O\,(ad) \longrightarrow (RuC_{20}H_4N_4)(CH_2CH_3)_{8-x} + x\,OCH_2CH_3\,(ad)$$

$$(RuC_{20}H_4N_4)(CH_2CH_3)_8 \xrightarrow{Cu(110)\text{-}(2x1)O} (RuC_{20}H_4N_4)(CH_2CH_3)_{8-x} + x\,CH_3CH_2\,(ad)$$

Acetaldehyde/Ethylene formation:

$$OCH_2CH_3\,(ad) \longrightarrow OCHCH_3\,(g) + H\,(ad) \quad (m/z\ 44)$$

$$CH_3CH_2\,(ad) \longrightarrow CH_2CH_2\,(g) + H\,(ad) \quad (m/z\ 28)$$

$$OCH_2CH_3\,(ad) \longrightarrow CH_2CH_2\,(g) + H\,(ad) + O\,(ad) \quad (m/z\ 28)$$

Water formation:

$$2\,H\,(ad) + O\,(ad) \longrightarrow H_2O\,(g) \quad (m/z\ 18)$$

IMe adsorption and desorption experiments

To investigate the initially predicted increase in thermal stability of the Ru-IMe bond on an oxidized Cu(110) surface, TPD measurements on monolayers of Ru(IMe)-OEP on Cu(110)-(2×1)O as well as on Cu(110) were performed (Figure 8.6a,b). On Cu(110)-(2×1)O, the IMe desorption maxima is at 415 K (Figure 8.6a). The shape of the TPD spectra suggests a complex desorption behavior; hence, a single binding energy for IMe desorption from Ru-OEP/Cu(110)-(2×1)O is not possible to derive. The discussed differences in adsorption sites of the porphyrins on the oxidized surface are presumably related to the shape of the IMe desorption spectra, as different adsorption configurations of the porphyrins are expected to impact the binding strength of the metal center to the carbene. By STM measurements, we

investigated the binding of the IMe at RT. It was possible to confirm that the carbene binds to the Ru center on Cu(110)-(2×1)O as every IMe molecule, observed as major bright protrusions, is situated in the center of an Ru-OEP position (Figure 8.6c). A comparison of the apparent height of the bright porphyrin centers and the adsorbed carbenes is shown in Figure 8.6c.

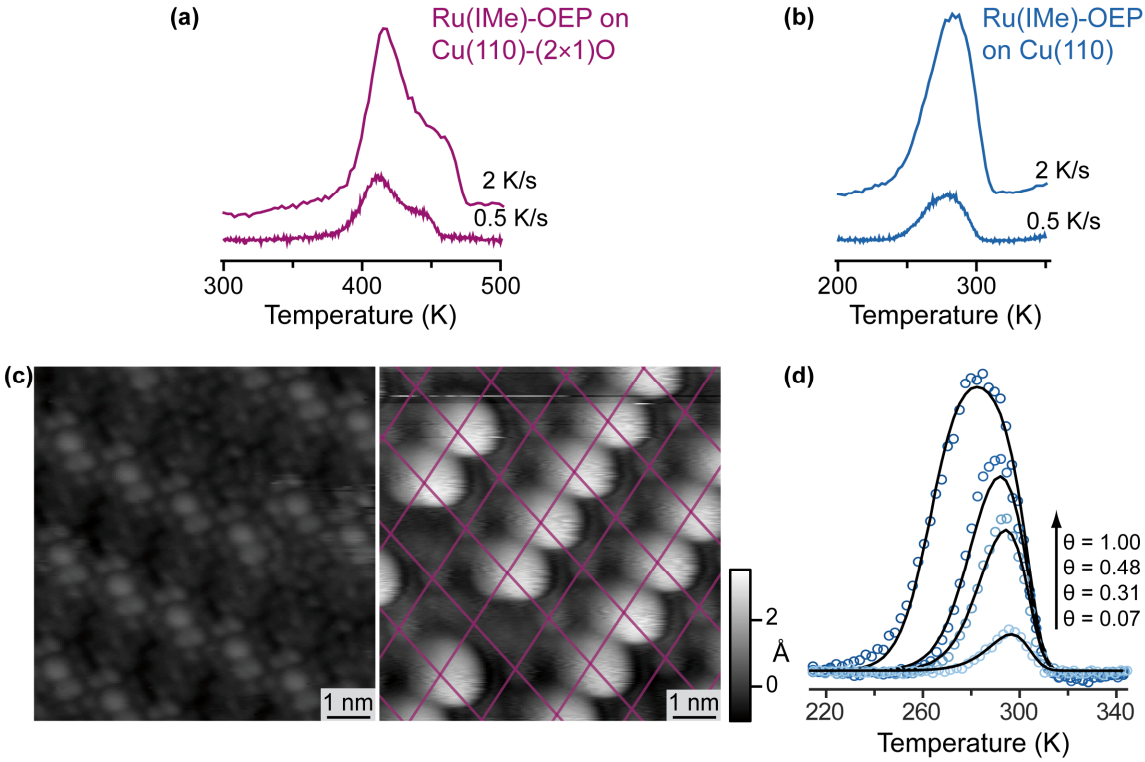

Figure 8.6: TPD spectra with different heating rates (2, 0.5 K s^{-1}) of IMe (*m/z* 96) from (a) Ru(IMe)-OEP/Cu(110)-(2×1)O and (b) Ru(IMe)-OEP/Cu(110). (c) Apparent height comparison of STM images of Ru-OEP on Cu(110)-(2×1)O (left, 1051 mV, 100 pA, RT) and Ru(IMe)-OEP on Cu(110)-(2×1)O (right, 1770 mV, 70 pA, RT). The scale was applied on both images, to show the difference in apparent height between the bright porphyrin centers and the adsorbed carbenes. The Ru-OEP positions are indicated by the purple grid in the right image. IMe is always on a Ru-OEP center position. (d) Fitted coverage dependent IMe (*m/z* 96) desorption spectra on Ru-OEP/Cu(110).

For IMe desorption on Ru-OEP/Cu(110), a coverage dependent binding energy of E_{des} = (0.92 eV - 0.7·θ) eV was derived (Figure 8.6d). The coverage dependent decrease most likely arises from repulsive dipole-dipole interactions of the carbenes [42, 247]. Comparing these IMe desorption spectra, one can find that the maximum of IMe desorption is 132 K lower on the bare metal substrate than on the reconstructed surface. Another substrate-pedestal system where IMe desorption was investigated is Ru(IMe)-TPP on Ag(111) [42]. IMe desorption has its maximum at a temperature of approximately 90 K lower than Ru(IMe)-OEP on Cu(110)-(2×1)O. A desorption energy of E_{des} = (1.08 eV - 0.12·θ) eV was derived for the binding strength of IMe on Ru-TPP on Ag(111) [42]. We can thus assume that the binding

strength of IMe to Ru-OEP on Cu(110)-(2×1)O has to be significantly higher than this, and hence, the stability of the Ru-IMe-bond has increased on the oxidized surface.

To obtain information on the chemical state and interaction with the surface, photoemission experiments were performed. The Ru $3d_{5/2}$ peak's position of 279.5 eV at Ru-OEP on Cu(110) is significantly shifted from the expected energy for Ru^{2+} and is comparable to ruthenium porphyrins on Ag(111) and to surface metallic ruthenium (Figure 8.7a) [231-232]. This is caused by charge transfer from the substrate to the molecules, as is also observed for other metal porphyrins on metal surfaces [38-39, 269]. The UP spectrum of Ru-OEP on Cu(110) is also indicative of this charge transfer, showing an additional energy state near the Fermi edge (Figure 8.7c, light blue spectrum) [270]. Both the energy state near the Fermi edge (Figure 8.7c, orange spectrum) and the Ru $3d_{5/2}$ core level shift (Figure 8.7b, orange spectrum) are absent for Ru-OEP/Cu(110)-(2×1)O. The Ru $3d_{5/2}$ peak is at 281.2 eV, in line with the expected oxidation state of the Ru center, which is also found for ruthenium porphyrins in a multilayer [223, 231, 233]. This suggests the absence of a charge transfer from the Cu(110)-(2×1)O substrate to the Ru center and thus an electronic decoupling of the porphyrin from the substrate.

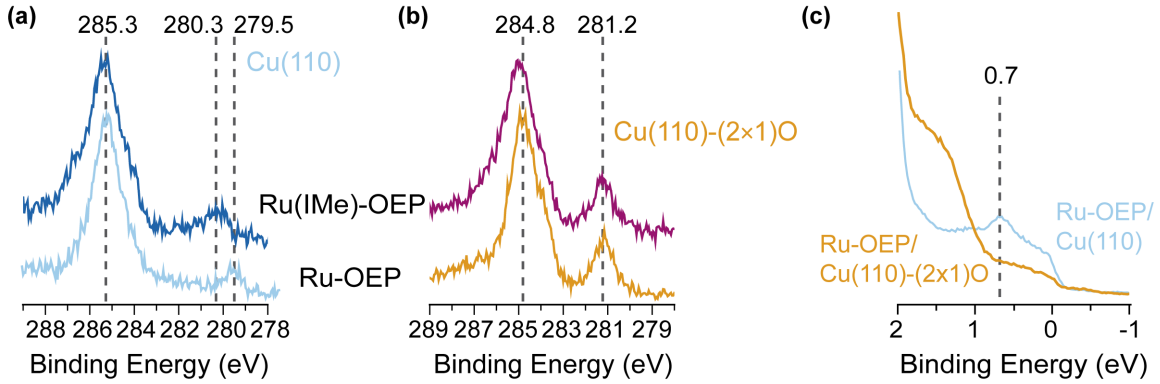

Figure 8.7: (a) XP spectra of Ru-OEP (light blue) and Ru(IMe)-OEP (dark blue) on Cu(110) and (b) XP spectra of Ru-OEP (orange) and Ru(IMe)-OEP (purple) on Cu(110)-(2×1)O. All XPS data is taken with Mg Kα radiation (hν = 1253.6 eV). (c) UP spectra of Ru-OEP on Cu(110) (light blue) and Cu(110)-(2×1)O (orange).

After dosing IMe to Ru-OEP/Cu(110)-(2×1)O, the Ru $3d_{5/2}$ peak shows no change in its position at 281.2 eV (Figure 8.7b, purple spectrum). In the C 1s region, an additional species with a higher binding energy is detected, in good accord with the carbon species of the IMe reported at a binding energy of 286.3 eV [44]. Formation of a multilayer of IMe can be excluded based on the relative increase of C 1s and the intensity of the Ru peak. The effect of the IMe binding to the Ru-OEP/Cu(110) is more striking with a shift of the Ru $3d_{5/2}$ peak by 0.8 eV to higher binding energy (Figure 8.7a, dark blue spectrum). This is ascribed to a reduction of the charge transfer to the metal center upon IMe ligation [41]. Consequentially, *trans* ligation of

strong ligands to the metalloporphyrin can result in an electronic decoupling of the metal center of a macrocycle from the substrate and thus, e.g., to a reduction of substrate induced deformation of porphyrins or phthalocyanines [49, 214, 223, 239].

Conclusion

Ru-OEP on Cu(110)-(2×1)O is stable until at least 420 K. However, at higher temperatures, surface oxygen reacts with the side chains of Ru-OEP, resulting in desorption of presumably ethylene, acetaldehyde, and water and the loss of the (2×1)O reconstruction. Overall, this system exhibits lower thermal stability compared to Ru-OEP on the bare Cu(110) substrate, where the thermal stability is only limited by inter- and intramolecular reactions of the ethyl side chains at temperatures above 500 K. However, the introduction of oxygen led to an increase in NHC binding stability of up to 130 K, surpassing the binding strengths observed on porphyrins on bare metal substrates, such as Ag(111) and Cu(110). With various analytical methods, we were able to demonstrate that the strengthening is primarily driven by the reduction in interaction with the substrate. This is a direct consequence of the *trans* effect resulting from the diminished interaction of the substrate with the ruthenium center and the *trans* positioned IMe. This study proceeds the fundamental understanding for future 3D nanoarchitectures. For instance, a functionalization of the linker molecules by a second carbene group in opposite direction to the first one could allow the formation of a well-ordered second layer of porphyrins at RT and above guided by the linker molecules [40].

9 Summary and Conclusions

This thesis discussed different approaches to obtain 3D architectures and crucial steps in their formations.

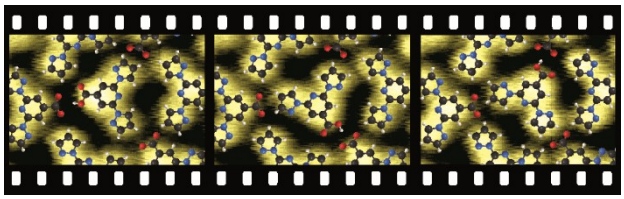

In Chapter 4, we described a system of bpp-COOH rotors in a host network formed by the deprotonated species. The kagome network cavity accommodates these rotors. In temperature-dependent STM investigations, distinct anchoring orientations of the guest were observed, transitioning with a thermal barrier of 0.95 eV. Hydrogen bonding between the guest and the host transiently stabilizes the rotating guest. DFT analyses elucidate the intricate rotation of the guest and how the energy landscape is shaped by the formation and cleavage of hydrogen bonds. The guest's enantiodirected, dynamic anchoring is explainable by the combination of the influences of the molecular kagome network and the Ag(111) substrate on the rotor molecules. The spontaneous creation of this host–guest assembly, as detailed in this study, serves as a model system for exploring intricate, dynamic, and enantiospecific interactions in confined spaces. These insights could contribute to the design of enantioselective heterogeneous catalysts. Additionally, we anticipate that organized large-scale networks with embedded individual switching units may hold promise as components for the development of molecular nanodevices.

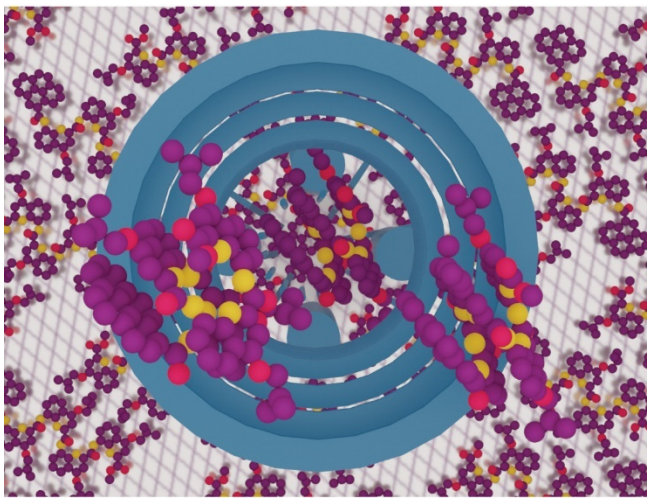

In Chapter 5, we applied a new method, electrospray controlled ion beam deposition, to deposit intact, helical foldamer molecules on an Ag(111) substrate in UHV. Unfortunately, this led to the loss of their secondary structures and formation of only a 2D self-assembly. We hypothesized that this could be attributed to either a robust interaction with the substrate in UHV conditions or the deposition energy. Consequently, a more in-depth investigation into substrate interactions is imperative. To address this issue, we propose adopting the passivated surface approach, a method employed in the subsequent chapter of this thesis, with e.g. Cu(110)-(2×1)O. This change in substrate is anticipated to mitigate interactions between the molecules and the substrate. However, modification of the foldamers' pedestal will be probably needed to

enhance their affinity with the substrate to form RT stable self-assemblies. Another avenue worth exploring is the potential reduction of deposition energy, which could prove to be a pivotal step in maintaining the secondary structure of the foldamers. A key step is to improve spraying conditions and, through this, increase the intensity of the ion beam. This will partially compensate for the effect of the reduction of the landing energy of the foldamers to the deposition timespan. For this, individual steps of the spraying process have to be explored. For instance, an experimental investigation of the *Rayleigh* limit, describing the maximal charge on single molecules during electrospray, was already started but is beyond the scope of this thesis.

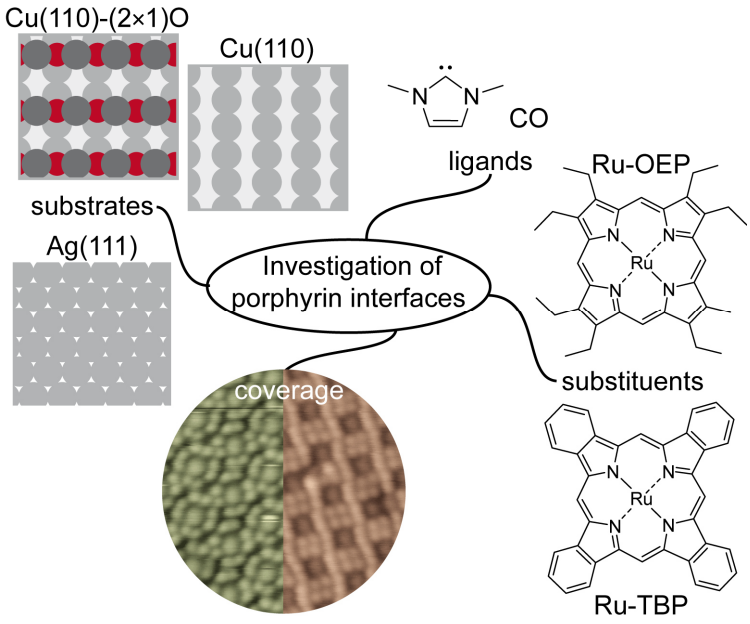

The third segment of this thesis focused on utilizing porphyrins as pedestals for carbene molecules to build 3D architectures. Our investigation delved into various factors influencing the binding strength of ligands to the metal center, including the impact of macrocycle substituents, porphyrins' coverages, and the substrate. We showed that the porphyrin substituents have a direct effect on the binding strength as IMe is stronger bonded to Ru-TBP compared to Ru-OEP. Notably, we implemented further a strategy to reinforce even more the carbene bond by minimizing interactions with the metal substrate, by changing the substrate to the Cu(110)-(2×1)O reconstructed surface. However, our observations revealed a dynamic movement of the carbene away from the surface normal, potentially detrimental to 3D MOFs. Addressing this issue necessitates a reduction in carbene dynamics, a challenge that might be tackled by inducing a strong deformation in the porphyrin macrocycle, such as adopting a saddle shape conformation as in tetraphenyl porphyrin. This conformation could limit the freedom of movement of the adsorbed carbene. Another idea is to increase the bulkiness of the carbene, thus making movement sterically hindered. NEXAFS measurements could provide valuable insights into the suppression of an angle to the surface normal for these approaches. Despite these challenges, the functional group of carbenes demonstrated robust binding to the centers, rendering them valuable linker molecules. The logical progression involves introducing new linker molecules with dual functional groups on opposing sides. This advancement could facilitate the organized growth of a second porphyrin

layer atop of the linker molecules, thereby surpassing limitations in 2D self-assemblies under UHV conditions.

Enhancing the thermal stability of the Ru-OEP/Cu(110)-(2×1)O interface emerges as a key objective. Utilizing Ru-TBP or Ru-TPP molecules, previously demonstrated on the Ag(111) substrate, could achieve this by preventing reactions with oxygen, owing to the enhanced stability of the phenyl rings over the ethyl groups. Potential strategies include the deposition of a Ru-TBP precursor or a hot deposition of Ru-OEP on the Cu(110) substrate, followed by the formation of the (2×1) reconstruction through oxygen exposure beneath the porphyrin. This heightened thermal stability would facilitate more intricate TPD studies, enhancing our understanding of IMe desorption. Such research into the desorption and binding of exemplary ligands for reaction educts and products to single metal atoms contributes significantly to advance, e.g., the understanding of single-atom catalysis – an evolving field aimed at reducing the reliance on precious metals in catalysis, aligning with the imperative goal of improving metal utilization efficiency in green catalysis challenges ahead [271-274].

Bibliography

[1] Fujita, M., Metal-directed self-assembly of two- and three-dimensional synthetic receptors. *Chem. Soc. Rev.* **1998**, *27* (6), 417-425.

[2] Love, J. C.; Estroff, L. A.; Kriebel, J. K.; Nuzzo, R. G.; Whitesides, G. M., Self-Assembled Monolayers of Thiolates on Metals as a Form of Nanotechnology. *Chem. Rev.* **2005**, *105* (4), 1103-1170.

[3] Zhou, H.-C.; Long, J. R.; Yaghi, O. M., Introduction to Metal–Organic Frameworks. *Chem. Rev.* **2012**, *112* (2), 673-674.

[4] Lehn, J.-M., Perspectives in Chemistry—Steps towards Complex Matter. *Angew. Chem. Int. Ed.* **2013**, *52* (10), 2836-2850.

[5] Ahmad, S.; Liu, J.; Ji, W.; Sun, L., Metal–Organic Framework Thin Film-Based Dye Sensitized Solar Cells with Enhanced Photocurrent. *Materials* **2018**, *11* (10), 1868.

[6] Chen, X.; Zhang, K.; Hassan, Z. M.; Redel, E.; Baumgart, H., Charge. transport, conductivity and Seebeck coefficient in pristine and TCNQ loaded preferentially grown metal-organic framework films. *J. Phys. Condens. Matter* **2022**, *34* (40), 404001.

[7] Lin, Y.; Li, W.-H.; Wen, Y.; Wang, G.-E.; Ye, X.-L.; Xu, G., Layer-by-Layer Growth of Preferred-Oriented MOF Thin Film on Nanowire Array for High-Performance Chemiresistive Sensing. *Angew. Chem. Int. Ed.* **2021**, *60* (49), 25758-25761.

[8] Yao, M.-S.; Lv, X.-J.; Fu, Z.-H.; Li, W.-H.; Deng, W.-H.; Wu, G.-D.; Xu, G., Layer-by-Layer Assembled Conductive Metal–Organic Framework Nanofilms for Room-Temperature Chemiresistive Sensing. *Angew. Chem. Int. Ed.* **2017**, *56* (52), 16510-16514.

[9] Kanj, A. B.; Verma, R.; Liu, M.; Helfferich, J.; Wenzel, W.; Heinke, L., Bunching and Immobilization of Ionic Liquids in Nanoporous Metal–Organic Framework. *Nano Lett.* **2019**, *19* (3), 2114-2120.

[10] Haldar, R.; Sen, B.; Hurrle, S.; Kitao, T.; Sankhla, R.; Kühl, B.; Welle, A.; Heissler, S.; Brenner-Weiß, G.; Thissen, P.; Uemura, T.; Gliemann, H.; Barner-Kowollik, C.; Wöll, C., Oxidative polymerization of terthiophene and a substituted thiophene monomer in metal-organic framework thin films. *Eur. Polym. J.* **2018**, *109*, 162-168.

[11] Li, W.; Xue, S.; Watzele, S.; Hou, S.; Fichtner, J.; Semrau, A. L.; Zhou, L.; Welle, A.; Bandarenka, A. S.; Fischer, R. A., Advanced Bifunctional Oxygen Reduction and Evolution Electrocatalyst Derived from Surface-Mounted Metal–Organic Frameworks. *Angew. Chem. Int. Ed.* **2020**, *59* (14), 5837-5843.

[12] Li, W.; Watzele, S.; El-Sayed, H. A.; Liang, Y.; Kieslich, G.; Bandarenka, A. S.; Rodewald, K.; Rieger, B.; Fischer, R. A., Unprecedented High Oxygen Evolution Activity of Electrocatalysts Derived from Surface-Mounted Metal–Organic Frameworks. *J. Am. Chem. Soc.* **2019**, *141* (14), 5926-5933.

[13] Gu, C.; Zhang, H.; You, P.; Zhang, Q.; Luo, G.; Shen, Q.; Wang, Z.; Hu, J., Giant and Multistage Nonlinear Optical Response in Porphyrin-Based Surface-Supported Metal–Organic Framework Nanofilms. *Nano Lett.* **2019**, *19* (12), 9095-9101.

[14] Santos, J. C. C.; Pramudya, Y.; Krstić, M.; Chen, D.-H.; Neumeier, B. L.; Feldmann, C.; Wenzel, W.; Redel, E., Halogenated Terephthalic Acid “Antenna Effects” in Lanthanide-SURMOF Thin Films. *ACS Appl. Mater. Interfaces* **2020**, *12* (46), 52166-52174.

[15] Liu, J.; Redel, E.; Walheim, S.; Wang, Z.; Oberst, V.; Liu, J.; Heissler, S.; Welle, A.; Moosmann, M.; Scherer, T.; Bruns, M.; Gliemann, H.; Wöll, C., Monolithic High Performance Surface Anchored Metal−Organic Framework Bragg Reflector for Optical Sensing. *Chem. Mater.* **2015**, *27* (6), 1991-1996.

[16] Streit, H. C.; Adlung, M.; Shekhah, O.; Stammer, X.; Arslan, H. K.; Zybaylo, O.; Ladnorg, T.; Gliemann, H.; Franzreb, M.; Wöll, C.; Wickleder, C., Surface-Anchored MOF-Based Photonic Antennae. *ChemPhysChem* **2012**, *13* (11), 2699-2702.

[17] Valadez Sánchez, E. P.; Knebel, A.; Izquierdo Sánchez, L.; Klumpp, M.; Wöll, C.; Dittmeyer, R., Studying ZIF-8 SURMOF Thin Films with a Langatate Crystal Microbalance: Single-Component Gas Adsorption Isotherms Measured at Elevated Temperatures and Pressures. *Langmuir* **2020**, *36* (29), 8444-8450.

[18] Zvyagina, A. I.; Shiryaev, A. A.; Baranchikov, A. E.; Chernyshev, V. V.; Enakieva, Y. Y.; Raitman, O. A.; Ezhov, A. A.; Meshkov, I. N.; Grishanov, D. A.; Ivanova, O. S.; Gorbunova, Y. G.; Arslanov, V. V.; Kalinina, M. A., Layer-by-layer assembly of porphyrin-based metal–organic frameworks on solids decorated with graphene oxide. *New J. Chem.* **2017**, *41* (3), 948-957.

[19] Bétard, A.; Fischer, R. A., Metal–Organic Framework Thin Films: From Fundamentals to Applications. *Chem. Rev.* **2012**, *112* (2), 1055-1083.

[20] Biswas, A.; Bayer, I. S.; Biris, A. S.; Wang, T.; Dervishi, E.; Faupel, F., Advances in top–down and bottom–up surface nanofabrication: Techniques, applications & future prospects. *Adv. Colloid Interface Sci.* **2012**, *170* (1), 2-27.

[21] Shekhah, O.; Wang, H.; Kowarik, S.; Schreiber, F.; Paulus, M.; Tolan, M.; Sternemann, C.; Evers, F.; Zacher, D.; Fischer, R. A.; Wöll, C., Step-by-Step Route for the Synthesis of Metal−Organic Frameworks. *J. Am. Chem. Soc.* **2007**, *129* (49), 15118-15119.

[22] Makiura, R.; Motoyama, S.; Umemura, Y.; Yamanaka, H.; Sakata, O.; Kitagawa, H., Surface nano-architecture of a metal–organic framework. *Nat. Mater.* **2010**, *9* (7), 565-571.

[23] Chen, D.-H.; Gliemann, H.; Wöll, C., Layer-by-layer assembly of metal-organic framework thin films: Fabrication and advanced applications. *Chem. Phys. Rev.* **2023**, *4* (1), 011305.

[24] Stepanow, S.; Lingenfelder, M.; Dmitriev, A.; Spillmann, H.; Delvigne, E.; Lin, N.; Deng, X.; Cai, C.; Barth, J. V.; Kern, K., Steering molecular organization and host–guest interactions using two-dimensional nanoporous coordination systems. *Nat. Mater.* **2004**, *3* (4), 229-233.

[25] Mena-Osteritz, E.; Bäuerle, P., Complexation of C_{60} on a Cyclothiophene Monolayer Template. *Adv. Mater.* **2006**, *18* (4), 447-451.

[26] Blunt, M. O.; Russell, J. C.; Gimenez-Lopez, M. d. C.; Taleb, N.; Lin, X.; Schröder, M.; Champness, N. R.; Beton, P. H., Guest-induced growth of a surface-based supramolecular bilayer. *Nat. Chem.* **2011**, *3* (1), 74-78.

[27] Cui, D.; Ebrahimi, M.; Rosei, F.; Macleod, J. M., Control of Fullerene Crystallization from 2D to 3D through Combined Solvent and Template Effects. *J. Am. Chem. Soc.* **2017**, *139* (46), 16732-16740.

[28] Ciesielski, A.; Cadeddu, A.; Palma, C.-A.; Gorczyński, A.; Patroniak, V.; Cecchini, M.; Samorì, P., Self-templating 2D supramolecular networks: a new avenue to reach control over a bilayer formation. *Nanoscale* **2011**, *3* (10), 4125-4129.

[29] Serrano, G.; Wiespointner-Baumgarthuber, S.; Tebi, S.; Klyatskaya, S.; Ruben, M.; Koch, R.; Müllegger, S., Bilayer of Terbium Double-Decker Single-Molecule Magnets. *J. Phys. Chem. C* **2016**, *120* (25), 13581-13586.

[30] Dawson, S. J.; Mészáros, Á.; Pethő, L.; Colombo, C.; Csékei, M.; Kotschy, A.; Huc, I., Controlling Helix Handedness in Water-Soluble Quinoline Oligoamide Foldamers. *Eur. J. Org. Chem.* **2014**, *2014* (20), 4265-4275.

[31] Devaux, F.; Li, X.; Sluysmans, D.; Maurizot, V.; Bakalis, E.; Zerbetto, F.; Huc, I.; Duwez, A.-S., Single-molecule mechanics of synthetic aromatic amide helices: Ultrafast and robust non-dissipative winding. *Chem* **2021**, *7* (5), 1333-1346.

[32] Rauschenbach, S.; Stadler, F. L.; Lunedei, E.; Malinowski, N.; Koltsov, S.; Costantini, G.; Kern, K., Electrospray Ion Beam Deposition of Clusters and Biomolecules. *Small* **2006**, *2* (4), 540-547.

[33] Peng, W.-P.; Goodwin, M. P.; Nie, Z.; Volný, M.; Ouyang, Z.; Cooks, R. G., Ion Soft Landing Using a Rectilinear Ion Trap Mass Spectrometer. *Anal. Chem.* **2008**, *80* (17), 6640-6649.

[34] Walz, A., Compact and versatile electrospray - controlled ion beam deposition with adjustable frequency RF ion guides and extended mass range. Physics Department, E20, Ph.D. Thesis (Technical University of Munich, Garching, 2020).

[35] Walz, A.; Stoiber, K.; Huettig, A.; Schlichting, H.; Barth, J. V., Navigate Flying Molecular Elephants Safely to the Ground: Mass-Selective Soft Landing up to the Mega-Dalton Range by Electrospray Controlled Ion-Beam Deposition. *Anal. Chem.* **2022**, *94* (22), 7767-7778.

[36] Ran, W.; Walz, A.; Stoiber, K.; Knecht, P.; Xu, H.; Papageorgiou, A. C.; Huettig, A.; Cortizo-Lacalle, D.; Mora-Fuentes, J. P.; Mateo-Alonso, A.; Schlichting, H.; Reichert, J.; Barth, J. V., Depositing Molecular Graphene Nanoribbons on Ag(111) by Electrospray Controlled Ion Beam Deposition: Self-Assembly and On-Surface Transformations. *Angew. Chem. Int. Ed.* **2022**, *61* (14), e202111816.

[37] Wang, Z.; Qian, K.; Öner, M. A.; Deimel, P. S.; Wang, Y.; Zhang, S.; Zhang, X.; Gupta, V.; Li, J.; Gao, H. J.; Duncan, D. A.; Barth, J. V.; Lin, X.; Allegretti, F.; Du, S.; Palma, C. A., Layer-by-Layer Epitaxy of Porphyrin–Ligand Fe(II)-Fe(III) Nanoarchitectures for Advanced Metal–Organic Framework Growth. *ACS Appl. Nano Mater.* **2020**, *3*, 11752.

[38] Gottfried, J. M., Surface Chemistry of Porphyrins and Phthalocyanines. *Surf. Sci. Rep.* **2015**, *70* (3), 259-379.

[39] Auwärter, W.; Écija, D.; Klappenberger, F.; Barth, J. V., Porphyrins at Interfaces. *Nat. Chem.* **2015**, *7*, 105-120.

[40] Orbelli Biroli, A.; Calloni, A.; Bossi, A.; Jagadeesh, M. S.; Albani, G.; Duò, L.; Ciccacci, F.; Goldoni, A.; Verdini, A.; Schio, L.; Floreano, L.; Bussetti, G., Out-Of-Plane Metal Coordination for a True Solvent-Free Building with Molecular Bricks: Dodging the Surface Ligand Effect for On-Surface Vacuum Self-Assembly. *Adv. Funct. Mater.* **2021**, *31* (20), 2011008.

[41] Knecht, P.; Zhang, B.; Reichert, J.; Duncan, D. A.; Schwarz, M.; Haag, F.; Ryan, P. T. P.; Lee, T.-L.; Deimel, P. S.; Feulner, P.; Allegretti, F.; Auwärter, W.; Médard, G.; Seitsonen, A. P.; Barth, J. V.; Papageorgiou, A. C., Assembly and Manipulation of a Prototypical N-Heterocyclic Carbene with a Metalloporphyrin Pedestal on a Solid Surface. *J. Am. Chem. Soc.* **2021**, *143* (11), 4433-4439.

[42] Knecht, P.; Meier, D.; Reichert, J.; Duncan, D. A.; Schwarz, M.; Küchle, J. T.; Lee, T.-L.; Deimel, P. S.; Feulner, P.; Allegretti, F.; Auwärter, W.; Médard, G.; Seitsonen, A. P.; Barth, J. V.; Papageorgiou, A. C., N-Heterocyclic Carbenes: Molecular Porters of Surface Mounted Ru-Porphyrins. *Angew. Chem. Int. Ed.* **2022**, *61* (49), e202211877.

[43] Hopkinson, M. N.; Richter, C.; Schedler, M.; Glorius, F., An Overview of N-Heterocyclic Carbenes. *Nature* **2014**, *510* (7506), 485-496.

[44] Jiang, L.; Zhang, B.; Médard, G.; Seitsonen, A. P.; Haag, F.; Allegretti, F.; Reichert, J.; Kuster, B.; Barth, J. V.; Papageorgiou, A. C., N-Heterocyclic carbenes on close-packed coinage metal surfaces: bis-carbene metal adatom bonding scheme of monolayer films on Au, Ag and Cu. *Chem. Sci.* **2017**, *8* (12), 8301-8308.

[45] Wang, G.; Rühling, A.; Amirjalayer, S.; Knor, M.; Ernst, J. B.; Richter, C.; Gao, H. J.; Timmer, A.; Gao, H. Y.; Doltsinis, N. L.; Glorius, F.; Fuchs, H., Ballbot-Type Motion of N-Heterocyclic Carbenes on Gold Surfaces. *Nat. Chem.* **2017**, *9*, 152-156.

[46] Larrea, C. R.; Baddeley, C. J.; Narouz, M. R.; Mosey, N. J.; Horton, J. H.; Crudden, C. M., N-Heterocyclic Carbene Self-Assembled Monolayers on Copper and Gold: Dramatic Effect of Wingtip Groups on Binding, Orientation and Assembly. *ChemPhysChem* **2017**, *18* (24), 3536-3539.

[47] Inayeh, A.; Groome, R. R. K.; Singh, I.; Veinot, A. J.; de Lima, F. C.; Miwa, R. H.; Crudden, C. M.; McLean, A. B., Self-assembly of N-heterocyclic carbenes on Au(111). *Nat. Commun.* **2021**, *12* (1), 4034.

[48] Ren, J.; Freitag, M.; Gao, Y.; Bellotti, P.; Das, M.; Schulze Lammers, B.; Monig, H.; Zhang, Y.; Daniliuc, C. G.; Du, S.; Fuchs, H.; Glorius, F., Reversible Self-Assembly of an N-Heterocyclic Carbene on Metal Surfaces. *Angew. Chem. Int. Ed.* **2022**, *61* (13), e202115104.

[49] Deimel, P. S.; Bababrik, R. M.; Wang, B.; Blowey, P. J.; Rochford, L. A.; Thakur, P. K.; Lee, T. L.; Bocquet, M. L.; Barth, J. V.; Woodruff, D. P.; Duncan, D. A.; Allegretti, F., Direct quantitative identification of the “surface *trans*-effect”. *Chem. Sci.* **2016**, *7* (9), 5647-5656

[50] Hieringer, W.; Flechtner, K.; Kretschmann, A.; Seufert, K.; Auwärter, W.; Barth, J. V.; Görling, A.; Steinrück, H. P.; Gottfried, J. M., The Surface Trans Effect: Influence of Axial Ligands on the Surface Chemical Bonds of Adsorbed Metalloporphyrins. *J. Am. Chem. Soc.* **2011**, *133* (16), 6206-6222.

[51] Flechtner, K.; Kretschmann, A.; Steinrück, H.-P.; Gottfried, J. M., NO-Induced Reversible Switching of the Electronic Interaction between a Porphyrin-Coordinated Cobalt Ion and a Silver Surface. *J. Am. Chem. Soc.* **2007**, *129* (40), 12110-12111.

[52] Seufert, K.; Auwärter, W.; Barth, J. V., Discriminative Response of Surface-Confined Metalloporphyrin Molecules to Carbon and Nitrogen Monoxide. *J. Am. Chem. Soc.* **2010**, *132* (51), 18141-18146.

[53] Fenn, J. B.; Mann, M.; Meng, C. K.; Wong, S. F.; Whitehouse, C. M., Electrospray Ionization for Mass Spectrometry of Large Biomolecules. *Science* **1989**, *246* (4926), 64-71.

[54] The Nobel Prize in Chemistry 2002. NobelPrize.org. Nobel Prize Outreach AB 2024. https://www.nobelprize.org/prizes/chemistry/2002/summary/ Fri. 12 Jan 2024.

[55] Konermann, L.; Ahadi, E.; Rodriguez, A. D.; Vahidi, S., Unraveling the Mechanism of Electrospray Ionization. *Anal. Chem.* **2013**, *85* (1), 2-9.

[56] Fenn, J. B., Electrospray Wings for Molecular Elephants (Nobel Lecture). *Angew. Chem. Int. Ed.* **2003**, *42* (33), 3871-3894.

[57] Wu, X.; Oleschuk, R. D.; Cann, N. M., Characterization of microstructured fibre emitters: in pursuit of improved nano electrospray ionization performance. *Analyst* **2012**, *137* (18), 4150-4161.

[58] Taylor, G. I., Disintegration of water drops in an electric field. *Proc. R. Soc. Lond. A* **1964**, *280* (1382), 383-397.

[59] Duft, D.; Achtzehn, T.; Müller, R.; Huber, B. A.; Leisner, T., Rayleigh jets from levitated microdroplets. *Nature* **2003**, *421* (6919), 128-128.

[60] Rayleigh, L., On the equilibrium of liquid conducting masses charged with electricity. *Lond. Edinb. Dublin Philos. Mag. J. Sci.* **1882**, *14* (87), 184-186.

[61] Tersoff, J.; Hamann, D. R., Theory of the scanning tunneling microscope. *Phys. Rev. B* **1985**, *31* (2), 805-813.

[62] Binnig, G.; Rohrer, H.; Gerber, C.; Weibel, E., Surface Studies by Scanning Tunneling Microscopy. *Phys. Rev. Lett.* **1982**, *49* (1), 57-61.

[63] Binnig, G.; Rohrer, H., Scanning tunneling microscopy-from birth to adolescence. *Rev. Mod. Phys.* **1987**, *59* (3), 615-625.

[64] The Nobel Prize in Physics 1986. NobelPrize.org. Nobel Prize Outreach AB 2023. https://www.nobelprize.org/prizes/physics/1986/summary/ Fri. 9 Jun 2023.

[65] Voigtländer, B., *Scanning probe microscopy: Atomic force microscopy and scanning tunneling microscopy*. Springer: Berlin, 2015.

[66] Tersoff, J.; Hamann, D. R., Theory and Application for the Scanning Tunneling Microscope. *Phys. Rev. Lett.* **1983**, *50* (25), 1998-2001.

[67] Bardeen, J., Tunnelling from a Many-Particle Point of View. *Phys. Rev. Lett.* **1961**, *6* (2), 57-59.

[68] Hansma, P. K.; Tersoff, J., Scanning tunneling microscopy. *J. Appl. Phys.* **1987**, *61* (2), R1-R24.

[69] Fang, F.; Ju, B., Scanning Tunneling Microscope. In *CIRP Encyclopedia of Production Engineering*, The International Academy for, P.; Laperrière, L.; Reinhart, G., Eds. Springer Berlin Heidelberg: Berlin, Heidelberg, 2016; pp 1-4.

[70] Hertz, H., Ueber einen Einfluss des ultravioletten Lichtes auf die electrische Entladung. *Ann. Phys. (Leipzig)* **1887**, *267* (8), 983-1000.

[71] Einstein, A., Über einen die Erzeugung und Verwandlung des Lichtes betreffenden heuristischen Gesichtspunkt. *Ann. Phys. (Leipzig)* **1905**, *322* (6), 132-148.

[72] The Nobel Prize in Physics 1921. NobelPrize.org. Nobel Prize Outreach AB 2023. https://www.nobelprize.org/prizes/physics/1921/summary/ Fri. 9 Jun 2023.

[73] Kai M. Siegbahn – Facts. NobelPrize.org. Nobel Prize Outreach AB 2024. https://www.nobelprize.org/prizes/physics/1981/siegbahn/facts/ Sun. 21 Jan 2024.

[74] Hüfner, S., *Photoelectron Spectroscopy: Principles and Applications*. Springer Science & Business Media: 2003.

[75] Huchital, D. A.; McKeon, R. T., Use of an Electron Flood Gun to Reduce Surface Charging in X-Ray Photoelectron Spectroscopy. *Appl. Phys. Lett.* **2003**, *20* (4), 158-159.

[76] Chastain, J.; King Jr, R. C., Handbook of X-ray photoelectron spectroscopy. *Perkin-Elmer Corporation* **1992**, *40*, 114.

[77] Stöhr, J.; Outka, D. A., Determination of molecular orientations on surfaces from the angular dependence of near-edge x-ray-absorption fine-structure spectra. *Phys. Rev. B* **1987**, *36* (15), 7891-7905.

[78] Stöhr, J.; Baberschke, K.; Jaeger, R.; Treichler, R.; Brennan, S., Orientation of Chemisorbed Molecules from Surface-Absorption Fine-Structure Measurements: CO and NO on Ni(100). *Phys. Rev. Lett.* **1981**, *47* (5), 381-384.

[79] Stöhr, J.; Jaeger, R., Absorption-edge resonances, core-hole screening, and orientation of chemisorbed molecules: CO, NO, and N_2 on Ni(100). *Phys. Rev. B* **1982**, *26* (8), 4111-4131.

[80] Outka, D. A.; Stöhr, J., Curve fitting analysis of near-edge core excitation spectra of free, adsorbed, and polymeric molecules. *J. Chem. Phys.* **1988**, *88* (6), 3539-3554.

[81] Woodruff, D. P., Surface structure determination using x-ray standing waves. *Rep. Prog. Phys.* **2005**, *68* (4), 743-798.

[82] Batterman, B. W.; Cole, H., Dynamical Diffraction of X Rays by Perfect Crystals. *Rev. Mod. Phys.* **1964**, *36* (3), 681-717.

[83] Knecht, P., Transition Metal Centers Embedded in Surface-Confined Coordination Environments: Tunable Interfaces and N-Heterocyclic Carbene Nanoarchitectures. Physics Department, E20, Ph.D. Thesis (Technical University of Munich, Garching, 2021).

[84] Batterman, B. W., Detection of Foreign Atom Sites by Their X-Ray Fluorescence Scattering. *Phys. Rev. Lett.* **1969**, *22* (14), 703-705.

[85] Woodruff, D. P.; Duncan, D. A., X-Ray Standing Wave Studies of Molecular Adsorption: Why Coherent Fractions Matter. *New J. Phys.* **2020**, *22*, 113012.

[86] Oura, K.; Katayama, M.; Zotov, A. V.; Lifshits, V. G.; Saranin, A. A., Elementary processes at surfaces I: adsorption and desorption. In *Surface Science: An Introduction*, 2003; pp 295-323.

[87] King, D. A., Thermal desorption from metal surfaces: A review. *Surf. Sci.* **1975**, *47* (1), 384-402.

[88] Estrup, P. J.; Greene, E. F.; Cardillo, M. J.; Tully, J. C., Influence of surface phase transitions on desorption kinetics: the compensation effect. *J. Phys. Chem.* **1986**, *90* (17), 4099-4104.

[89] Lee, S. B.; Weiss, M.; Ertl, G., Adsorption of potassium on iron. *Surf. Sci.* **1981**, *108* (2), 357-367.

[90] Albano, E. V., Thermal desorption mass spectrometry of alkali metal atoms from transition metal surfaces. The influence of coadsorbed oxygen. *J. Chem. Phys.* **1986**, *85* (2), 1044-1051.

[91] Davisson, C.; Germer, L. H., Diffraction of electrons by a crystal of nickel. *Phys. Rev.* **1927**, *30* (6), 705.

[92] The Nobel Prize in Physics 1937. NobelPrize.org. Nobel Prize Outreach AB 2024. https://www.nobelprize.org/prizes/physics/1937/summary/ Sun. 14 Jan 2024.

[93] Conrad, E.; Unertl, W., Diffraction methods. *Handbook of surface science* **1996**, *1*, 271-360.

[94] Ladislas Wiza, J., Microchannel plate detectors. *Nucl. Instrum. Methods* **1979**, *162* (1), 587-601.

[95] Krumbein, L.; Anggara, K.; Stella, M.; Michnowicz, T.; Ochner, H.; Abb, S.; Rinke, G.; Portz, A.; Dürr, M.; Schlickum, U.; Baldwin, A.; Floris, A.; Kern, K.; Rauschenbach, S., Fast Molecular Compression by a Hyperthermal Collision Gives Bond-Selective Mechanochemistry. *Phys. Rev. Lett.* **2021**, *126* (5), 056001.

[96] Pauly, M.; Sroka, M.; Reiss, J.; Rinke, G.; Albarghash, A.; Vogelgesang, R.; Hahne, H.; Kuster, B.; Sesterhenn, J.; Kern, K.; Rauschenbach, S., A hydrodynamically optimized nano-electrospray ionization source and vacuum interface. *Analyst* **2014**, *139* (8), 1856-1867.

[97] Feulner, P.; Menzel, D., Simple Ways to Improve ''Flash Desorption'' Measurements from Single Crystal Surfaces. *J. Vac. Sci. Technol.* **1980**, *17* (2), 662.

[98] Haag, F. M., Atomic Level Studies of the Surface-Directed Synthesis of Novel Organometallic and Metal-Organic Two-Dimensional Assemblies. Physics Department, E20, Ph.D. Thesis (Technical University of Munich, Garching, 2022).

[99] Cao, N., On-Surface Synthesis of Covalent-Bonded Molecular Nanostructures: Reaction Strategies and Refined Control. Physics Department, E20, Ph.D. Thesis (Technical University of Munich, Garching, 2022).

[100] Oberta, P.; Flechsig, U.; Muntwiler, M.; Quitmann, C., Optical design study of the PEARL beamline at SLS. *Nucl. Instrum. Methods Phys. Res. A* **2011**, *635* (1), 116-120.

[101] Muntwiler, M.; Zhang, J.; Stania, R.; Matsui, F.; Oberta, P.; Flechsig, U.; Patthey, L.; Quitmann, C.; Glatzel, T.; Widmer, R.; Meyer, E.; Jung, T. A.; Aebi, P.; Fasel, R.; Greber, T., Surface science at the PEARL beamline of the Swiss Light Source. *J. Synchrotron Radiat.* **2017**, *24* (1), 354-366.

[102] Lee, T. L.; Duncan, D. A., A Two-Color Beamline for Electron Spectroscopies at Diamond Light Source. *Synchrotron Radiat. News* **2018**, *31* (4), 16.

[103] Preobrajenski, A.; Generalov, A.; Öhrwall, G.; Tchaplyguine, M.; Tarawneh, H.; Appelfeller, S.; Frampton, E.; Walsh, N., FlexPES: a versatile soft X-ray beamline at MAX IV Laboratory. *J. Synchrotron Radiat.* **2023**, *30* (Pt 4), 831-840.

[104] Meier, D.; Adak, A. K.; Knecht, P.; Reichert, J.; Mondal, S.; Suryadevara, N.; Kuppusamy, S. K.; Eguchi, K.; Muntwiler, M. K.; Allegretti, F.; Ruben, M.; Barth, J. V.; Narasimhan, S.; Papageorgiou, A. C., Rotation in an Enantiospecific Self-Assembled Array of Molecular Raffle Wheels. *Angew. Chem. Int. Ed.* **2021**, *60* (52), 26932-26938.

[105] Qi, T.; Deschrijver, T.; Huc, I., Large-scale and chromatography-free synthesis of an octameric quinoline-based aromatic amide helical foldamer. *Nat. Protoc.* **2013**, *8* (4), 693-708.

[106] Li, X.; Markandeya, N.; Jonusauskas, G.; McClenaghan, N. D.; Maurizot, V.; Denisov, S. A.; Huc, I., Photoinduced Electron Transfer and Hole Migration in Nanosized Helical Aromatic Oligoamide Foldamers. *J. Am. Chem. Soc.* **2016**, *138* (41), 13568-13578.

[107] Delsuc, N.; Kawanami, T.; Lefeuvre, J.; Shundo, A.; Ihara, H.; Takafuji, M.; Huc, I., Kinetics of Helix-Handedness Inversion: Folding and Unfolding in Aromatic Amide Oligomers. *ChemPhysChem* **2008**, *9* (13), 1882-1890.

[108] Wang, J.; Wicher, B.; Méndez-Ardoy, A.; Li, X.; Pecastaings, G.; Buffeteau, T.; Bassani, D. M.; Maurizot, V.; Huc, I., Loading Linear Arrays of CuII Inside Aromatic Amide Helices. *Angew. Chem. Int. Ed.* **2021**, *60* (34), 18461-18466.

[109] Meier, D.; Schoof, B.; Wang, J.; Li, X.; Walz, A.; Huettig, A.; Schlichting, H.; Rosu, F.; Gabelica, V.; Maurizot, V.; Reichert, J.; Papageorgiou, A. C.; Huc, I.; Barth, J. V., Structural adaptations of electrosprayed aromatic oligoamide foldamers on Ag(111). *Chem. Commun.* **2022**, *58* (64), 8938-8941.

[110] Au, C. T.; Hirsch, W.; Hirschwald, W., Adsorption of carbon monoxide and carbon dioxide on annealed and defect zinc oxide (0001) surfaces studied by photoelectron spectroscopy (XPS and UPS). *Surf. Sci.* **1988**, *197* (3), 391-401.

[111] Cirera, B.; Giménez-Agulló, N.; Björk, J.; Martínez-Peña, F.; Martin-Jimenez, A.; Rodriguez-Fernandez, J.; Pizarro, A. M.; Otero, R.; Gallego, J. M.; Ballester, P.; Galan-Mascaros, J. R.; Ecija, D., Thermal selectivity of intermolecular versus intramolecular reactions on surfaces. *Nat. Commun.* **2016**, *7* (1), 11002.

[112] Heinrich, B. W.; Ahmadi, G.; Müller, V. L.; Braun, L.; Pascual, J. I.; Franke, K. J., Change of the Magnetic Coupling of a Metal–Organic Complex with the Substrate by a Stepwise Ligand Reaction. *Nano Lett.* **2013**, *13* (10), 4840-4843.

[113] Williams, C. G.; Wang, M.; Skomski, D.; Tempas, C. D.; Kesmodel, L. L.; Tait, S. L., Dehydrocyclization of peripheral alkyl groups in porphyrins at Cu(100) and Ag(111) surfaces. *Surf. Sci.* **2016**, *653*, 130-137.

[114] Nečas, D.; Klapetek, P., Gwyddion: an open-source software for SPM data analysis. *Open Phys.* **2012**, *10* (1), 181-188.

[115] Riss, A., SpmImage Tycoon: Organize and analyze scanning probe microscopy data. *JOSS* **2022**, *7* (77), 4644.

[116] Giannozzi, P.; Baroni, S.; Bonini, N.; Calandra, M.; Car, R.; Cavazzoni, C.; Ceresoli, D.; Chiarotti, G. L.; Cococcioni, M.; Dabo, I.; Dal Corso, A.; de Gironcoli, S.; Fabris, S.; Fratesi, G.; Gebauer, R.; Gerstmann, U.; Gougoussis, C.; Kokalj, A.; Lazzeri, M.; Martin-Samos, L.; Marzari, N.; Mauri, F.; Mazzarello, R.; Paolini, S.; Pasquarello, A.; Paulatto, L.; Sbraccia, C.; Scandolo, S.; Sclauzero, G.; Seitsonen, A. P.; Smogunov, A.; Umari, P.; Wentzcovitch, R. M., QUANTUM ESPRESSO: a Modular and Open-Source Software Project for Quantum Simulations of Materials. *J. Phys. Condens. Matter* **2009**, *21*, 395502.

[117] Kohn, W.; Sham, L. J., Self-Consistent Equations Including Exchange and Correlation Effects. *Phys. Rev.* **1965**, *140* (4A), A1133-A1138.

[118] Vanderbilt, D., Soft self-consistent pseudopotentials in a generalized eigenvalue formalism. *Phys. Rev. B* **1990**, *41* (11), 7892-7895.

[119] Perdew, J. P.; Burke, K.; Ernzerhof, M., Generalized Gradient Approximation Made Simple. *Phys. Rev. Lett.* **1996**, *77* (18), 3865-3868.

[120] Grimme, S., Semiempirical GGA-type density functional constructed with a long-range dispersion correction. *J. Comput. Chem.* **2006**, *27* (15), 1787-1799.

[121] Marzari, N.; Vanderbilt, D.; De Vita, A.; Payne, M. C., Thermal Contraction and Disordering of the Al(110) Surface. *Phys. Rev. Lett.* **1999**, *82* (16), 3296-3299.

[122] Broyden, C. G., The convergence of a class of double-rank minimization algorithms: 2. The new algorithm. *IMA J. Appl. Math.* **1970**, *6* (3), 222-231.

[123] Fletcher, R., A new approach to variable metric algorithms. *Comput. J.* **1970**, *13* (3), 317-322.

[124] Goldfarb, D., A family of variable-metric methods derived by variational means. *Math. Comput.* **1970**, *24* (109), 23-26.

[125] Shanno, D. F., Conditioning of quasi-Newton methods for function minimization. *Math. Comput.* **1970**, *24* (111), 647-656.

[126] Feynman, R. P., Forces in molecules. *Phys. Rev.* **1939**, *56* (4), 340.

[127] Bader, R., Atoms in molecules: a quantum theory: Oxford Univ. *Press.: Oxford* **1990**.

[128] Henkelman, G.; Arnaldsson, A.; Jónsson, H., A fast and robust algorithm for Bader decomposition of charge density. *Comput. Mater. Sci.* **2006**, *36* (3), 354-360.

[129] Balzani, V.; Credi, A.; Venturi, M., Molecular Machines Working on Surfaces and at Interfaces. *ChemPhysChem* **2008**, *9* (2), 202-220.

[130] Browne, W. R.; Feringa, B. L., Making molecular machines work. *Nat. Nanotechnol.* **2006**, *1* (1), 25-35.

[131] Écija, D.; Auwärter, W.; Vijayaraghavan, S.; Seufert, K.; Bischoff, F.; Tashiro, K.; Barth, J. V., Assembly and Manipulation of Rotatable Cerium Porphyrinato Sandwich Complexes on a Surface. *Angew. Chem. Int. Ed.* **2011**, *50* (17), 3872-3877.

[132] Hla, S.-W., Molecular machines: Reinventing the wheel. *Nat. Nanotechnol.* **2007**, *2* (2), 82-84.

[133] Michl, J.; Sykes, E. C. H., Molecular Rotors and Motors: Recent Advances and Future Challenges. *ACS Nano* **2009**, *3* (5), 1042-1048.

[134] Wahl, M.; Stöhr, M.; Spillmann, H.; Jung, T. A.; Gade, L. H., Rotation-libration in a hierarchic supramolecular rotor-stator system: Arrhenius activation and retardation by local interaction. *Chem. Commun.* **2007**, (13), 1349-1351.

[135] Wintjes, N.; Bonifazi, D.; Cheng, F.; Kiebele, A.; Stöhr, M.; Jung, T.; Spillmann, H.; Diederich, F., A Supramolecular Multiposition Rotary Device. *Angew. Chem. Int. Ed.* **2007**, *46* (22), 4089-4092.

[136] Jung, T. A.; Schlittler, R. R.; Gimzewski, J. K.; Tang, H.; Joachim, C., Controlled Room-Temperature Positioning of Individual Molecules: Molecular Flexure and Motion. *Science* **1996**, *271* (5246), 181.

[137] Eichberger, M.; Marschall, M.; Reichert, J.; Weber-Bargioni, A.; Auwärter, W.; Wang, R. L. C.; Kreuzer, H. J.; Pennec, Y.; Schiffrin, A.; Barth, J. V., Dimerization Boosts One-Dimensional Mobility of Conformationally Adapted Porphyrins on a Hexagonal Surface Atomic Lattice. *Nano Lett.* **2008**, *8* (12), 4608-4613.

[138] Otero, R.; Hümmelink, F.; Sato, F.; Legoas, S. B.; Thostrup, P.; Lægsgaard, E.; Stensgaard, I.; Galvão, D. S.; Besenbacher, F., Lock-and-key effect in the surface diffusion of large organic molecules probed by STM. *Nat. Mater.* **2004**, *3* (11), 779-782.

[139] Chiaravalloti, F.; Gross, L.; Rieder, K.-H.; Stojkovic, S. M.; Gourdon, A.; Joachim, C.; Moresco, F., A rack-and-pinion device at the molecular scale. *Nat. Mater.* **2007**, *6* (1), 30-33.

[140] Makoudi, Y.; Arras, E.; Kepčija, N.; Krenner, W.; Klyatskaya, S.; Klappenberger, F.; Ruben, M.; Seitsonen, A. P.; Barth, J. V., Hierarchically Organized Bimolecular Ladder Network Exhibiting Guided One-Dimensional Diffusion. *ACS Nano* **2012**, *6* (1), 549-556.

[141] Haq, S.; Wit, B.; Sang, H.; Floris, A.; Wang, Y.; Wang, J.; Pérez-García, L.; Kantorovitch, L.; Amabilino, D. B.; Raval, R., A Small Molecule Walks Along a Surface Between Porphyrin Fences That Are Assembled In Situ. *Angew. Chem. Int. Ed.* **2015**, *54* (24), 7101-7105.

[142] de Jonge, J. J.; Ratner, M. A.; de Leeuw, S. W.; Simonis, R. O., Molecular Dipole Chains III: Energy Transfer. *J. Phys. Chem. B* **2004**, *108* (8), 2666-2675.

[143] Gao, L.; Liu, Q.; Zhang, Y. Y.; Jiang, N.; Zhang, H. G.; Cheng, Z. H.; Qiu, W. F.; Du, S. X.; Liu, Y. Q.; Hofer, W. A.; Gao, H. J., Constructing an Array of Anchored Single-Molecule Rotors on Gold Surfaces. *Phys. Rev. Lett.* **2008**, *101* (19), 197209.

[144] Bellisario, D. O.; Baber, A. E.; Tierney, H. L.; Sykes, E. C. H., Engineering Dislocation Networks for the Directed Assembly of Two-Dimensional Rotor Arrays. *J. Phys. Chem. C* **2009**, *113* (15), 5895-5898.

[145] Charra, F.; Cousty, J., Surface-Induced Chirality in a Self-Assembled Monolayer of Discotic Liquid Crystal. *Phys. Rev. Lett.* **1998**, *80* (8), 1682-1685.

[146] Kühne, D.; Klappenberger, F.; Krenner, W.; Klyatskaya, S.; Ruben, M.; Barth, J. V., Rotational and constitutional dynamics of caged supramolecules. *Proc. Natl. Acad. Sci. U.S.A.* **2010**, *107* (50), 21332-21336.

[147] Palma, C.-A.; Björk, J.; Rao, F.; Kühne, D.; Klappenberger, F.; Barth, J. V., Topological Dynamics in Supramolecular Rotors. *Nano Lett.* **2014**, *14* (8), 4461-4468.

[148] Palma, C.-A.; Björk, J.; Klappenberger, F.; Arras, E.; Kuhne, D.; Stafstrom, S.; Barth, J. V., Visualization and thermodynamic encoding of single-molecule partition function projections. *Nat. Commun.* **2015**, *6*, 6210.

[149] Lloyd, J. A.; Papageorgiou, A. C.; Fischer, S.; Oh, S. C.; Sağlam, Ö.; Diller, K.; Duncan, D. A.; Allegretti, F.; Klappenberger, F.; Stöhr, M.; Maurer, R. J.; Reuter, K.; Reichert, J.; Barth, J. V., Dynamics of Spatially Confined Bisphenol A Trimers in a Unimolecular Network on Ag(111). *Nano Lett.* **2016**, *16* (3), 1884-1889.

[150] Jing, C.; Zhang, B.; Synkule, S.; Ebrahimi, M.; Riss, A.; Auwärter, W.; Jiang, L.; Médard, G.; Reichert, J.; Barth, J. V.; Papageorgiou, A. C., Snapshots of Dynamic Adaptation: Two-Dimensional Molecular Architectonics with Linear Bis-Hydroxamic Acid Modules. *Angew. Chem. Int. Ed.* **2019**, *58* (52), 18948-18956.

[151] Jasper-Toennies, T.; Gruber, M.; Johannsen, S.; Frederiksen, T.; Garcia-Lekue, A.; Jäkel, T.; Roehricht, F.; Herges, R.; Berndt, R., Rotation of Ethoxy and Ethyl Moieties on a Molecular Platform on Au(111). *ACS Nano* **2020**, *14* (4), 3907-3916.

[152] Zhang, Y.; Kersell, H.; Stefak, R.; Echeverria, J.; Iancu, V.; Perera, U. G. E.; Li, Y.; Deshpande, A.; Braun, K. F.; Joachim, C.; Rapenne, G.; Hla, S. W., Simultaneous and coordinated rotational switching of all molecular rotors in a network. *Nat. Nanotechnol.* **2016**, *11* (8), 706-712.

[153] Merz, L.; Ernst, K.-H., Unification of the matrix notation in molecular surface science. *Surf. Sci.* **2010**, *604* (11), 1049-1054.

[154] Ecija, D.; Vijayaraghavan, S.; Auwärter, W.; Joshi, S.; Seufert, K.; Aurisicchio, C.; Bonifazi, D.; Barth, J. V., Two-Dimensional Short-Range Disordered Crystalline Networks from Flexible Molecular Modules. *ACS Nano* **2012**, *6* (5), 4258-4265.

[155] Feynman, R. P.; Leighton, R. B.; Sands, M. L., *The Feynman lectures on physics*. Addison-Wesley Pub. Co.: Reading, Mass., 1963.

[156] Fischer, S.; Papageorgiou, A. C.; Marschall, M.; Reichert, J.; Diller, K.; Klappenberger, F.; Allegretti, F.; Nefedov, A.; Wöll, C.; Barth, J. V., l-Cysteine on Ag(111): A Combined STM and X-ray Spectroscopy Study of Anchorage and Deprotonation. *J. Phys. Chem. C* **2012**, *116* (38), 20356-20362.

[157] Galadzhun, I.; Kulmaczewski, R.; Cespedes, O.; Yamada, M.; Yoshinari, N.; Konno, T.; Halcrow, M. A., 2,6-Bis(pyrazol-1-yl)pyridine-4-carboxylate Esters with Alkyl Chain Substituents and Their Iron(II) Complexes. *Inorg. Chem.* **2018**, *57* (21), 13761-13771.

[158] Xiao, W.; Ernst, K.-H.; Palotas, K.; Zhang, Y.; Bruyer, E.; Peng, L.; Greber, T.; Hofer, W. A.; Scott, L. T.; Fasel, R., Microscopic origin of chiral shape induction in achiral crystals. *Nat. Chem.* **2016**, *8* (4), 326-330.

[159] Shukla, N.; Gellman, A. J., Chiral metal surfaces for enantioselective processes. *Nat. Mater.* **2020**, *19* (9), 939-945.

[160] Bonello, J. M.; Williams, F. J.; Lambert, R. M., Aspects of Enantioselective Heterogeneous Catalysis: Structure and Reactivity of (*S*)-(−)-1-(1-Naphthyl)ethylamine on Pt{111}. *J. Am. Chem. Soc.* **2003**, *125* (9), 2723-2729.

[161] Demers-Carpentier, V.; Goubert, G.; Masini, F.; Lafleur-Lambert, R.; Dong, Y.; Lavoie, S.; Mahieu, G.; Boukouvalas, J.; Gao, H.; Rasmussen, A. M. H.; Ferrighi, L.; Pan, Y.; Hammer, B.; McBreen, P. H., Direct Observation of Molecular Preorganization for Chirality Transfer on a Catalyst Surface. *Science* **2011**, *334* (6057), 776-780.

[162] Schlickum, U.; Decker, R.; Klappenberger, F.; Zoppellaro, G.; Klyatskaya, S.; Auwärter, W.; Neppl, S.; Kern, K.; Brune, H.; Ruben, M.; Barth, J. V., Chiral Kagomé Lattice from Simple Ditopic Molecular Bricks. *J. Am. Chem. Soc.* **2008**, *130* (35), 11778-11782.

[163] Chen, T.; Chen, Q.; Zhang, X.; Wang, D.; Wan, L.-J., Chiral Kagome Network from Thiacalix[4]arene Tetrasulfonate at the Interface of Aqueous Solution/Au(111) Surface: An in Situ Electrochemical Scanning Tunneling Microscopy Study. *J. Am. Chem. Soc.* **2010**, *132* (16), 5598-5599.

[164] Wang, T.; Fan, Q.; Feng, L.; Tao, Z.; Huang, J.; Ju, H.; Xu, Q.; Hu, S.; Zhu, J., Chiral Kagome Lattices from On-Surface Synthesized Molecules. *ChemPhysChem* **2017**, *18* (23), 3329-3333.

[165] Liu, J.; Li, J.; Xu, Z.; Zhou, X.; Xue, Q.; Wu, T.; Zhong, M.; Li, R.; Sun, R.; Shen, Z.; Tang, H.; Gao, S.; Wang, B.; Hou, S.; Wang, Y., On-surface preparation of coordinated lanthanide-transition-metal clusters. *Nat. Commun.* **2021**, *12* (1), 1619.

[166] Chen, Q.; Richardson, N. V., Enantiomeric interactions between nucleic acid bases and amino acids on solid surfaces. *Nat. Mater.* **2003**, *2* (5), 324-328.

[167] Kim, C. J.; Sánchez-Castillo, A.; Ziegler, Z.; Ogawa, Y.; Noguez, C.; Park, J., Chiral atomically thin films. *Nat. Nanotechnol.* **2016**, *11* (6), 520-524.

[168] Sunku, S. S.; Ni, G. X.; Jiang, B. Y.; Yoo, H.; Sternbach, A.; McLeod, A. S.; Stauber, T.; Xiong, L.; Taniguchi, T.; Watanabe, K.; Kim, P.; Fogler, M. M.; Basov, D. N., Photonic crystals for nano-light in moiré graphene superlattices. *Science* **2018**, *362* (6419), 1153-1156.

[169] Zalake, P.; Ghosh, S.; Narasimhan, S.; Thomas, K. G., Descriptor-Based Rational Design of Two-Dimensional Self-Assembled Nanoarchitectures Stabilized by Hydrogen Bonds. *Chem. Mater.* **2017**, *29* (17), 7170-7182.

[170] Silvestrelli, P. L., Hydrogen bonding characterization in water and small molecules. *J. Chem. Phys.* **2017**, *146* (24), 244315.

[171] Kitagawa, S.; Uemura, K., Dynamic porous properties of coordination polymers inspired by hydrogen bonds. *Chem. Soc. Rev.* **2005**, *34* (2), 109-119.

[172] Prince, R. B.; Barnes, S. A.; Moore, J. S., Foldamer-Based Molecular Recognition. *J. Am. Chem. Soc.* **2000**, *122* (12), 2758-2762.

[173] Saha, S.; Kauffmann, B.; Ferrand, Y.; Huc, I., Selective Encapsulation of Disaccharide Xylobiose by an Aromatic Foldamer Helical Capsule. *Angew. Chem. Int. Ed.* **2018**, *57* (41), 13542-13546.

[174] Seo, S. B.; Lee, S.; Jeon, H.-G.; Jeong, K.-S., Dramatic Enhancement of Binding Affinities Between Foldamer-Based Receptors and Anions by Intra-Receptor π-Stacking. *Angew. Chem. Int. Ed.* **2020**, *59* (26), 10441-10445.

[175] Parks, F. C.; Liu, Y.; Debnath, S.; Stutsman, S. R.; Raghavachari, K.; Flood, A. H., Allosteric Control of Photofoldamers for Selecting between Anion Regulation and Double-to-Single Helix Switching. *J. Am. Chem. Soc.* **2018**, *140* (50), 17711-17723.

[176] Wang, Y.; Xiang, J.; Jiang, H., Halide-Guided Oligo(aryl-triazole-amide)s Foldamers: Receptors for Multiple Halide Ions. *Chem. Eur. J.* **2011**, *17* (2), 613-619.

[177] Inouye, M.; Waki, M.; Abe, H., Saccharide-Dependent Induction of Chiral Helicity in Achiral Synthetic Hydrogen-Bonding Oligomers. *J. Am. Chem. Soc.* **2004**, *126* (7), 2022-2027.

[178] Roy, A.; Shen, J.; Joshi, H.; Song, W.; Tu, Y. M.; Chowdhury, R.; Ye, R.; Li, N.; Ren, C.; Kumar, M.; Aksimentiev, A.; Zeng, H., Foldamer-based ultrapermeable and highly selective artificial water channels that exclude protons. *Nat. Nanotechnol.* **2021**, *16* (8), 911-917.

[179] Qi, S.; Zhang, C.; Yu, H.; Zhang, J.; Yan, T.; Lin, Z.; Yang, B.; Dong, Z., Foldamer-Based Potassium Channels with High Ion Selectivity and Transport Activity. *J. Am. Chem. Soc.* **2021**, *143* (9), 3284-3288.

[180] Shen, Y.; Fei, F.; Zhong, Y.; Fan, C.; Sun, J.; Hu, J.; Gong, B.; Czajkowsky, D. M.; Shao, Z., Controlling Water Flow through a Synthetic Nanopore with Permeable Cations. *ACS Cent. Sci.* **2021**, *7* (12), 2092-2098.

[181] Gauthier, M.; Koehler, V.; Clavel, C.; Kauffmann, B.; Huc, I.; Ferrand, Y.; Coutrot, F., Interplay between a Foldamer Helix and a Macrocycle in a Foldarotaxane Architecture. *Angew. Chem. Int. Ed.* **2021**, *60* (15), 8380-8384.

[182] Wang, X.; Gan, Q.; Wicher, B.; Ferrand, Y.; Huc, I., Directional Threading and Sliding of a Dissymmetrical Foldamer Helix on Dissymmetrical Axles. *Angew. Chem. Int. Ed.* **2019**, *58* (13), 4205-4209.

[183] Koehler, V.; Roy, A.; Huc, I.; Ferrand, Y., Foldaxanes: Rotaxane-like Architectures from Foldamers. *Acc. Chem. Res.* **2022**, *55* (7), 1074-1085.

[184] Méndez-Ardoy, A.; Markandeya, N.; Li, X.; Tsai, Y.-T.; Pecastaings, G.; Buffeteau, T.; Maurizot, V.; Muccioli, L.; Castet, F.; Huc, I.; Bassani, D. M., Multi-dimensional charge transport in supramolecular helical foldamer assemblies. *Chem. Sci.* **2017**, *8* (10), 7251-7257.

[185] Mateus, P.; Jacquet, A.; Méndez-Ardoy, A.; Boulloy, A.; Kauffmann, B.; Pecastaings, G.; Buffeteau, T.; Ferrand, Y.; Bassani, D. M.; Huc, I., Sensing a binding event through charge transport variations using an aromatic oligoamide capsule. *Chem. Sci.* **2021**, *12* (10), 3743-3750.

[186] Jiang, H.; Léger, J.-M.; Huc, I., Aromatic δ-Peptides. *J. Am. Chem. Soc.* **2003**, *125* (12), 3448-3449.

[187] Kumaki, J.; Sakurai, S.-i.; Yashima, E., Visualization of synthetic helical polymers by high-resolution atomic force microscopy. *Chem. Soc. Rev.* **2009**, *38* (3), 737-746.

[188] Zhu, J.; Dong, Z.; Lei, S.; Cao, L.; Yang, B.; Li, W.; Zhang, Y.; Liu, J.; Shen, J., Design of Aromatic Helical Polymers for STM Visualization: Imaging of Single and Double Helices with a Pattern of π–π Stacking. *Angew. Chem. Int. Ed.* **2015**, *54* (10), 3097-3101.

[189] Verbeck, G.; Hoffmann, W.; Walton, B., Soft-landing preparative mass spectrometry. *Analyst* **2012**, *137* (19), 4393-4407.

[190] Anggara, K.; Zhu, Y.; Delbianco, M.; Rauschenbach, S.; Abb, S.; Seeberger, P. H.; Kern, K., Exploring the Molecular Conformation Space by Soft Molecule–Surface Collision. *J. Am. Chem. Soc.* **2020**, *142* (51), 21420-21427.

[191] Laskin, J.; Johnson, G. E.; Warneke, J.; Prabhakaran, V., From Isolated Ions to Multilayer Functional Materials Using Ion Soft Landing. *Angew. Chem. Int. Ed.* **2018**, *57* (50), 16270-16284.

[192] Röckert, M.; Franke, M.; Tariq, Q.; Lungerich, D.; Jux, N.; Stark, M.; Kaftan, A.; Ditze, S.; Marbach, H.; Laurin, M.; Libuda, J.; Steinrück, H.-P.; Lytken, O., Insights in Reaction Mechanistics: Isotopic Exchange during the Metalation of Deuterated Tetraphenyl-21,23D-porphyrin on Cu(111). *J. Phys. Chem. C* **2014**, *118* (46), 26729-26736.

[193] Massicot, S.; Sasaki, T.; Lexow, M.; Shin, S.; Maier, F.; Kuwabata, S.; Steinrück, H.-P., Adsorption, Wetting, Growth, and Thermal Stability of the Protic Ionic Liquid Diethylmethylammonium Trifluoromethanesulfonate on Ag(111) and Au(111). *Langmuir* **2021**, *37* (39), 11552-11560.

[194] Lee, G.; Sprunger, P. T.; Okada, M.; Poker, D. B.; Zehner, D. M.; Plummer, E. W., Chemisorption of hydrogen on the Ag(111) surface. *J. Vac. Sci. Technol. A* **1994**, *12* (4), 2119-2123.

[195] Sakurai, S.-i.; Okoshi, K.; Kumaki, J.; Yashima, E., Two-Dimensional Hierarchical Self-Assembly of One-Handed Helical Polymers on Graphite. *Angew. Chem. Int. Ed.* **2006**, *45* (8), 1245-1248.

[196] Kim, S.; Castillo, H. D.; Lee, M.; Mortensen, R. D.; Tait, S. L.; Lee, D., From Foldable Open Chains to Shape-Persistent Macrocycles: Synthesis, Impact on 2D Ordering, and Stimulated Self-Assembly. *J. Am. Chem. Soc.* **2018**, *140* (13), 4726-4735.

[197] Abramyan, A. M.; Liu, Z.; Pophristic, V., Helix handedness inversion in arylamide foldamers: elucidation and free energy profile of a hopping mechanism. *Chem. Commun.* **2016**, *52* (4), 669-672.

[198] Dolain, C.; Maurizot, V.; Huc, I., Protonation-Induced Transition between Two Distinct Helical Conformations of a Synthetic Oligomer via a Linear Intermediate. *Angew. Chem. Int. Ed.* **2003**, *42* (24), 2738-2740.

[199] Schiffrin, A.; Reichert, J.; Pennec, Y.; Auwärter, W.; Weber-Bargioni, A.; Marschall, M.; Dell'Angela, M.; Cvetko, D.; Bavdek, G.; Cossaro, A.; Morgante, A.; Barth, J. V., Self-Assembly of l-Methionine on Cu(111): Steering Chiral Organization by Substrate Reactivity and Thermal Activation. *J. Phys. Chem. C* **2009**, *113* (28), 12101-12108.

[200] Belda Maximino, R., Surface tension and density of binary mixtures of monoalcohols, water and acetonitrile: equation of correlation of the surface tension. *Phys. Chem. Liq.* **2009**, *47* (5), 475-486.

[201] Gueneli, N.; McKenna, A. M.; Ohkouchi, N.; Boreham, C. J.; Beghin, J.; Javaux, E. J.; Brocks, J. J., 1.1-billion-year-old porphyrins establish a marine ecosystem dominated by bacterial primary producers. *Proc. Natl. Acad. Sci. U.S.A.* **2018**, *115* (30), E6978-E6986.

[202] Tahoun, M.; Gee, C. T.; McCoy, V. E.; Sander, P. M.; Müller, C. E., Chemistry of porphyrins in fossil plants and animals. *RSC Adv.* **2021**, *11* (13), 7552-7563.

[203] Hans Fischer – Nobel Lecture. NobelPrize.org. Nobel Prize Outreach AB 2024. https://www.nobelprize.org/prizes/chemistry/1930/fischer/lecture/ Mon. 12 Feb 2024.

[204] The Nobel Prize in Chemistry 1915. NobelPrize.org. Nobel Prize Outreach AB 2023. https://www.nobelprize.org/prizes/chemistry/1915/summary/ Wed. 12 Jul 2023.

[205] The Nobel Prize in Chemistry 1930. NobelPrize.org. Nobel Prize Outreach AB 2023. https://www.nobelprize.org/prizes/chemistry/1930/summary/ Wed. 12 Jul 2023.

[206] Baklanov, A.; Garnica, M.; Robert, A.; Bocquet, M. L.; Seufert, K.; Küchle, J. T.; Ryan, P. T. P.; Haag, F.; Kakavandi, R.; Allegretti, F.; Auwärter, W., On-Surface Synthesis of Nonmetal Porphyrins. *J. Am. Chem. Soc.* **2020**, *142*, 1871.

[207] Rheinfrank, E.; Pörtner, M.; Nuñez Beyerle, M. d. C.; Haag, F.; Deimel, P. S.; Allegretti, F.; Seufert, K.; Barth, J. V.; Bocquet, M.-L.; Feulner, P.; Auwärter, W., Actinide Coordination Chemistry on Surfaces: Synthesis, Manipulation, and Properties of Thorium Bis(porphyrinato) Complexes. *J. Am. Chem. Soc.* **2021**, *143* (36), 14581-14591.

[208] Bernien, M.; Miguel, J.; Weis, C.; Ali, M. E.; Kurde, J.; Krumme, B.; Panchmatia, P. M.; Sanyal, B.; Piantek, M.; Srivastava, P.; Baberschke, K.; Oppeneer, P. M.; Eriksson, O.; Kuch, W.; Wende, H., Tailoring the Nature of Magnetic Coupling of Fe-Porphyrin Molecules to Ferromagnetic Substrates. *Phys. Rev. Lett.* **2009**, *102* (4), 047202.

[209] Chylarecka, D.; Wäckerlin, C.; Kim, T. K.; Müller, K.; Nolting, F.; Kleibert, A.; Ballav, N.; Jung, T. A., Self-Assembly and Superexchange Coupling of Magnetic Molecules on Oxygen-Reconstructed Ferromagnetic Thin Film. *J. Phys. Chem. Lett.* **2010**, *1* (9), 1408-1413.

[210] Wäckerlin, C.; Tarafder, K.; Girovsky, J.; Nowakowski, J.; Hählen, T.; Shchyrba, A.; Siewert, D.; Kleibert, A.; Nolting, F.; Oppeneer, P. M.; Jung, T. A.; Ballav, N., Ammonia Coordination Introducing a Magnetic Moment in an On-Surface Low-Spin Porphyrin. *Angew. Chem. Int. Ed.* **2013**, *52* (17), 4568-4571.

[211] Köbke, A.; Gutzeit, F.; Röhricht, F.; Schlimm, A.; Grunwald, J.; Tuczek, F.; Studniarek, M.; Longo, D.; Choueikani, F.; Otero, E.; Ohresser, P.; Rohlf, S.; Johannsen, S.; Diekmann, F.; Rossnagel, K.; Weismann, A.; Jasper-Toennies, T.; Näther, C.; Herges, R.; Berndt, R.; Gruber, M., Reversible coordination-induced spin-state switching in complexes on metal surfaces. *Nat. Nanotechnol.* **2020**, *15* (1), 18-21.

[212] Seufert, K.; Bocquet, M. L.; Auwärter, W.; Weber-Bargioni, A.; Reichert, J.; Lorente, N.; Barth, J. V., Cis-Dicarbonyl Binding at Cobalt and Iron Porphyrins with Saddle-Shape Conformation. *Nat. Chem.* **2011**, *3*, 114.

[213] Carlotto, S.; Cojocariu, I.; Feyer, V.; Floreano, L.; Casarin, M., The Magnetic Behaviour of CoTPP Supported on Coinage Metal Surfaces in the Presence of Small Molecules: A Molecular Cluster Study of the Surface *trans*-Effect. *Nanomater.* **2022**, *12* (2), 218.

[214] Cojocariu, I.; Carlotto, S.; Baranowski, D.; Jugovac, M.; Schio, L.; Floreano, L.; Casarin, M.; Feyer, V.; Schneider, C. M., Substitutional flexibility and molecular pinning in porphyrin-based interfaces sensitive to NO_2. *Inorg. Chim. Acta* **2023**, *556*, 121657.

[215] Castellarin-Cudia, C.; Borghetti, P.; Di Santo, G.; Fanetti, M.; Larciprete, R.; Cepek, C.; Vilmercati, P.; Sangaletti, L.; Verdini, A.; Cossaro, A.; Floreano, L.; Morgante, A.; Goldoni, A., Substrate Influence for the Zn-tetraphenyl-porphyrin Adsorption Geometry and the Interface-Induced Electron Transfer. *ChemPhysChem* **2010**, *11* (10), 2248-2255.

[216] Rojas, G.; Simpson, S.; Chen, X.; Kunkel, D. A.; Nitz, J.; Xiao, J.; Dowben, P. A.; Zurek, E.; Enders, A., Surface state engineering of molecule–molecule interactions. *Phys. Chem. Chem. Phys.* **2012**, *14* (14), 4971-4976.

[217] Lepper, M.; Köbl, J.; Schmitt, T.; Gurrath, M.; de Siervo, A.; Schneider, M. A.; Steinrück, H.-P.; Meyer, B.; Marbach, H.; Hieringer, W., "Inverted" porphyrins: a distorted adsorption geometry of free-base porphyrins on Cu (111). *Chem. Commun.* **2017**, *53* (58), 8207-8210.

[218] Bai, Y.; Sekita, M.; Schmid, M.; Bischof, T.; Steinrück, H.-P.; Gottfried, J. M., Interfacial coordination interactions studied on cobalt octaethylporphyrin and cobalt tetraphenylporphyrin monolayers on Au(111). *Phys. Chem. Chem. Phys.* **2010**, *12* (17), 4336-4344.

[219] Di Santo, G.; Blankenburg, S.; Castellarin-Cudia, C.; Fanetti, M.; Borghetti, P.; Sangaletti, L.; Floreano, L.; Verdini, A.; Magnano, E.; Bondino, F.; Pignedoli, C. A.; Nguyen, M. T.; Gaspari, R.; Passerone, D.; Goldoni, A., Supramolecular Engineering through Temperature-Induced Chemical Modification of 2H-Tetraphenylporphyrin on Ag(111): Flat Phenyl Conformation and Possible Dehydrogenation Reactions. *Chem. Eur. J.* **2011**, *17*, 14354.

[220] Röckert, M.; Franke, M.; Tariq, Q.; Ditze, S.; Stark, M.; Uffinger, P.; Wechsler, D.; Singh, U.; Xiao, J.; Marbach, H.; Steinrück, H.-P.; Lytken, O., Coverage- and Temperature-Dependent Metalation and Dehydrogenation of Tetraphenylporphyrin on Cu(111). *Chem. Eur. J.* **2014**, *20* (29), 8948-8953.

[221] Arruda, L. M.; Ali, M. E.; Bernien, M.; Nickel, F.; Kopprasch, J.; Czekelius, C.; Oppeneer, P. M.; Kuch, W., Modifying the Magnetic Anisotropy of an Iron Porphyrin Molecule by an on-Surface Ring-Closure Reaction. *J. Phys. Chem. C* **2019**, *123* (23), 14547-14555.

[222] Cojocariu, I.; Feyersinger, F.; Puschnig, P.; Schio, L.; Floreano, L.; Feyer, V.; Schneider, C. M., Insight into intramolecular chemical structure modifications by on-surface reaction using photoemission tomography. *Chem. Commun.* **2021**, *57* (24), 3050-3053.

[223] Knecht, P.; Reichert, J.; Deimel, P. S.; Feulner, P.; Haag, F.; Allegretti, F.; Garnica, M.; Schwarz, M.; Auwärter, W.; Ryan, P. T. P.; Lee, T.-L.; Duncan, D. A.; Seitsonen, A. P.; Barth, J. V.; Papageorgiou, A. C., Conformational Control of Chemical Reactivity for Surface-Confined Ru-Porphyrins. *Angew. Chem. Int. Ed.* **2021**, *60* (30), 16561-16567.

[224] Arruda, L. M.; Ali, M. E.; Bernien, M.; Hatter, N.; Nickel, F.; Kipgen, L.; Hermanns, C. F.; Bißwanger, T.; Loche, P.; Heinrich, B. W.; Franke, K. J.; Oppeneer, P. M.; Kuch, W., Surface-orientation- and ligand-dependent quenching of the spin magnetic moment of Co porphyrins adsorbed on Cu substrates. *Phys. Chem. Chem. Phys.* **2020**, *22* (22), 12688-12696.

[225] Wiengarten, A.; Lloyd, J. A.; Seufert, K.; Reichert, J.; Auwarter, W.; Han, R.; Duncan, D. A.; Allegretti, F.; Fischer, S.; Oh, S. C.; Saglam, O.; Jiang, L.; Vijayaraghavan, S.; Ecija, D.; Papageorgiou, A. C.; Barth, J. V., Surface-Assisted Cyclodehydrogenation; Break the Symmetry, Enhance the Selectivity. *Chem. Eur. J.* **2015**, *21* (35), 12285-90.

[226] Scudiero, L.; Barlow, D. E.; Hipps, K. W., Scanning Tunneling Microscopy, Orbital-Mediated Tunneling Spectroscopy, and Ultraviolet Photoelectron Spectroscopy of Nickel(II) Octaethylporphyrin Deposited from Vapor. *J. Phys. Chem. B* **2002**, *106* (5), 996-1003.

[227] Yoshimoto, S.; Inukai, J.; Tada, A.; Abe, T.; Morimoto, T.; Osuka, A.; Furuta, H.; Itaya, K., Adlayer Structure of and Electrochemical O_2 Reduction on Cobalt Porphine-Modified and Cobalt Octaethylporphyrin-Modified Au(111) in $HClO_4$. *J. Phys. Chem. B* **2004**, *108* (6), 1948-1954.

[228] Bai, Y.; Buchner, F.; Kellner, I.; Schmid, M.; Vollnhals, F.; Steinrück, H.-P.; Marbach, H.; Michael Gottfried, J., Adsorption of cobalt (II) octaethylporphyrin and 2H-octaethylporphyrin on Ag(111): new insight into the surface coordinative bond. *New J. Phys.* **2009**, *11* (12), 125004.

[229] Teugels, L. G.; Avila-Bront, L. G.; Sibener, S. J., Chiral Domains Achieved by Surface Adsorption of Achiral Nickel Tetraphenyl- or Octaethylporphyrin on Smooth and Locally Kinked Au(111). *J. Phys. Chem. C* **2011**, *115* (6), 2826-2834.

[230] Schultz, J. F.; Jiang, N., Noble Metal Substrate Identity Effects on the Self-Assembly, Dynamics, and Dehydrocyclization Reaction of Octaethylporphyrin Molecules. *J. Phys. Chem. C* **2021**, *125* (43), 23680-23687.

[231] Knecht, P.; Ryan, P. T. P.; Duncan, D. A.; Jiang, L.; Reichert, J.; Deimel, P. S.; Haag, F.; Küchle, J. T.; Allegretti, F.; Lee, T.-L.; Schwarz, M.; Garnica, M.; Auwärter, W.; Seitsonen, A. P.; Barth, J. V.; Papageorgiou, A. C., Tunable Interface of Ruthenium Porphyrins and Silver. *J. Phys. Chem. C* **2021**, *125* (5), 3215-3224.

[232] Lizzit, S.; Baraldi, A.; Groso, A.; Reuter, K.; Ganduglia-Pirovano, M. V.; Stampfl, C.; Scheffler, M.; Stichler, M.; Keller, C.; Wurth, W.; Menzel, D., Surface Core-Level Shifts of Clean and Oxygen-Covered Ru(0001). *Phys. Rev. B* **2001**, *63*, 205419.

[233] Jarzembska, K.; Seal, S.; Woźniak, K.; Szadkowska, A.; Bieniek, M.; Grela, K., X-Ray Photoelectron Spectroscopy and Reactivity Studies of a Series of Ruthenium Catalysts. *ChemCatChem* **2009**, *1*, 144.

[234] Schwarz, M.; Garnica, M.; Duncan, D. A.; Pérez Paz, A.; Ducke, J.; Deimel, P. S.; Thakur, P. K.; Lee, T.-L.; Rubio, A.; Barth, J. V.; Allegretti, F.; Auwärter, W., Adsorption Conformation and Lateral Registry of Cobalt Porphine on Cu(111). *J. Phys. Chem. C* **2018**, *122* (10), 5452-5461.

[235] Lukasczyk, T.; Flechtner, K.; Merte, L. R.; Jux, N.; Maier, F.; Gottfried, J. M.; Steinrück, H. P., Interaction of Cobalt(II) Tetraarylporphyrins with a Ag(111) Surface Studied with Photoelectron Spectroscopy. *J. Phys. Chem. C* **2007**, *111* (7), 3090-3098.

[236] Wiengarten, A.; Seufert, K.; Auwärter, W.; Ecija, D.; Diller, K.; Allegretti, F.; Bischoff, F.; Fischer, S.; Duncan, D. A.; Papageorgiou, A. C.; Klappenberger, F.; Acres, R. G.; Ngo, T. H.; Barth, J. V., Surface-assisted Dehydrogenative Homocoupling of Porphine Molecules. *J. Am. Chem. Soc.* **2014**, *136* (26), 9346-9354.

[237] Duncan, D. A.; Deimel, P. S.; Wiengarten, A.; Paszkiewicz, M.; Casado Aguilar, P.; Acres, R. G.; Klappenberger, F.; Auwärter, W.; Seitsonen, A. P.; Barth, J. V.; Allegretti, F., Bottom-Up Fabrication of a Metal-Supported Oxo–Metal Porphyrin. *J. Phys. Chem. C* **2019**, *123* (51), 31011-31025.

[238] Fanetti, M.; Calzolari, A.; Vilmercati, P.; Castellarin-Cudia, C.; Borghetti, P.; Di Santo, G.; Floreano, L.; Verdini, A.; Cossaro, A.; Vobornik, I.; Annese, E.; Bondino, F.; Fabris, S.; Goldoni, A., Structure and Molecule–Substrate Interaction in a Co-octaethyl Porphyrin Monolayer on the Ag(110) Surface. *J. Phys. Chem. C* **2011**, *115* (23), 11560-11568.

[239] Cojocariu, I.; Sturmeit, H. M.; Zamborlini, G.; Cossaro, A.; Verdini, A.; Floreano, L.; D'Incecco, E.; Stredansky, M.; Vesselli, E.; Jugovac, M.; Cinchetti, M.; Feyer, V.; Schneider, C. M., Evaluation of molecular orbital symmetry via oxygen-induced charge transfer quenching at a metal-organic interface. *Appl. Surf. Sci.* **2020**, *504*, 144343.

[240] Stoodley, M. A.; Klein, B. P.; Clarke, M.; Williams, L. B. S.; Rochford, L. A.; Ferrer, P.; Grinter, D. C.; Saywell, A.; Duncan, D. A., Adsorption structure of iron phthalocyanine and titanyl phthalocyanine on Cu(111). *Inorg. Chim. Acta* **2023**, 121679.

[241] Weber-Bargioni, A.; Auwärter, W.; Klappenberger, F.; Reichert, J.; Lefrançois, S.; Strunskus, T.; Wöll, C.; Schiffrin, A.; Pennec, Y.; Barth, J. V., Visualizing the Frontier Orbitals of a Conformationally Adapted Metalloporphyrin. *ChemPhysChem* **2008**, *9* (1), 89-94.

[242] Smith, C. A.; Narouz, M. R.; Lummis, P. A.; Singh, I.; Nazemi, A.; Li, C. H.; Crudden, C. M., N-Heterocyclic Carbenes in Materials Chemistry. *Chem. Rev.* **2019**, *119* (8), 4986.

[243] Veinot, A. J.; Al-Rashed, A.; Padmos, J. D.; Singh, I.; Lee, D. S.; Narouz, M. R.; Lummis, P. A.; Baddeley, C. J.; Crudden, C. M.; Horton, J. H., N-Heterocyclic Carbenes Reduce and Functionalize Copper Oxide Surfaces in One Pot. *Chem. Eur. J.* **2020**, *26* (50), 11431.

[244] Navarro, J. J.; Das, M.; Tosoni, S.; Landwehr, F.; Bruce, J. P.; Heyde, M.; Pacchioni, G.; Glorius, F.; Roldan Cuenya, B., Covalent Adsorption of N-Heterocyclic Carbenes on a Copper Oxide Surface. *J. Am. Chem. Soc.* **2022**, *144* (36), 16267-16271.

[245] Koy, M.; Bellotti, P.; Das, M.; Glorius, F., N-Heterocyclic carbenes as tunable ligands for catalytic metal surfaces. *Nat. Catal.* **2021**, *4* (5), 352-363.

[246] Chan, K. H.; Guan, X.; Lo, V. K. Y.; Che, C. M., Elevated Catalytic Activity of Ruthenium(II)–Porphyrin-Catalyzed Carbene/Nitrene Transfer and Insertion Reactions with N-Heterocyclic Carbene Ligands. *Angew. Chem. Int. Ed.* **2014**, *53* (11), 2982.

[247] Kim, H. K.; Hyla, A. S.; Winget, P.; Li, H.; Wyss, C. M.; Jordan, A. J.; Larrain, F. A.; Sadighi, J. P.; Fuentes-Hernandez, C.; Kippelen, B.; Brédas, J.-L.; Barlow, S.; Marder, S. R., Reduction of the Work Function of Gold by N-Heterocyclic Carbenes. *Chem. Mater.* **2017**, *29* (8), 3403-3411.

[248] Diller, K.; Klappenberger, F.; Allegretti, F.; Papageorgiou, A. C.; Fischer, S.; Wiengarten, A.; Joshi, S.; Seufert, K.; Écija, D.; Auwärter, W.; Barth, J. V., Investigating the Molecule-Substrate Interaction of Prototypic Tetrapyrrole Compounds: Adsorption and Self-Metalation of Porphine on Cu(111). *J. Chem. Phys.* **2013**, *138*, 154710.

[249] Lovat, G.; Doud, E. A.; Lu, D.; Kladnik, G.; Inkpen, M. S.; Steigerwald, M. L.; Cvetko, D.; Hybertsen, M. S.; Morgante, A.; Roy, X.; Venkataraman, L., Determination of the Structure and Geometry of N-Heterocyclic Carbenes on Au(111) Using High-Resolution Spectroscopy. *Chem. Sci.* **2019**, *10* (3), 930.

[250] Schwarz, M.; Duncan, D. A.; Garnica, M.; Ducke, J.; Deimel, P. S.; Thakur, P. K.; Lee, T. L.; Allegretti, F.; Auwärter, W., Quantitative Determination of a Model Organic/Insulator/Metal Interface Structure. *Nanoscale* **2018**, *10* (46), 21971.

[251] Grossmann, L.; Ringel, E.; Rastgoo-Lahrood, A.; King, B. T.; Rosen, J.; Heckl, W. M.; Opris, D.; Björk, J.; Lackinger, M., Steering Self-Assembly of Three-Dimensional Iptycenes on Au(111) by Tuning Molecule-Surface Interactions. *Angew. Chem. Int. Ed.* **2022**, *61* (25), e202201044.

[252] Grossmann, L.; Duncan, D. A.; Jarvis, S. P.; Jones, R. G.; De, S.; Rosen, J.; Schmittel, M.; Heckl, W. M.; Björk, J.; Lackinger, M., Evolution of adsorption heights in the on-surface synthesis and decoupling of covalent organic networks on Ag(111) by normal-incidence X-ray standing wave. *Nanoscale Horiz.* **2022**, *7* (1), 51-62.

[253] Albani, G.; Schio, L.; Goto, F.; Calloni, A.; Orbelli Biroli, A.; Bossi, A.; Melone, F.; Achilli, S.; Fratesi, G.; Zucchetti, C.; Floreano, L.; Bussetti, G., Ordered assembly of non-planar vanadyl-tetraphenylporphyrins on ultra-thin iron oxide. *Phys. Chem. Chem. Phys.* **2022**, *24* (28), 17077-17087.

[254] Majumdar, I.; Goto, F.; Calloni, A.; Albani, G.; Duò, L.; Finazzi, M.; Ciccacci, F.; Bussetti, G., Porphyrin central metal ion driven self-assembling in heterogeneous ZnTPP – CoTPP films grown on Fe(001)-p(1 × 1)O. *Appl. Surf. Sci.* **2023**, *636*, 157807.

[255] Deimel, P. S.; Feulner, P.; Barth, J. V.; Allegretti, F., Spatial Decoupling of Macrocyclic Metal–Organic Complexes from a Metal Support: a 4-Fluorothiophenol Self-Assembled Monolayer as a Thermally Removable Spacer. *Phys. Chem. Chem. Phys.* **2019**, *21* (21), 10992.

[256] Stadtmüller, B.; Willenbockel, M.; Schröder, S.; Kleimann, C.; Reinisch, E. M.; Ules, T.; Soubatch, S.; Ramsey, M. G.; Tautz, F. S.; Kumpf, C., Modification of the PTCDA-Ag bond by forming a heteromolecular bilayer film. *Phys. Rev. B* **2015**, *91* (15), 155433.

[257] Hermanns, C. F.; Bernien, M.; Krüger, A.; Miguel, J.; Kuch, W., Switching the electronic properties of Co-octaethylporphyrin molecules on oxygen-covered Ni films by NO adsorption. *J. Phys. Condens. Matter* **2012**, *24* (39), 394008.

[258] Bussetti, G.; Albani, G.; Calloni, A.; Sangarashettyhalli Jagadeesh, M.; Goletti, C.; Duò, L.; Ciccacci, F., Persistence of the Co-tetra-phenyl-porphyrin HOMO-LUMO features when a single organic layer is grown onto Cu(1 1 0)-(2 × 1)O. *Appl. Surf. Sci.* **2020**, *514*, 145891.

[259] Albani, G.; Capra, M.; Lodesani, A.; Calloni, A.; Bussetti, G.; Finazzi, M.; Ciccacci, F.; Brambilla, A.; Duò, L.; Picone, A., Self-assembly of C_{60} on a ZnTPP/Fe(001)–p(1 × 1)O substrate: observation of a quasi-freestanding C_{60} monolayer. *Beilstein J. Nanotechnol.* **2022**, *13*, 857-864.

[260] Hermanns, C. F.; Tarafder, K.; Bernien, M.; Krüger, A.; Chang, Y.-M.; Oppeneer, P. M.; Kuch, W., Magnetic Coupling of Porphyrin Molecules Through Graphene. *Adv. Mater.* **2013**, *25* (25), 3473-3477.

[261] MacLeod, J. M.; Rosei, F., Molecular Self-Assembly on Graphene. *Small* **2014**, *10* (6), 1038-1049.

[262] Pörtner, M.; Wei, Y.; Riss, A.; Seufert, K.; Garnica, M.; Barth, J. V.; Seitsonen, A. P.; Diekhöner, L.; Auwärter, W., Charge State Control of F_{16}CoPc on *h*-BN/Cu(111). *Adv. Mater. Interfaces* **2020**, *7* (15), 2000080.

[263] Zimmermann, D. M.; Seufert, K.; Đorđević, L.; Hoh, T.; Joshi, S.; Marangoni, T.; Bonifazi, D.; Auwärter, W., Self-assembly and spectroscopic fingerprints of photoactive pyrenyl tectons on *h*BN/Cu(111). *Beilstein J. Nanotechnol.* **2020**, *11*, 1470-1483.

[264] Presel, F.; Kern, C. S.; Boné, T. G.; Schwarz, F.; Puschnig, P.; Ramsey, M. G.; Sterrer, M., Charge and adsorption height dependence of the self-metalation of porphyrins on ultrathin MgO(001) films. *Phys. Chem. Chem. Phys.* **2022**, *24* (46), 28540-28547.

[265] Galeotti, G.; Fritton, M.; Lischka, M.; Obermann, S.; Ma, J.; Heckl, W. M.; Feng, X.; Lackinger, M., Initial Coupling and Reaction Progression of Directly Deposited Biradical Graphene Nanoribbon Monomers on Iodine-Passivated Versus Pristine Ag(111). *Chemistry* **2022**, *4* (2), 259-269.

[266] Mundenar, J. M.; Baddorf, A. P.; Plummer, E. W.; Sneddon, L. G.; Didio, R. A.; Zehner, D. M., Oxygen chemisorption on copper (110). *Surf. Sci.* **1987**, *188* (1), 15-31.

[267] Chua, F. M.; Kuk, Y.; Silverman, P. J., Oxygen chemisorption on Cu(110): An atomic view by scanning tunneling microscopy. *Phys. Rev. Lett.* **1989**, *63* (4), 386-389.

[268] Ethylene in Linstrom, P. J.; Mallard, W. G. (eds.); *NIST Chemistry WebBook, NIST Standard Reference Database Number 69*, National Institute of Standards and Technology, Gaithersburg (MD), (30.01.2024).

[269] Diller, K.; Papageorgiou, A. C.; Klappenberger, F.; Allegretti, F.; Barth, J. V.; Auwärter, W., In Vacuo Interfacial Tetrapyrrole Metallation. *Chem. Soc. Rev.* **2016**, *45*, 1629.

[270] Papageorgiou, A. C.; Fischer, S.; Oh, S. C.; Sağlam, Ö.; Reichert, J.; Wiengarten, A.; Seufert, K.; Vijayaraghavan, S.; Écija, D.; Auwärter, W.; Allegretti, F.; Acres, R. G.; Prince, K. C.; Diller, K.; Klappenberger, F.; Barth, J. V., Self-Terminating Protocol for an Interfacial Complexation Reaction in Vacuo by Metal–Organic Chemical Vapor Deposition. *ACS Nano* **2013**, *7*, 4520.

[271] Yang, X. F.; Wang, A.; Qiao, B.; Li, J.; Liu, J.; Zhang, T., Single-atom catalysts: a new frontier in heterogeneous catalysis. *Acc Chem Res* **2013**, *46* (8), 1740-1748.

[272] Chen, F.; Jiang, X.; Zhang, L.; Lang, R.; Qiao, B., Single-atom catalysis: Bridging the homo- and heterogeneous catalysis *Chin. J. Catal.* **2018**, *39* (5), 893–898.

[273] Cui, X.; Li, W.; Ryabchuk, P.; Junge, K.; Beller, M., Bridging homogeneous and heterogeneous catalysis by heterogeneous single-metal-site catalysts. *Nat. Catal.* **2018**, *1* (6), 385-397.

[274] Liu, L.; Corma, A., Metal Catalysts for Heterogeneous Catalysis: From Single Atoms to Nanoclusters and Nanoparticles. *Chem. Rev.* **2018**, *118* (10), 4981-5079.

List of Publications

- **Rotation of Enantiospecific Self-Assembled Array of Molecular Raffle Wheels**
  Meier, D.*; Adak, A. K.*; Knecht, P.*; Reichert, J.; Mondal, S.; Suryadevara, N.; Kumar, K. S.; Eguchi, K.; Allegretti, F.; Muntwiler, M. K.; Ruben, M.; Barth, J. V.; Narasimhan, S.; Papageorgiou, A. C.
  (* equal contribution)
  Angew. Chem. Int. Ed. **2021**, *60*, 26932-26938.
- **Structural adaptations of electrosprayed aromatic oligoamide foldamers on Ag(111)**
  Meier, D.*; Schoof, B.*; Wang. J.; Li, X.; Walz, A.; Huettig, A.; Schlichting, H.; Rosu, F.; Gabelica, V.; Maurizot, V.; Reichert, J.; Papageorgiou, A. C.; Huc, I.; Barth, J V
  (* equal contribution)
  Chem. Commun. **2022**, *58*, 8938-8941.
- **N-Heterocyclic Carbenes: Molecular Porters of Surface Mounted Ru-Porphyrins**
  Knecht, P.; **Meier, D.**; Reichert, J.; Duncan, D. A.; Schwarz, M.; Küchle, J. T.; Lee, T.-L.; Deimel, P.; Feulner, P.; Allegretti, F.; Auwärter, W.; Barth, J. V.; Papageorgiou, A. C.
  Angew. Chem. Int. Ed. **2022**, *61*, e202211877.
- **On-Surface Isomerization of Indigo within 1D Coordination Polymers**
  Xu, H.; Chakraborty, R.; Adak, A. K.; Das, A.; Yang, B.; **Meier, D.**; Riss, A.; Reichert, J.; Narasimhan, S.; Barth, J. V.; Papageorgiou, A. C.
  Angew. Chem. Int. Ed. **2024**, *63*, e202319162.
- **Investigation of *Rayleigh*'s charge limit and structure-modifying factors of soft-landed plasmid DNA in UHV**
  Meier, D.; Walz, W.; Stoiber, K.; Zhao, P.; Xu, H.; Lawes, P.; Reichert, J.; Papageorgiou, A. C.; Huettig, A.; Schlichting H.; Barth J. V.
  in preparation
- **Passivation of a metal surface strengthens the binding of an N-heterocyclic carbene to a metalloporphyrin pedestal**
  Meier, D.; Knecht, P.; Allegretti, F.; Feulner, P.; Reichert, J.; Barth, J. V.; Seitsonen, A. P.; Papageorgiou, A. C.
  in preparation

- **Multiple-Technique Approach for a Comparative Study of Ruthenium Porphyrins on Ag(111)**

  Meier, D.; Knecht, P.; Eratam, F; Vezzoni Vincente, P; Xu, H; Generalov, A; Preobrajenski, A; Lee, T.-L.; Riss, A; Yang, B; Allegretti, F.; Feulner, P.; Reichert, J.; Barth, J. V.; Seitsonen, A. P.; Duncan, D. A.; Papageorgiou, A. C.

  in preparation

- **Investigation of Differences in the Ligation Behavior of a Carbene and CO on Ruthenium Porphyrins**

  Meier, D.; Knecht, P.; Eratam, F; Vezzoni Vincente, P; Xu, H; Generalov, A; Preobrajenski, A; Lee, T.-L.; Riss, A; Yang, B; Allegretti, F.; Feulner, P.; Reichert, J.; Barth, J. V.; Seitsonen, A. P.; Duncan, D. A.; Papageorgiou, A. C.

  in preparation

- **Tuning the selectivity of C-H bond activation: 6,6′ (or 5,5′) vs. 7,7′**

  Xu, H.; Adak, A. K.; Yang, B.; **Meier, D.**; Riss, A.; Reichert, J.; Narasimhan, S.; Barth, J. V.; Papageorgiou A. C.

  in preparation

Appendix A

Experimental Details for Chapter 4

A.1 Consecutive STM images of guest bpp-COOH in a self-assembled kagome host network

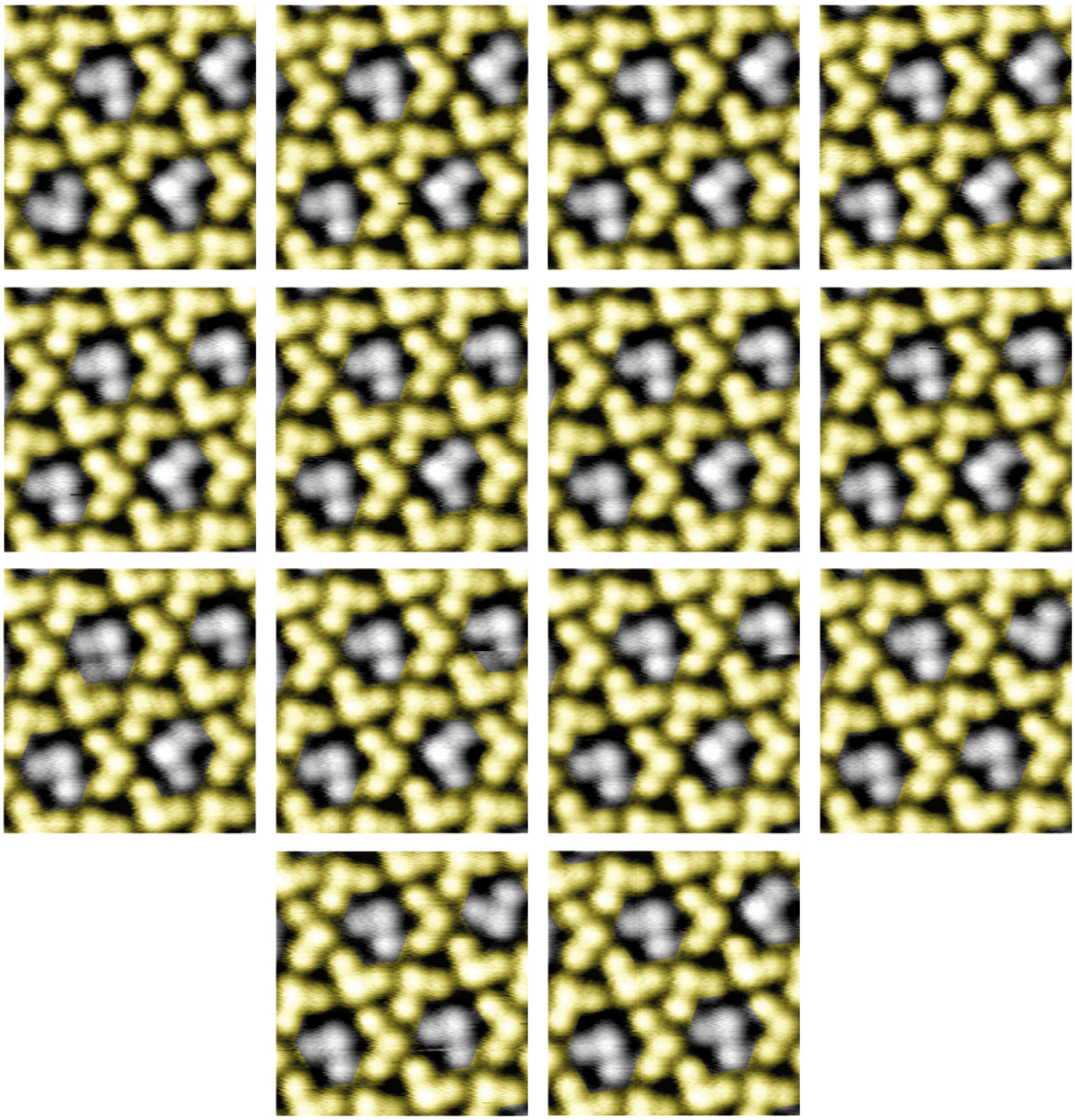

Figure A.1: Consecutive STM images (42×42 Å^2, -620 mV, 20 pA) showing the motion of bpp-COOH guest molecules in the kagome network at RT. Guest molecules are in grey and the kagome structure is highlighted in yellow. The time in between the images is approximately 15 s. Adapted from [104].

A.2 DFT optimization of *syn,syn*-host-guest Network

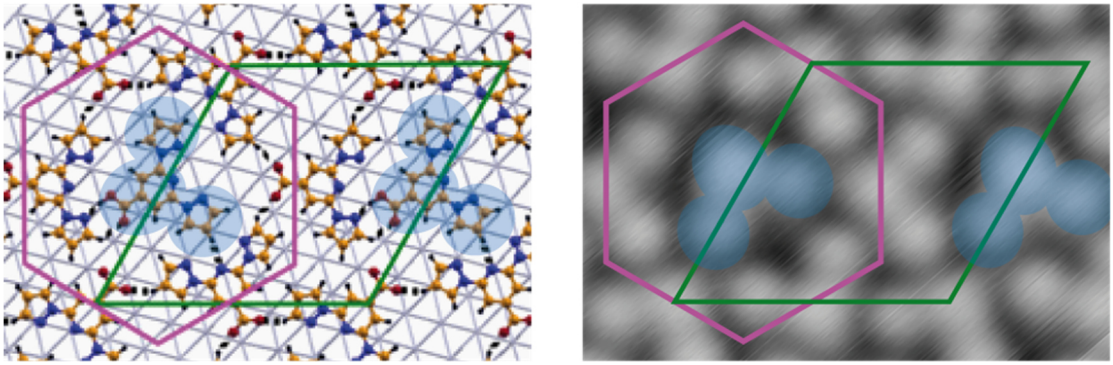

Figure A.2: The *syn,syn*-host-guest network on Ag(111). Relaxed structure from DFT (left), compared to STM data (right: -500 mV, 50 pA, 5 K). The green and magenta lines indicate the boundaries of a rhombus-shaped and hexagonal unit cell, respectively. The guest molecules are highlighted in blue. Black dotted lines indicate hydrogen bonds. C, N, O and H are in yellow, blue, red and black, respectively. Grey lines indicate Ag-Ag nearest neighbor bonds in the topmost Ag layer. Adapted from [104].

A.3 DFT optimization of a deprotonated guest molecule in a kagome host network

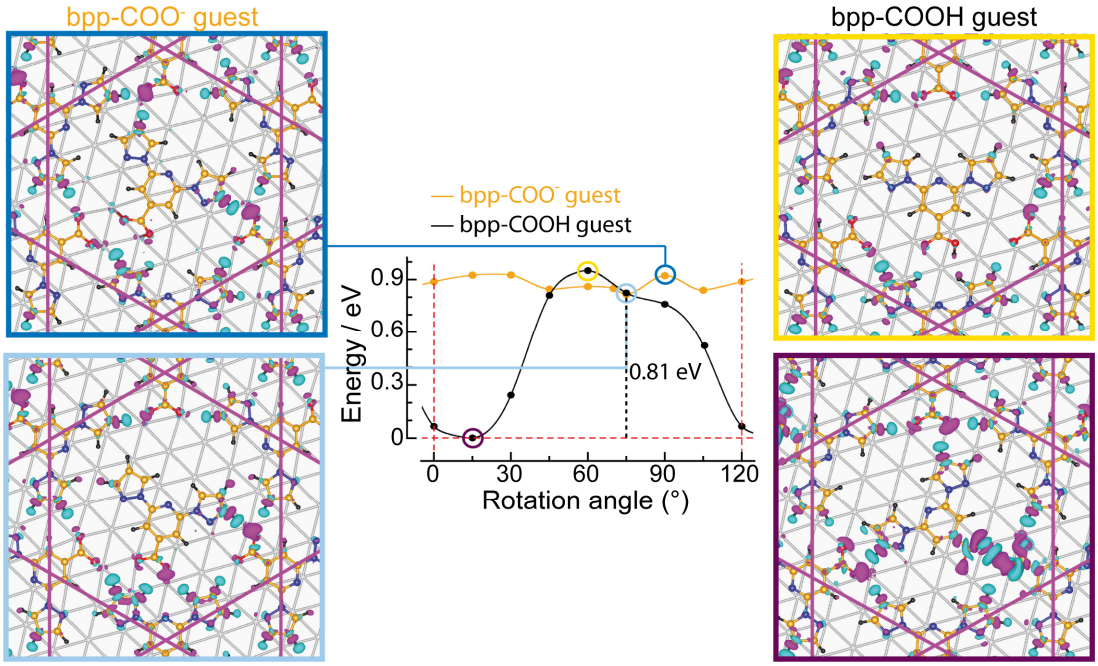

Figure A.3: Gibbs free energy comparison of rotational barrier of guest molecules for deprotonated (yellow) and protonated (black) guest. For protonated (black) guest molecules, the Gibbs free energy $G = E_{tot}$, where E_{tot} is the total energy computed from DFT. For deprotonated (yellow) guest molecules, $G = E_{tot} + 1/2\ \mu_H$ where μ_H is the chemical potential of hydrogen. Throughout the rotation, the protonated guest system is energetically favored, except in the window between 50° − 75°. The atomistic models show the DFT optimized geometries at the indicated guest orientations. C, N, O and H are in yellow, blue, red and black, respectively. Grey lines indicate Ag-Ag nearest neighbor bonds in the topmost Ag layer. Each line of alternating magenta and cyan lobes indicates the formation of a hydrogen bond. The purple lines indicate the kagome lattice of the host molecules. Adapted from [104].

Appendix B

Experimental Details for Chapter 5

B.1 Coverage dependent STM images of pyr-Q_4

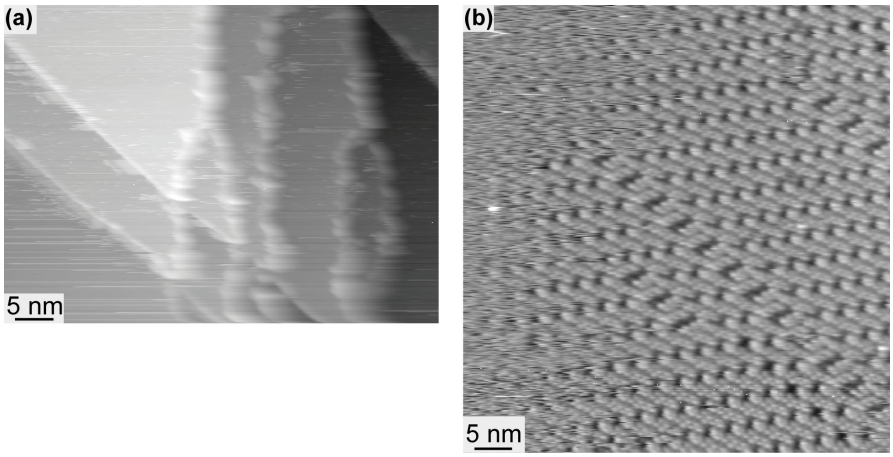

Figure B.1: (a) STM image of a $[pyr\text{-}Q_4+H]^+$ deposition with total charge 43 nC (2500 mV, 50 pA, 180 K). Molecules are only observed on the step edges. (b) STM image of a $[pyr\text{-}Q_4+H]^+$ deposition with a total charge of 325 nC (1500 mV, 50 pA, 170 K). A self-assembled island extending to more than 60 nm is depicted. Diffusing adsorbates encroach upon the borders of the island on the planar surface. Adapted from [109].

B.2 Geometry optimizations of unfolded pyr-Q_4 and pyr-Q_7 on Ag(111)

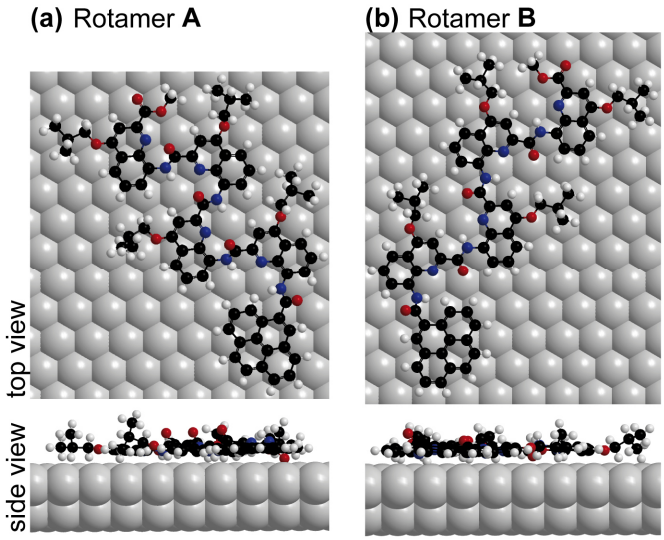

Figure B.2: Geometry optimizations (MM+) of pyr-Q_4 on Ag(111). (a) Rotamer **A** of pyr-Q_4 was obtained by rotation of the aryl-NH bonds between the quinoline monomers. (b) Rotamer **B** of pyr-Q_4 obtained by rotation of the aryl-carbonyl bonds between the quinoline monomers. C, N, O, H and Ag atoms are in black, blue, red, white and silver, respectively. Adapted from [109].

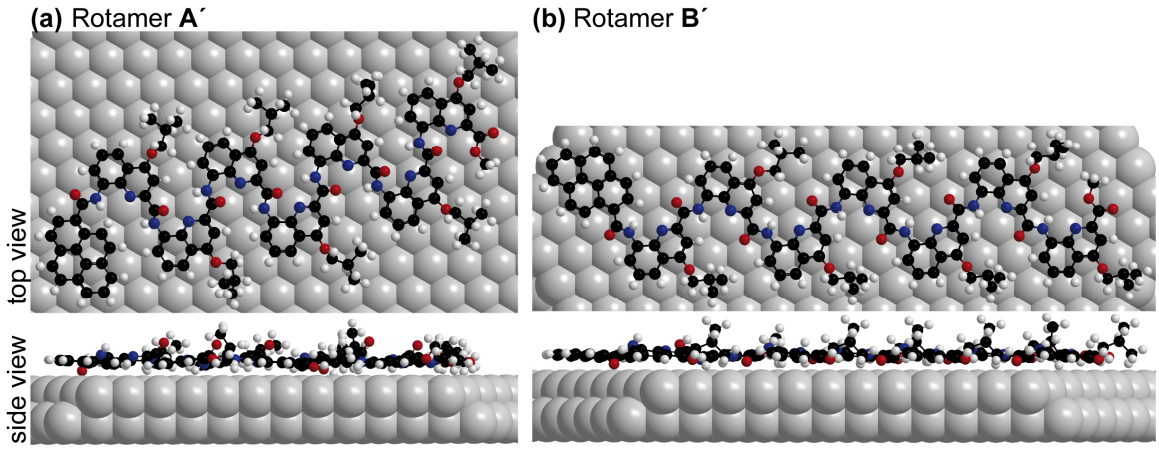

Figure B.3: Geometry optimizations (MM+) of pyr-Q_7 on Ag(111). (a) Rotamer **A'** of pyr-Q_7 was obtained by rotation of the aryl-NH bonds between the quinoline monomers. (b) Rotamer **B'** of pyr-Q_7 obtained by rotation of the aryl-carbonyl bonds between the quinoline monomers. C, N, O, H and Ag atoms are in black, blue, red, white and silver, respectively. Adapted from [109].

B.3 Comparison of experimentally and theoretically derived collision cross sections

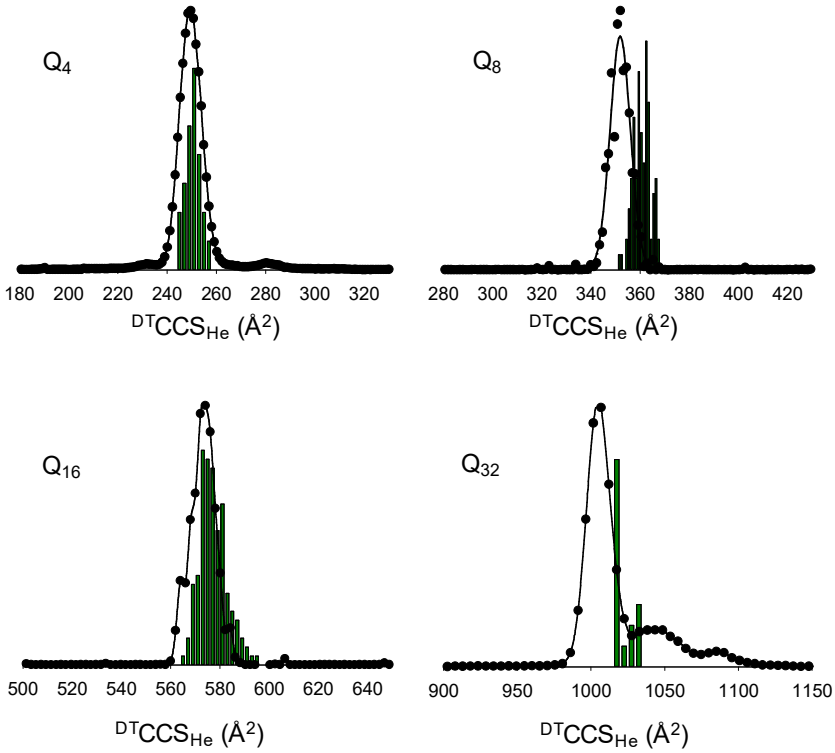

Figure B.4: $^{DT}CCS_{He}$ of the different foldamers species measured by drift tube ion mobility ESI-MS. The corresponding theoretical $^{DT}CCS_{He}$ calculated from snapshots sampled from *ab-initio* molecular dynamics simulations is displayed as histograms. For Q_4 and Q_8, DFT level (MO62X, 6-31G*) is used. Because of the size of Q_{16} and Q_{32}, semi-empirical level (PM7) is employed. Adapted from [109].

Appendix C

Experimental Details for Chapter 6

C.1 Determination of the unit cells of Ru-OEP and Ru-TBP on Ag(111)

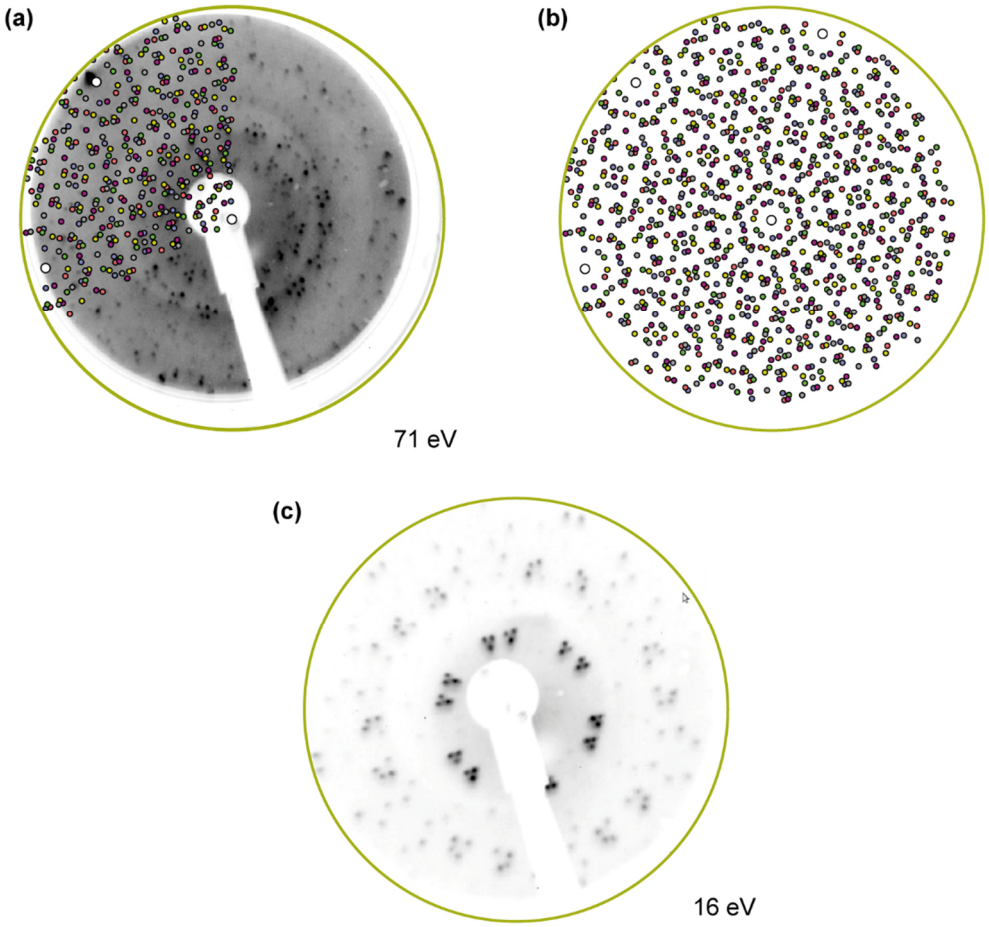

Figure C.1: LEED pattern of submonolayer phase of Ru-OEP on Ag(111) with an electron energy of (a) 71 eV and (c) 16 eV (performed in I09 end station). (b) Model of the LEED pattern. In (a) the model of the unit cell is partially overlaid over the LEED pattern.

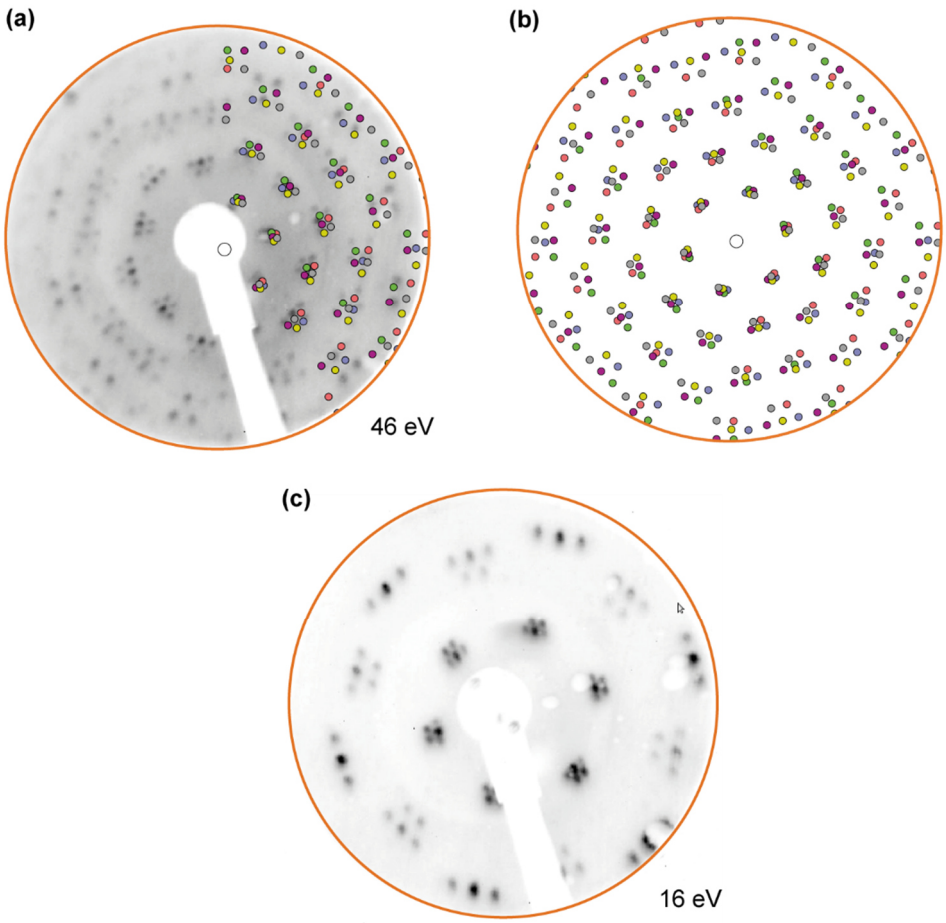

Figure C.2: LEED pattern of compressed phase of Ru-OEP on Ag(111) with an electron energy of (a) 46 eV and (c) 16 eV (performed at the I09 end station). (b) Model for the LEED pattern. In (a) the model of the unit cell is partially overlaid over the LEED pattern.

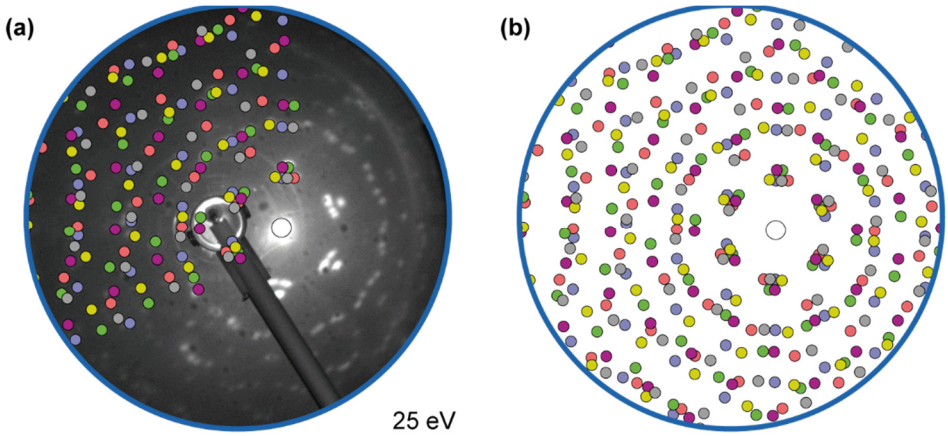

Figure C.3: (a) LEED pattern of Ru-TBP on Ag(111) with an electron energy of 25 eV partially overlaid with a model of the unit cell (performed in PSD chamber). (b) Model of the LEED pattern.

C.2 Bias dependent STM data

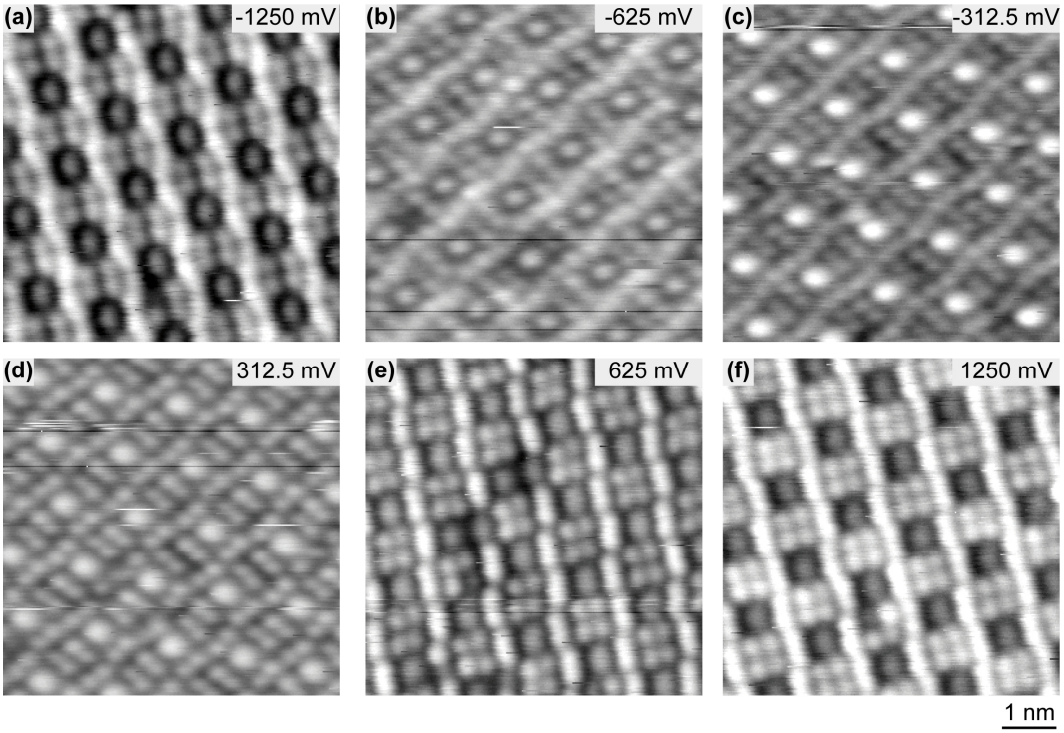

Figure C.4: Bias dependent STM images of (a-f) the compressed phase of Ru-OEP on Ag(111) (all at 20 pA) at RT. The corresponding bias is given in the respective STM images.

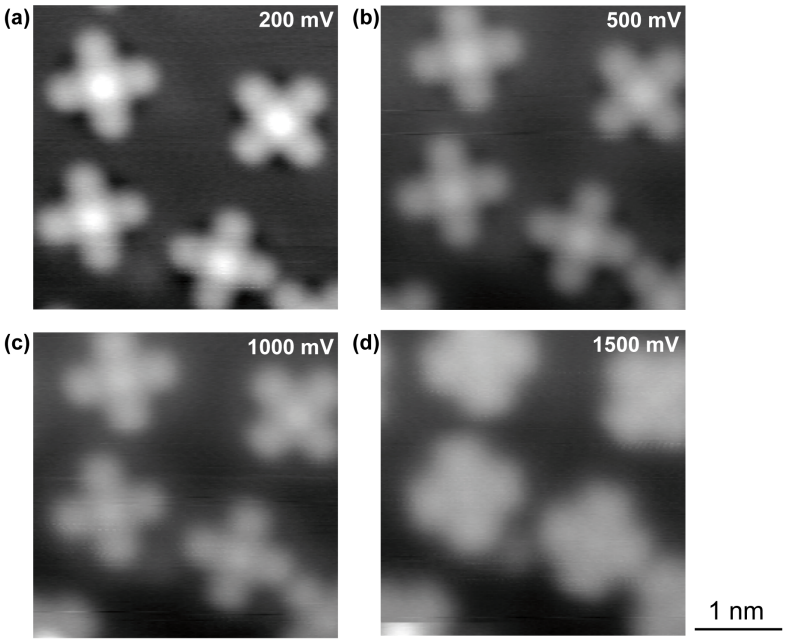

Figure C.5: Bias dependent STM images of (a-d) Ru-TBP on Ag(111) (all at 50 pA) at 5 K. The corresponding bias is given in the respective STM image.

C.3 Discrepancy between unit cell derived by LEED and STM for Ru-TBP on Ag(111)

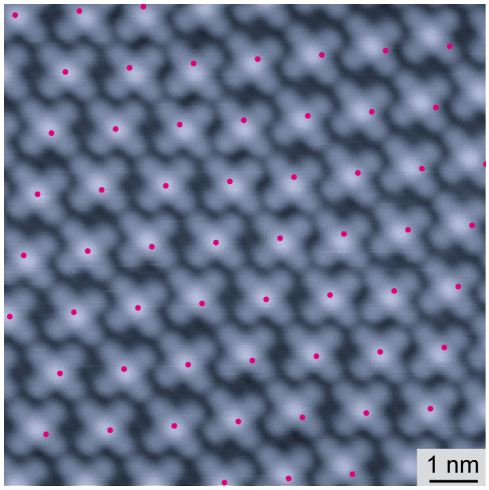

Figure C.6: STM image of Ru-TBP (50 pA, 200 mV, 5 K) on Ag(111) overlaid with the position of the porphyrins derived by the LEED unit cell (measured at 200 K) marked with pink dots. There is a discrepancy between the position of the LEED unit cell and the STM position of the porphyrins. This is ascribed to the differences in experimental temperature of both experiments.

C.4 N K-edge NEXAFS of the submonolayer phase of Ru-OEP

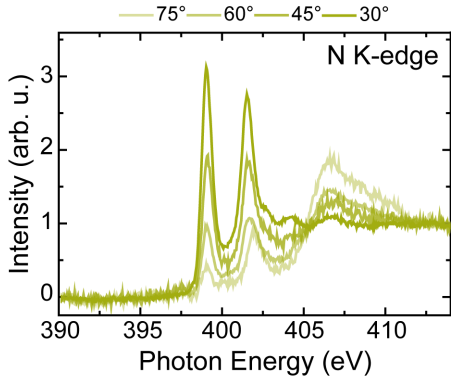

Figure C.7: Angular dependency of the N K-edge NEXAFS of the submonolayer phase of Ru-OEP on Ag(111).

Appendix D

Experimental Details for Chapter 7

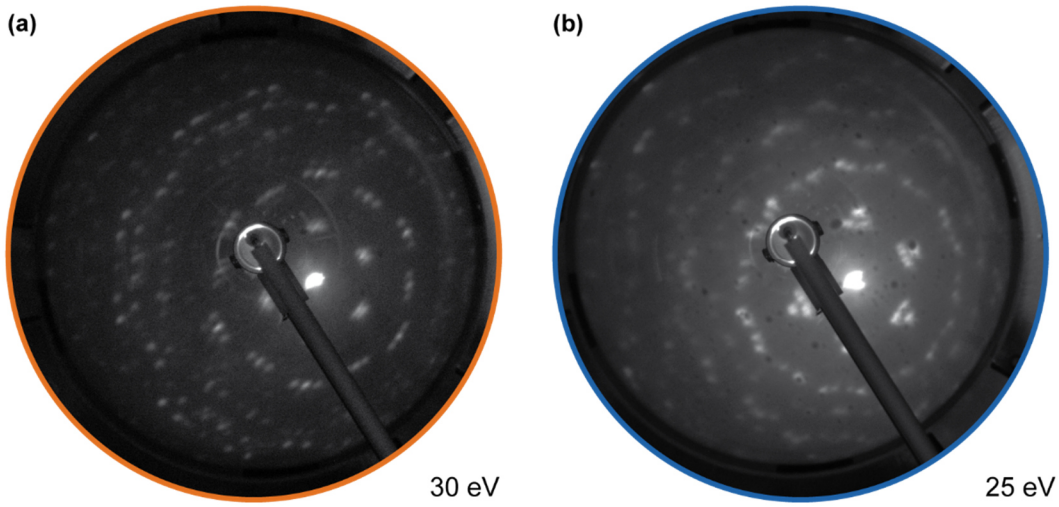

Figure D.1: LEED pattern after IMe desorption for (a) compressed phase of Ru-OEP and (b) Ru-TBP on Ag(111). The electron energy is noted next to the respective LEED pattern. No significant change after IMe desorption can be noticed.